Spring 5-31-2011

Study of the heating and ignition of metal powder by electrostatic discharge

Ervin Beloni
New Jersey Institute of Technology

ABSTRACT

STUDY OF THE HEATING AND IGNITION OF METAL POWDER BY ELECTROSTATIC DISCHARGE

by
Ervin Beloni

The objective of this work was to understand the processes that lead to ESD stimulated ignition events in metal powders. Several metals were studied: Mg, Al, and Ti. A commercially available ESD test device was adapted for the present experiments. The ESD current and voltage were measured using inductance coils; the data were used to determine the electric circuit impedance, and energy transferred to the powder. A mode of the powder ignition (individual particles vs. dust cloud), ignition delays, burn times, and velocities of ignited and ejected particles were determined from optical measurements.

It was determined that the ESD energy is delivered to the powder primarily via its Joule heating. Powder heating in ESD occurs adiabatically. Powder ejection from the sample holder is due to a reflected shockwave generated by the spark. Among many ejected particles, only some are heated to ignition. The spatial distribution of energy in the powder sample was evaluated from spark imprint measurements.

For Mg, the ESD-ejected powder produces a dust cloud flame. At the minimum ignition energy, ignition can be described by simple heat transfer analysis combined with the Mg thermal initiation kinetics. For Al powder, there is a threshold ESD energy. Above the threshold, ESD ignition results in a dust cloud flame and below the threshold, ESD ignites individual particles producing distinct luminous streaks. A correlation of the longest burn time (for the largest ignited particle) as a function of Joule energy was

observed for Al powder with nominal particle sizes in the range of 10-14 μm; however, the correlation was not detected for a finer, 3-4.5 μm powder. A simplified model proposed to describe ignition, considered the Joule energy distributed among the particles based on their surface area. For Ti, powder particles struck by ESD readily fuse together resulting in drastic reduction in the associated Joule heating and reduced ESD ignition sensitivity.

For all metals, it was found that the powder layer thickness affects significantly their ESD ignition. Both powder layer resistance and Joule energy increase with increasing layer thickness; however, the energy density increases substantially for thinner layers. Velocities of ejected particles increase for thinner layers suggesting a greater fire hazard caused by ignited particles traveling longer distances. For powders placed in a monolayer, particles struck by ESD are fragmented, resulting in enhanced ignition, a more readily formed dust cloud flame, and reduced durations of individual particle burn events due to the reduced particle dimensions.

A detailed ESD ignition model for metal powder layers was developed simulating packing of polydisperse powders using Discrete Element Modeling. In the model, the electrical resistance network created by particle contacts is analyzed to determine the powder impedance and energy distribution among heated particles. The model is calibrated for Al powders by matching predicted and measured powder resistance and Joule energy for different layer thicknesses and particle size distributions. The model predicts the temperatures of individual particles heated by ESD. It was observed that the number of particles predicted to be heated to the boiling point compares well to the number of particles ignited in respective experiments.

STUDY OF THE HEATING AND IGNITION OF METAL POWDER BY ELECTROSTATIC DISCHARGE

by
Ervin Beloni

A Dissertation
Submitted to the Faculty of
New Jersey Institute of Technology
in Partial Fulfillment of the Requirements for the Degree of
Doctor of Philosophy in Chemical Engineering

Otto H. York Department of Chemical, Biological, and Pharmaceutical Engineering

May 2011

.

APPROVAL PAGE

STUDY OF THE HEATING AND IGNITION OF METAL POWDER BY ELECTROSTATIC DISCHARGE

Ervin Beloni

Dr. Edward L. Dreizin, Dissertation Advisor — Date
Professor of Chemical Engineering, NJIT

Dr. Rajesh N. Dave, Committee Member — Date
Distinguished Professor of Chemical Engineering, NJIT

Dr. Norman Loney, Committee Member — Date
Professor of Chemical Engineering, NJIT

Dr. Robert B. Barat, Committee Member — Date
Professor of Chemical Engineering, NJIT

Dr. Richard J. Lee, Committee Member — Date
Research Physicist, Indian Head Naval Surface Warfare Center, Indian Head, MD

BIOGRAPHICAL SKETCH

Author: Ervin Beloni

Degree: Doctor of Philosophy

Date: May 2011

Undergraduate and Graduate Education:

- Doctor of Philosophy in Chemical Engineering,
  New Jersey Institute of Technology, Newark, NJ, 2011

- Master of Science in Mechanical Engineering,
  New Jersey Institute of Technology, Newark, NJ, 2008

- Bachelor of Science in Mechanical Engineering,
  New Jersey Institute of Technology, Newark, NJ, 2006

Major: Chemical Engineering

Presentations and Publications:

Williams, R.A., Beloni, E., Dreizin, E.L. Ignition of metal powder samples with different thicknesses by electrostatic discharge, Journal of Propulsion and Power, (2011) submitted for publication.

Beloni, E., Dreizin, E.L. Ignition of Ti powders by electro-static discharge, Combustion, Science, and Technology, (2011) accepted for publication.

Beloni, E., Dreizin, E.L. Ignition of metal powder by electrostatic discharge, Chapter 7, in Energetic Matierals: Thermophysical Properties, Prediction and Experimental Measurements, V. Boddu, P. Redner, Eds., CRC Press, New York, USA, (2011) 107-138.

Beloni, E., Williams, R.A., Dreizin, E.L. Effect of ESD on layer thickness on ESD ignition of spherical metal powders, 7th US National Technical Meeting of the Combustion Institute, Atlanta, GA, March 2011.

Beloni, E., Dreizin, E.L. Ignition of aluminum powders by electrostatic discharge, Combustion and Flame 157 (7), (2010) 1346-1355.

Stamatis, D., Jiang, X., Beloni, E., Dreizin, E.L. Aluminum burn rate modifiers based on reactive nanocomposite powders, Propellants, Explosives, Pyrotechnics 35 (3), (2010) 260-267.

Beloni, E., Dreizin, E.L. ESD stimulated ignition of metal powders, 32nd Annual EOS/ESD Symposium, Sparks, NV, October 2010.

Beloni, E., Dreizin, E.L. Electrostatic discharge (ESD) stimulation of metal powders, 2010 Gordon Research Conference: Energetic Materials, Tilton, NH, June 2010.

Beloni, E., Dreizin, E.L. Experimental study of ignition of magnesium powder by electrostatic discharge, Combustion and Flame 156 (7), (2009) 1386-1395.

Beloni, E., Dreizin, E.L. Ignition of aluminum powder by electrostatic discharge, 5th Annual GSA Research Day, Newark, NJ, November 2009.

Beloni, E., Dreizin, E.L. Ignition of aluminum powder by electrostatic discharge, 2009 Eastern States Section Meeting of the Combustion Institute, College Park, MD, October 2009.

Beloni, E., Dreizin, E.L. Ignition of aluminum powders by electrostatic discharge, 45th AIAA/ASME/SAE/ASEE Joint Propulsion Conference & Exhibit, Denver, CO, August 2009.

Beloni, E., Dreizin, E.L. Ignition of metal and nanocomposite powders by electrostatic discharge, 2009 NCRES Annual Meeting, La Plata, MD, April 2009.

Beloni, E., Dreizin, E.L. Combsution of decane-based slurries with metallic fuel additives, Journal of Propulsion and Power 24 (6), (2008) 1403-1411.

Beloni, E., Dreizin, E.L. Experimental study of ignition of magnesium by electro-static discharge, 2008 AIChE Annual Meeting, Philadelphia, PA, November 2008.

Beloni, E., Dreizin, E.L. Experimental study of ignition of magnesium powder by electro-static discharge, 44th AIAA/ASME/SAE/ASEE Joint Propulsion Conference & Exhibit, Hartford, CT, July 2008.

Beloni, E., Saiz-Poyatos, F., Dreizin, E.L. Electro-static discharge ignition of reactive powders, 2008 Gordon Research Conference: Energetic Materials, Tilton, NH, June 2008.

Beloni, E., Dreizin, E.L., Experimental study of ignition of Mg powder by electro-static discharge, 4th Annual Provost's Research Showcase, Newark, NJ, April 2008.

Beloni, E., Trunov, M.A., Dreizin, E.L. Ignition of metal powders by electric spark, 2007 AIChE Annual Meeting, Salt Lake City, UT, November 2007.

Beloni, E., Trunov, M.A., Dreizin, E.L. Ignition of metal powders by electric spark, AIChe Annual Meeting Conference Proceedings, 2007.

Beloni, E., Dreizin, E.L. Development of insensitive high energy density nanomaterials, AIAA Region I-NE Student Conference, Cambridge, MA, April 2007.

Beloni, E., Hoffmann, V.K., Dreizin, E.L., Combustion of decane-based slurries with metallic fuel additives, 45th AIAA Aerospace Sciences Meeting, Reno, NV, January 2007.

Beloni, E., Hoffmann, V.K., Dreizin, E.L., Combustion of decane-based slurries with metallic fuel additives, Collection of Technical Papers – 45th AIAA Aerospace Sciences Meeting 24, (2007) 16896-16907.

Beloni, E. Hoffmann, V.K., Dreizin, E.L. Combustion of decane-based slurries with metallic fuel additives, AIAA Region I Young Professional Student Education Conference, Laurel, MD, November 2006.

To my parents**, Terizia and Josef,** and to my grandmother**, Mary**

ACKNOWLEDGMENT

First, I would like to thank my advisor, Dr. Edward L. Dreizin, for his support and encouragement of my research over the years. I am indebted to his vast knowledge and insight, which helped me keep my focus and allowed me to complete my research. I would like to also thank my committee members: Dr. Rajesh Dave, Dr. Norman Loney, Dr. Robert Barat, and Dr. Richard Lee, for their participation and suggestions during my proposal and defense.

I would like to also acknowledge members of Dr. Dreizin's research group that have supported me over the years. I would like to thank Vern Hoffmann for his expertise in the design and manufacture of experimental equipment. I would like to thank Dr. Mirko Schoenitz, Dr. Robert Gill, Dr. Salil Mohan, and Dr. Alex Ermoline for their suggestions that improved my research. I would like to thank my fellow students and friends from Dr. Dreizin's research lab group who made this journey both interesting and rewarding: Demitrios Stamatis, Carlo Badiola, Priya Santhanam, Yasmine Aly, Shasank Vummidi, Shasha Zhang, Paul Dupiano, and Rayon Williams.

Lastly, I would like to thank Dr. Ralph A. Anthenien of the US Army Research Office for funding this work. Without his constant interest, none of this would be possible.

TABLE OF CONTENTS

TABLE OF CONTENTS
(Continued)

TABLE OF CONTENTS
(Continued)

TABLE OF CONTENTS
(Continued)

TABLE OF CONTENTS
(Continued)

Chapter **Page**

LIST OF TABLES

LIST OF FIGURES

LIST OF FIGURES
(Continued)

LIST OF FIGURES
(Continued)

Figure **Page**

LIST OF FIGURES
(Continued)

Figure **Page**

LIST OF FIGURES
(Continued)

LIST OF FIGURES
(Continued)

Figure **Page**

LIST OF FIGURES
(Continued)

LIST OF FIGURES
(Continued)

LIST OF FIGURES
(Continued)

LIST OF FIGURES
(Continued)

Figure **Page**

CHAPTER 1

INTRODUCTION

1.1 Background

Electro-static spark is a common ignition stimulus for both condensed and gas-phase flammable compounds, e.g. [1-4]. Multiple tests, standards, and evaluation methodologies have been and continue being developed to investigate ignition behavior of different substances struck by a spark [5-8]. Electro-static discharge (ESD) ignition of flammable gases was studied in great detail motivated by both safety requirements for handling flammable gas mixtures and convenience of using spark discharge as a controlled energy igniter for fundamental flammability studies. Effects of electrode materials, electrode shape, discharge duration, and other similar parameters have been quantified and reported. Reviews by Mellor et al., [9-10] published in 1990's described these trends and suggested that a similar systematic study would be necessary to establish a scientifically sound test of ESD sensitivity of powders. Ignition of various aerosolized powders (or flammable dust clouds) has been studied by many investigators, e.g., [11-13]. Important in their own right, such studies, however, do not provide insight for ignition mechanisms and flammability limits for powders stored in containers or spread on solid surfaces, both situations are ubiquitous in many industries. On the other hand, experimental tests of ESD ignition sensitivity for non-aerosolized powders are among the most commonly used safety assessments for powdered materials, including agricultural and food [14], textile [15], pharmaceutical [16], plastic [17-18], metallic [19-21] and of course, energetic components [22-23]. Typically, a spark is generated by a high-voltage capacitor discharging over a gap between a sharpened electrode and a powder bed. The

sharpened electrode can approach the surface or fixed at a certain distance from it. The minimum capacitor energy at which the powder ignites is specified as the minimum ignition energy (MIE), a parameter defining the sensitivity of a powder to ESD ignition stimulation [1-2]. It has been suggested [23] that the spark represents primarily a thermal source capable of raising the temperature of a flammable powder above the point at which thermal runaway occurs. However, it remains unclear how the spark heats the powder particles, what portion of the spark energy is being transferred to the powder and by which mechanism. For example, the spark's plasma can heat the powder surface directly while the current of the spark discharge can result in Joule heating distributed in the powder volume, along the current path. It remains unclear whether the polarity of the spark discharge is a factor affecting the ignition energy. The transport properties of powders including their thermal and electrical conductivities are initially governed by the respective contact resistances between the particles. While a powder is heated, gasified, and/or being melted, its transport properties are expected to change dramatically [24-25] affecting its interaction with the spark. The spark itself does not behave as a steady heat source and the energy distribution is expected to change as a function of both time and location. However, it is unclear whether the ignition governed by a runaway chemical reaction occurs within the same time frame as the relatively short-lived spark discharge, and thus whether the temporal changes in the spark energy distribution are significant in affecting the ignition sensitivity of various materials.

Understanding the mechanisms of the ESD ignition of powders becomes increasingly important with dramatic acceleration in recent research aimed to develop new powdered materials, including nanomaterials for a variety of applications. Current

protocols used for ESD ignition sensitivity testing, e.g., described in various standards, e.g., [26-27] are not based on such understanding and the results are often inconsistent between different testers and inconclusive in nature. Furthermore, the current protocols are not suitable for a number of newly developed powders, which are not available in the quantities required for the standardized testing. At the same time, often the development of new material manufacturing processes necessary to produce sufficient material quantities may hinge upon its positive safety evaluation, of which a conclusive ESD sensitivity evaluation is a necessary part.

1.2 Objectives and Approach

This work combines systematic experimental and modeling efforts and is expected to establish and quantitatively describe mechanisms of ignition of various powder-like materials by electric sparks. In the experimental portion of this effort, ESD ignition of metal powder will be addressed. In particular, magnesium, aluminum and titanium were selected for this study. There are relatively reliable descriptions for its thermal ignition available in the literature for Mg and Al [28-30]. For Ti, thermal ignition kinetics will be quantified using the method introduced in Reference [29].

As discussed earlier a systematic approach to determine which parameters affect ignition is needed and will be established. These parameters include sample preparation; particularly powder sample thickness and powder ejection will be addressed. In addition the effects of capacitance, capacitor voltage, discharge duration and gap between discharge pin and electrode, will be addressed. For each ignition experiment, the amount of energy delivered to the powder by the ESD will be determined. In addition to quantifying the energy that is delivered to the powder, its effect on ignition will be

determined from optical measurements including burn duration, ignition delay, light intensity and flame/particle velocity. From these measurements, the burn behavior of the powder can be described. The results of the measurements will be used in quantitative modeling of the ESD stimulated powder ignition. Initial modeling will look into what material and electrical parameters along with ignition kinetics describe the events that lead to ignition. In particular, how the ESD energy is distributed throughout the powder will be investigated.

A discrete element method (DEM) model will be used to describe how the powder layer resistance is generated inside the powder bed. The powder will be modeled by a commercial DEM program. The particle size distribution (PSD), layer thickness, and packing will be simulated to match the powder in experiment. An electrical resistance model will describe the contact resistance between particles. The contact resistances will be used to generate an equivalent resistance of the powder bed and compare it to the measured powder layer resistance. The effect of how the spark current enters the powder as well as how the powder heating is affected by the powder layer thickness will be addressed. In the model, the heat generated at the particle contacts will be distributed to the particles in contact, and the number and sizes of particles that have reached ignition will be compared to the experimental results.

CHAPTER 2

EXPERIMENTAL APPARATUS AND MATERIALS

2.1 Electrostatic Discharge Apparatus

A schematic diagram of the experimental setup is shown in Figure 2.1. A Model 931 Firing Test System (FTS) by Electro-Tech Systems, Inc. was used to generate spark discharges. FTS includes a capacitor bank with capacitance varied in the range of 100–10000 pF. The capacitors can be discharged through the spark gap directly or through an additional resistor varied from 500 to 5000 Ω. Additional resistors were not used in this project. The capacitors can be charged to a voltage varied from 100 V to 26 kV. The polarity of the electric output can be changed so that the high-voltage electrode can be either positive or negative. For a standard test [26], the powder is placed into a stainless steel cup (15 mm diameter, 3 mm deep) affixed to a grounded base. The high voltage pin-electrode (a stainless steel needle) is placed 0.2 mm above the surface of the powder being tested. If sufficient energy is delivered to the powder, ignition occurs. In a standard test [26], ignition is determined to have occurred when the ignited powder produces a bright white flame.

In addition to igniting powder in air, the gas environment can also be controlled. The discharge electrodes were placed in a sealable vacuum chamber, allowing the air to be replaced with a desired gas environment. A controlled gas environment was used to investigate the fragmentation of powder prepared as a monolayer and struck by a spark (see Chapters 5 and 6).

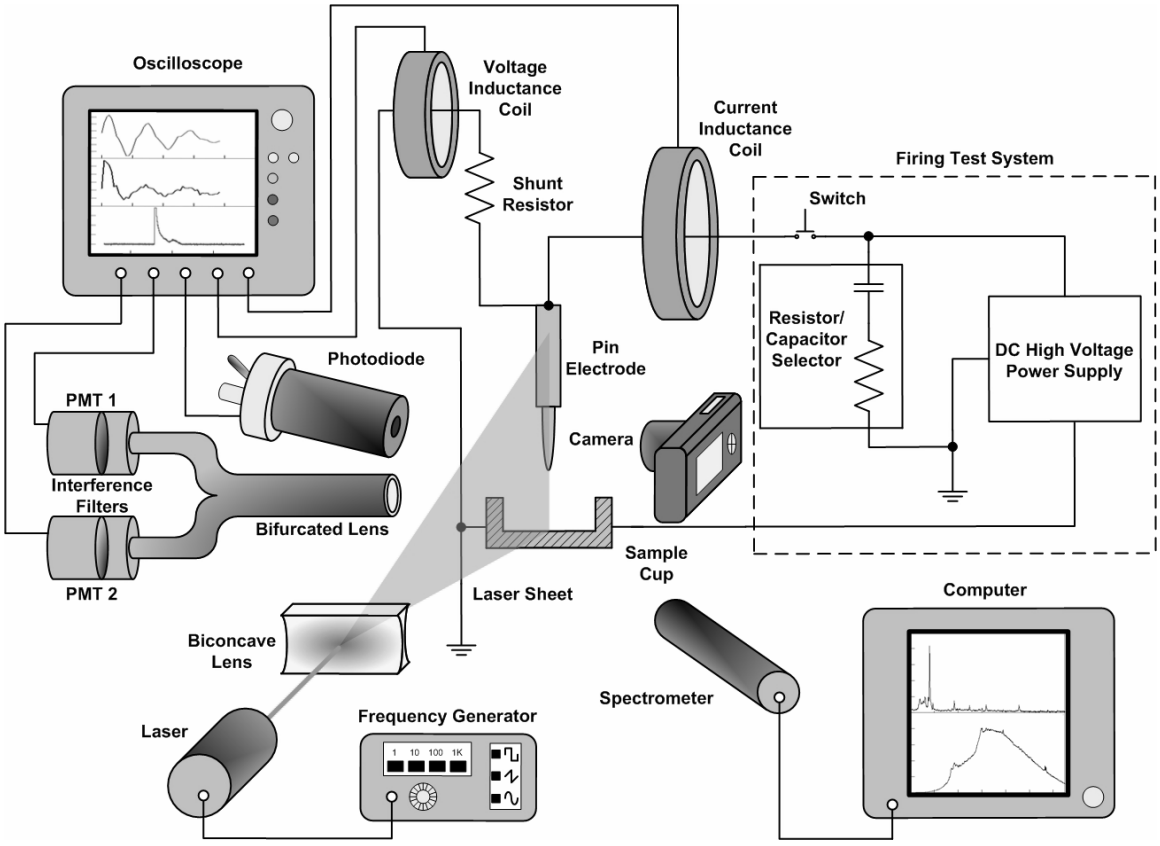

Figure 2.1 Schematic diagram of the experimental setup.

2.2 Sample Holders

Several sample holders were used in this work. A standard sample holder is a stainless steel cup described above. Two custom-made sample holders were made and used to assess the effect of the powder amount on its ignition for initial experiments with Mg. For both custom-made sample holders, it was desired to avoid the possibility for the spark to strike the sample holder surface rather than the powder directly. Therefore, the only conductive surfaces of each of the two customized sample holders were their bottom surfaces on which the powder was placed. The sample holders were comprised of aluminum plates with dielectric washers affixed by an epoxy resin. A 6 mm internal diameter, 0.5 mm-thick nylon washer was used to make a larger customized sample

holder. Similarly, a 2.1 mm internal diameter, 0.6 mm-thick polycarbonate washer was used to make a smaller sample holder. Powder was poured into the cup, which was gently tapped to fill it uniformly. Excess powder was scraped off the top to ensure an even layer thickness. The same loading method was used for all samples prepared with custom made sample holders

For experiments focused on ignition mechanisms and continued combustion of ejected Al and Ti particles, a brass cup holding a much smaller powder sample, 6 mm in diameter and 0.5 mm in depth, was used. For Ti, several layer thicknesses were prepared: 1 mm, 0.5 mm, 0.25 mm, and a powder monolayer, to investigate the effect of particle fusing (see below). To prepare layer thicknesses of 1, 0.5, and 0.25 mm, powder was filled in a sample cup with respectively selected depth. The cup was made from a 18.5 mm diameter brass cylinder surrounded by a PVC washer, which served as the cup wall. The cup depth was selected by sliding the washer above the brass cylinder so that the cup depth equaled the layer thickness. The washer fit tightly onto the cylinder to ensure that it did not move once it was placed in its proper position. In selected experiments, multiple discharges could be applied to different locations on the surface of a filled sample cup, because the effect of the spark was localized to a small, less than 1-2 mm diameter sample area leaving the rest of the powder undisturbed.

A monolayer was produced by pouring powder on a double sided carbon tape adhered to a 18-mm diameter brass support. Excess powder was blown away and the powder remaining on the tape formed a monolayer. To investigate the effect of a sample several monolayers thick, a coating of slurried powder was applied to the surface of 6 mm diameter brass stub. The slurry was made by mixing 0.2 g of powder with 3 ml of

hexane. The coating was allowed to dry for 5 minutes before ESD ignition testing. This coating technique was used for Mg and Al powders only. In all experiments, to ensure good electrical contact, silver paste from Ted Pella, Inc. was placed on the bottom of the holder affixed to the grounded base. All metal surfaces were polished with 1200 grit sandpaper prior to experimental use.

2.3 Binder

Several experiments were conducted with a small amount of binder added to Mg powder in order to investigate the effect of powder ejection by electric spark (see below) on its ignition. The binder chosen for these experiments was Star Brite liquid electrical tape which contains a vinyl acetate co-polymer, hydrocarbons, and ketones [31]. 0.1 g of binder was diluted in 10 ml of acetone. 1 ml of the diluted binder solution was added to 0.4 g of powder, thoroughly mixed, added to the sample holder, and air dried prior to testing. The binder amount was estimated to be only 0.3 wt. % of the binder/powder mixture. The binder was only used in selected tests utilizing a larger (6 mm diameter) customized sample holder described above. In addition, the same dilute binder solution was used visualize ESD spark imprints. As in coating experiments, the solution was allowed to dry for 5 minutes prior to testing.

2.4 Diagnostics

Inductance coils by Pearson Electronics were used to measure spark current and voltage across the pin electrode and sample gap. The current was measured using a model 110A coil with a 1 V / 10 A ratio. To measure the voltage drop, a 1 kΩ high voltage resistor was connected in parallel between the discharge pin and sample cup substrate. The

current through the resistor proportional to the spark voltage was measured using a model 4100 coil with a 1 V / 1 A ratio. Both current and voltage traces were visualized and recorded by a LeCroy WaveSurfer 64Xs Series oscilloscope.

Optical emission produced by the spark and by the igniting Mg powder was monitored in real time. In preliminary measurements, optical spectra produced respectively by sparks between the pin electrode and an empty sample cup and between the pin electrode and igniting Mg powder were recorded using an EPP2000 spectrometer by Stellarnet Inc. The recorded spectra are shown in Figure 2.2 without correction for sensitivity of the spectrometer.

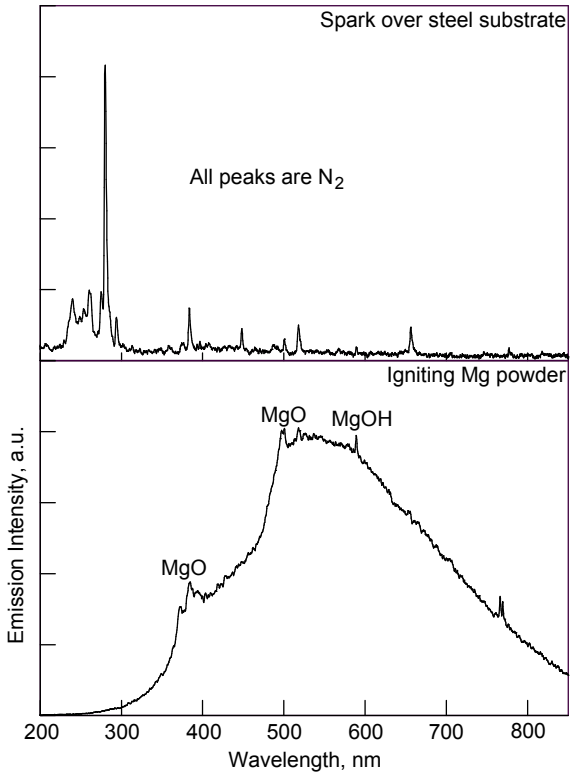

Figure 2.2 Emission spectra of the sparks between the pin electrode and an empty steel sample cup (top) and between the pin electrode and igniting Mg powder (bottom).

The lack of correction results in a distortion of the black-body emission envelope, while the uncorrected spectra are still helpful for identifying the spectral regions most suitable for monitoring the emissions produced by the spark and by the heated and ignited powder. The emission of the spark itself (generated over an empty sample cup) was dominated by an ultraviolet peak (around 280 nm) and it was assigned to molecular nitrogen [32-33]. The emission of the igniting Mg powder was heavily dominated by a broad black-body spectrum with one of the strong peaks observed around 500 nm, assigned to MgO. Respectively, interference filters at 280 nm and 500 nm were selected to separate between the radiation signatures of the spark and igniting powder. A bifurcated fiber optics cable with a single input window was used to split the optical signal between two outputs. Each output was connected to a respective interference filter and a photomultiplier.

The emission of the burning Mg, Al, and Ti particles was measured by a Thorlabs DET110 photodiode. The photodiode was placed 20 mm away from the discharge pin. Still images of the burning particles were acquired with an Optio Z10 digital camera with an open shutter placed at a distance of 20 cm from the discharge pin. A laser sheet was used for the visualization of ejected particles. The laser sheet was produced by a 20 mW Shanghai Uniwave Technology DPGL-3020 model laser with a wavelength centered at 532 nm passing through a biconcave lens. The laser irradiation was modulated at 1000 Hz by an Exact Electronics Model 119 function generator so that the particle trajectories appeared as dashed lines allowing visualization of individual ejected particles and evaluation of their velocities.

2.5 Preliminary Characterization of the Spark

In initial experiments, emission and electrical current traces were acquired for sparks striking solid metal substrates. The distance between the pin electrode and the substrate surface was maintained at 0.2 mm. The spark polarity, the value of the discharging capacitor, and the material of the substrate varied while the initial voltage was fixed at V_0=5 kV. Figure 2.3 shows typical examples of the current trace and radiation traces recorded using ultra-violet (280 nm) and green (500 nm) interference filters. Both the current and 280-nm filtered traces showed a strong AC component. A change in the pre-set polarity of the spark discharge using the FTS polarity selection did not appreciably change the shapes of the recorded current traces. The oscillations in current corresponding to the repeated re-charging of the capacitor correlated with the oscillations in the filtered spark emission signal.

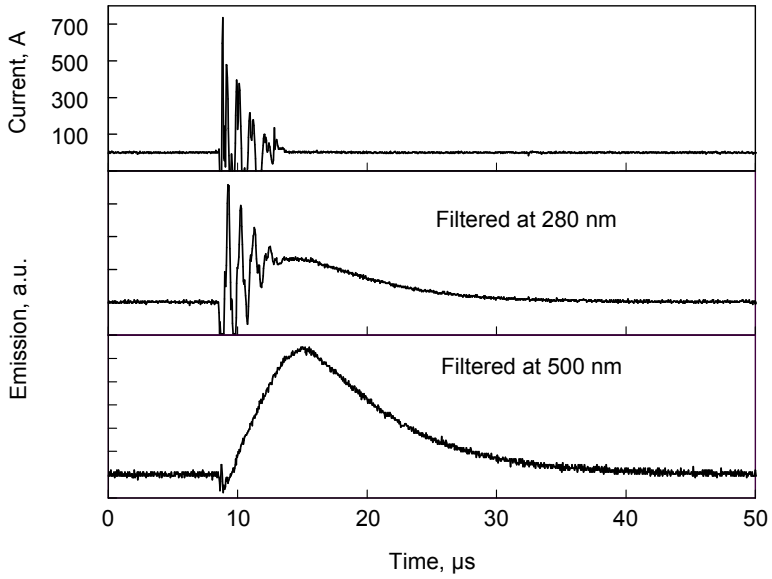

Figure 2.3 Examples of the spark current and emission traces (traces shown were obtained from a spark striking a stainless steel substrate, pin electrode was negative, V_0 = 5 kV, C = 5000 pF, and no additional resistor).

The green filtered trace showed no oscillations and the signal continuously increased during the time the spark current was measured. This clearly indicates the thermal radiation produced by the surface heated by the spark. Both radiation traces were observed to decay after the current trace was reduced to zero. Note that for both radiation signals the initial levels shift to negative voltage values with the onset of the spark current. This shift is clearly indicative of a parasitic interference between the noise generated by the spark and the acquired emission signals. However, a clear difference between the shapes of the emission traces recorded simultaneously and using the same data acquisition device suggests that the difference in the optical emission signatures produced at the wavelengths of 280 and 500 nm is real.

2.6 Magnesium Powder

The powder used in the ignition experiments was 1-11 μm spherical Mg by Hart Metals, Inc. The particle size distribution was measured using a Beckman-Coulter LS230 Enhanced Particle Analyzer and is shown in Figure 2.4. Based on the volumetric size distribution, the mean particle size is 10.3 μm. Particle shapes are shown in Figure 2.5; the particles are rather spherical and un-agglomerated. This same powder was earlier used in experiments on thermal ignition of Mg using an electrically heated filament [29] so that direct comparison is possible.

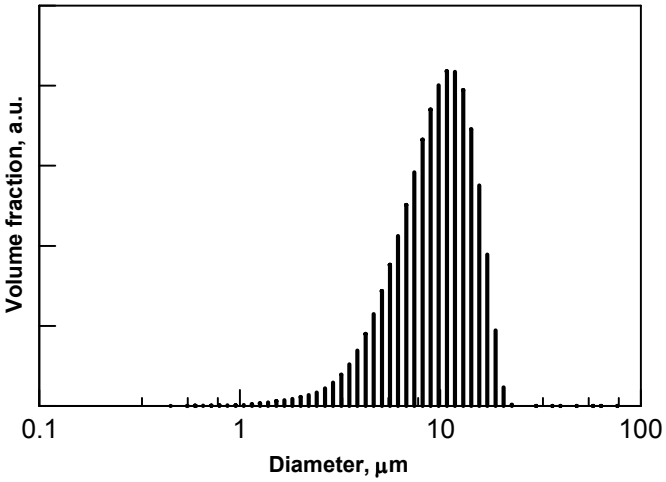

Figure 2.4 Particle size distribution of spherical Mg powder used in experiment having a mean particle size of 10.3 μm.

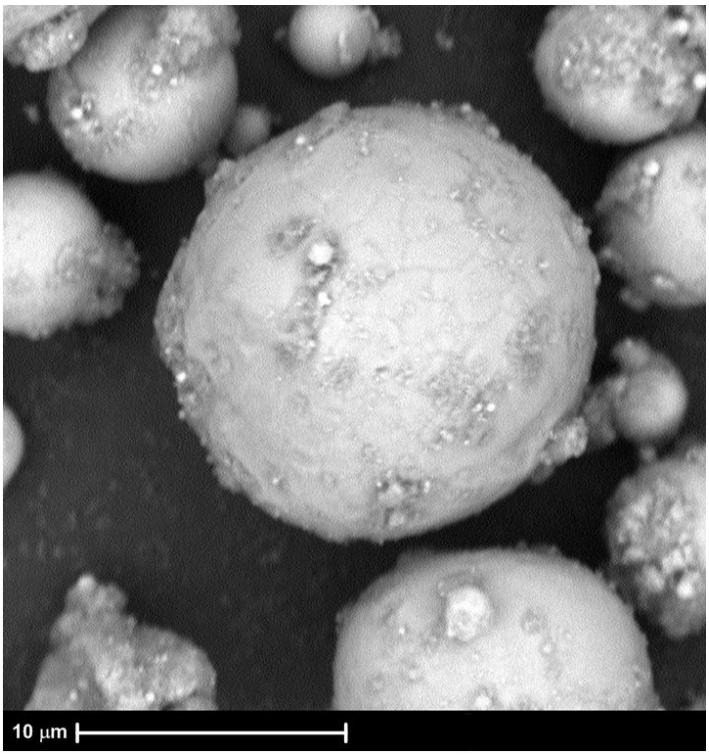

Figure 2.5 SEM image of spherical Mg used in experiment, showing un-agglomerated spherical particles.

2.7 Aluminum Powder

Two spherical powder samples with different particle size distributions were used: nominal dimensions 3-4.5 μm and 10-14 μm, both by Alfa Aesar. The particle size distributions for both powders were measured by low-angle laser light scattering using a Coulter LS 230 analyzer. The size distributions are shown in Figure 2.6. The volumetric mean diameters are 7.01 and 21.5 μm for Al 3-4.5 μm and 10-14 μm, respectively. The Al 3-4.5 μm powder size distribution includes substantial number of very fine, submicron particles, unlike the size distribution for the 10-14 μm powder.

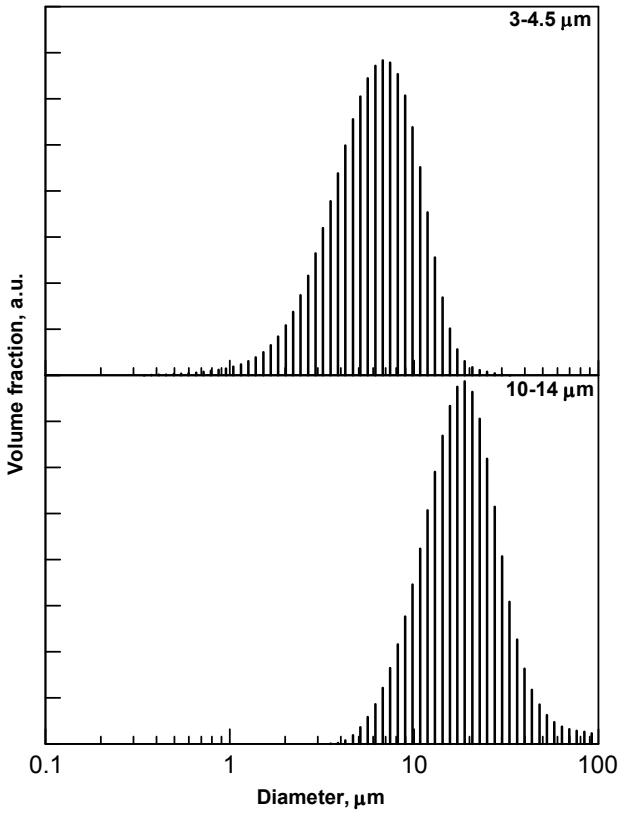

Figure 2.6 Particle size distributions of Al 3-4.5 μm and Al 10-14 μm.

SEM (scanning electron microscope) images of both powders are shown in Figure 2.7. The left image shows the 3-4.5 μm powder. All small particles are agglomerated and form relatively large clusters. Some of these clusters also include larger sized particles. In fact, no larger particles without attached small particles were detected in the acquired SEM images. Different de-agglomeration techniques including ultrasonication, drying, and tumble-milling were applied without apparent reduction in the number of agglomerates detected by the following SEM inspection. Little agglomeration is seen in the Al 10-14 μm powder (right image) in Figure 2.7. For both powders, the particles are mostly spherical.

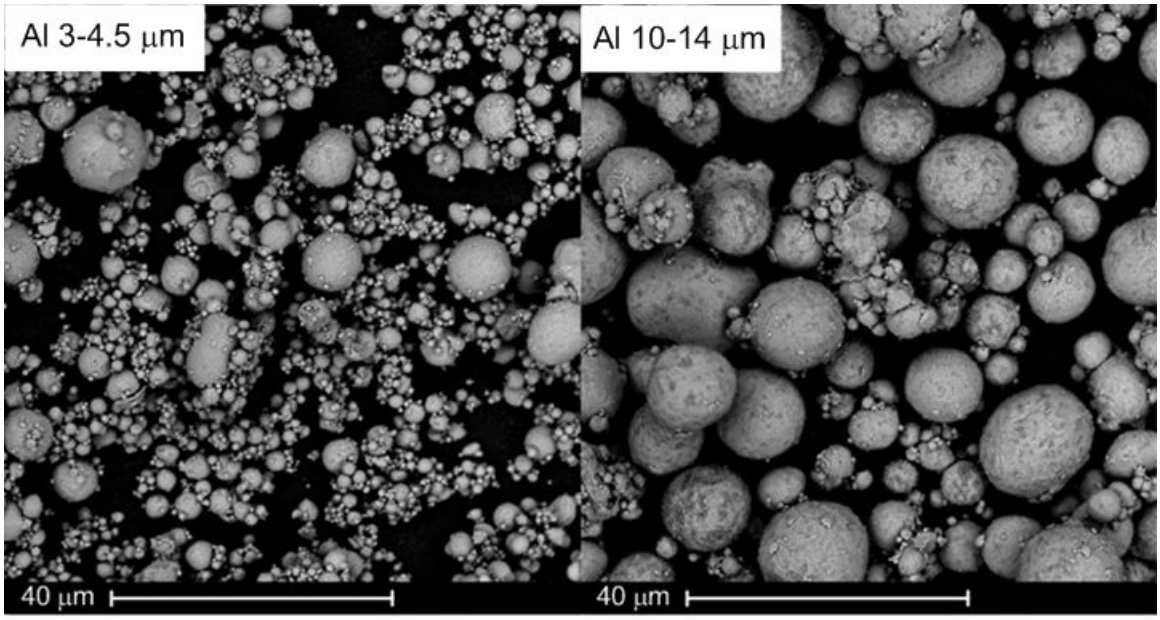

Figure 2.7 SEM images of Al 3-4.5 μm (left) and Al 10-14 μm (right).

2.8 Titanium Powder

Two Ti powder samples with different particle size distributions and morphologies were used: “sponge” powder from Atlantic Equipment Engineers, Inc. and spherical powder +150 mesh from Super Conductor Materials, Inc. Images of both powder samples taken with a scanning electron microscope are shown in Figure 2.8. The sponge powder particles are irregular in shape; many particles have sharp, jagged surfaces. Some agglomeration between particles is also observed. The spherical Ti powder contains large particles that are indeed mostly spherical and relatively well separated from one another. These two morphologies represent what is typically commercially available for Ti.

The particle size distribution for the Ti sponge powder was measured by low-angle laser light scattering using Coulter LS 230 analyzer. Spherical powder was too coarse for LS 230 and its particle size distribution was measured by processing microscopic images of the powder. The images were acquired using a Phenom scanning electron microscope (SEM) by FEI Co. The particle size distributions are shown in Figure 2.9. The volume mean diameters for the sponge and spherical powders are 30 and 82 μm, respectively. The sponge powder has a broader size distribution than the spherical powder. Also, the sponge powder contains small particles down to a micron in size, while the spherical powder has very few small particles, but has particles with diameters up to a 100 μm.

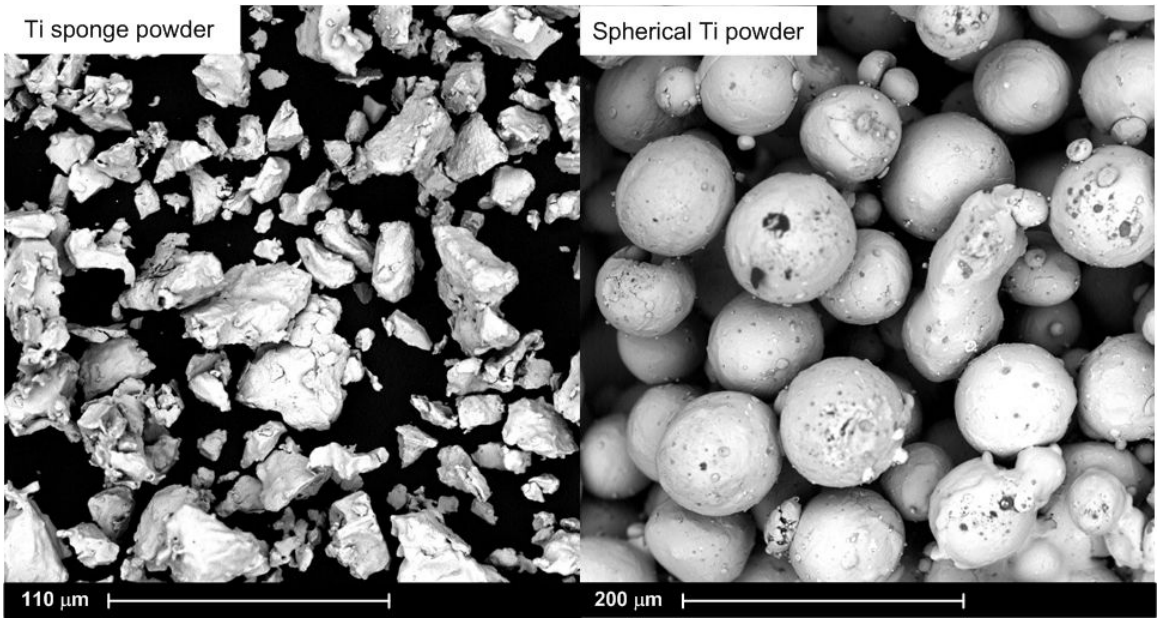

Figure 2.8 SEM images of Ti sponge powder (left) and spherical Ti powder (right).

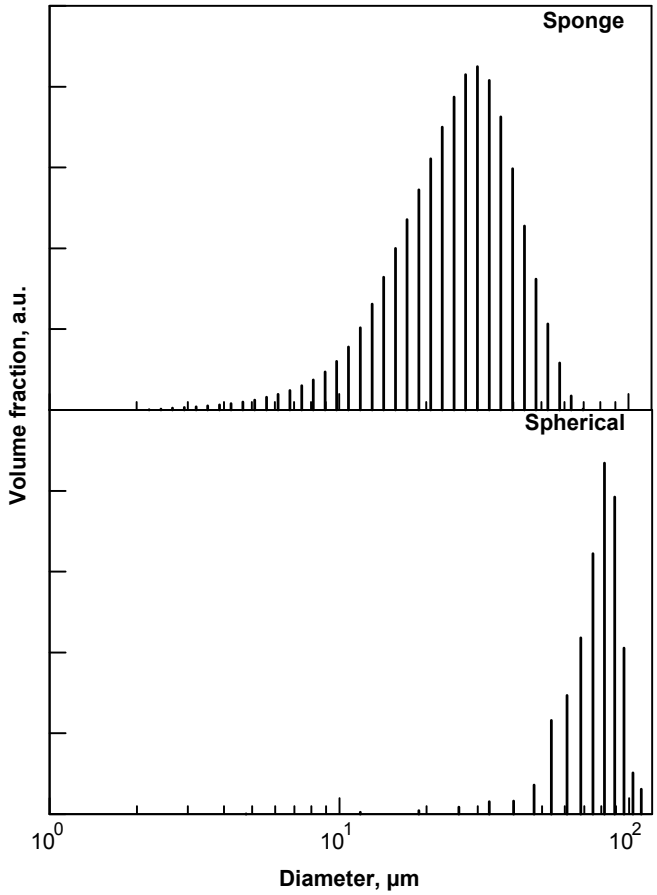

Figure 2.9 Particle size distributions for Ti sponge and spherical powders.

CHAPTER 3

ESD STIMULATED IGNITION OF MAGNESIUM POWDER

3.1 Results of Magnesium Experiments

3.1.1 Powder Ejection

Initial ignition tests showed that a portion of the powder placed in a sample cup is ejected from the cup for both ignition and non-ignition cases. A small crater, of about 1-3 mm diameter was always formed at the location where the spark struck the powder. Examples of the produced craters for the powder placed in the standard sample holder are shown in Figure 3.1. The electrode cup on the left shows powder that has not been struck by a spark. The middle cup shows Mg powder that has been struck by a spark but did not ignite. A crater of about 3 mm diameter is clearly seen in the center of the cup. The cup on the right shows Mg powder that has been struck by a spark and the spark energy was sufficient to ignite the powder. A crater of about 3 mm diameter is again observed in the center of the cup. There is also a white oxide layer covering almost the entire powder surface. It should be noted that the oxide layer formed after the spark was over while the powder away from the crater was burning for several seconds. Note that when the 6 mm diameter, custom sample holder was used the powder ejection and crater formation were observed, similar to the case illustrated in Figure 3.1. For the smaller, 2.1 mm diameter sample holder, the ejection resulted in effective removal of the entire powder charge from the sample holder.

To determine the velocity of the ejected particles, the sample was illuminated using a modulated green laser sheet placed perpendicular to the powder sample holder.

The spark energy was kept lower than the powder ignition threshold. Ejected, but not ignited particles scattered the laser light and were photographed using a digital camera with an open shutter. It was observed that the initial velocities at which the particles moved (measured about 1 mm from the powder surface) varied from 30 to 70 cm/s. The velocities were not affected by the spark voltage, systematically varied in these experiments.

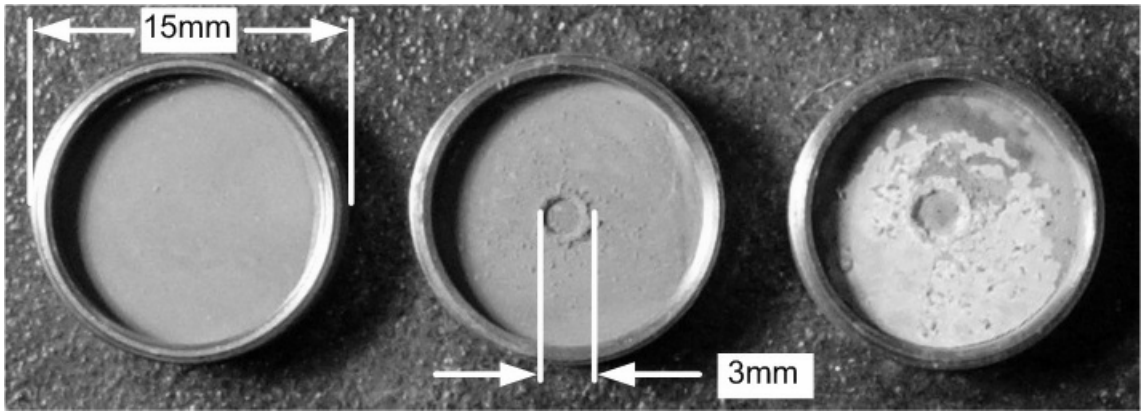

Figure 3.1 Electrode cups (15 mm diameter) containing Mg powder; left cup contains powder that has not been struck by a spark, middle cup contains powder that has been struck by a spark and has not ignited, and the right cup contains powder that has been struck by a spark and has ignited.

The ejection of powder by the spark resulting in the formation of the central crater can be attributed to the effect of the spark-produced shock wave [34]. This shock wave passes through the powder layer, reflects from the bottom of the sample holder and the powder becomes accelerated and is lifted by the pressure produced in the reflected wave. The role of the powder ejection in the ignition mechanism has not been previously discussed in the literature.

3.1.2 Observable Ignition

Different criteria are used to identify ignition for different powders. It could be appearance of individual particle streaks, emission with the color or spectral signature different from that of a spark striking an empty sample holder, or formation of a self-sustaining flame consuming the entire sample. Selection of a particular criterion is not straightforward. For example, it was observed that detectable streaks can be produced even when a spark strikes an empty sample holder that has a roughened surface, as illustrated in Figure 3.2.

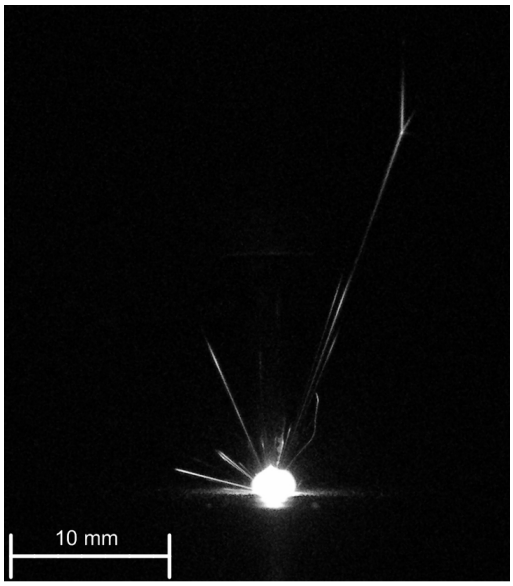

Figure 3.2 Still image of streaks produced from a roughened stainless steel cup holder.

Therefore, discrimination of such streaks, produced by fine particles eroded from the sample holder itself from the streaks representing igniting (and not simply heated up) powder particles is difficult. This issue was essentially removed by selecting Mg powder for the initial experiments. For Mg powder, ignition reproducibly results in formation of a self-sustaining flame consuming most of or the entire powder sample placed in the holder. A photograph showing an example of the produced flame is shown in Figure 3.3.

Individual particles can be seen burning; particularly large particles surrounded by flames appear as the white fire balls surrounding dark spots which are the particles themselves. In addition smaller particles can be seen burning along the periphery of the cloud as well many faint streaks correspond to particles that are not burning but scattering the light produced by the flame. Flame formation for Mg powder was also accompanied by a clearly detectable signature in the recorded photodiode signal as discussed in further detail below.

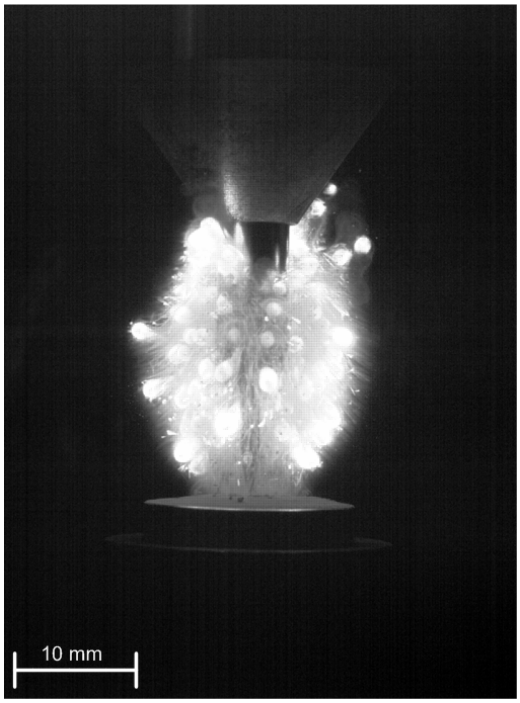

Figure 3.3 Still image taken from a high speed video showing ignition of individual particles within the Mg cloud aerosolized by the spark shockwave which results in a bright white flame.

3.1.3 Circuit Impedance and Measured Spark Energy

Current and voltage measurements were used to determine the total spark energy. In addition, the spark/powder impedance was roughly evaluated from processing the recorded current traces. The spark/powder system was assumed to be represented by an

LRC series circuit, with constant values of resistance, *R*, inductance, *L*, and capacitance, *C*. Figure 3.4 shows typical experimental traces for the current and voltage. In addition, the best fit trace for the current signal is shown.

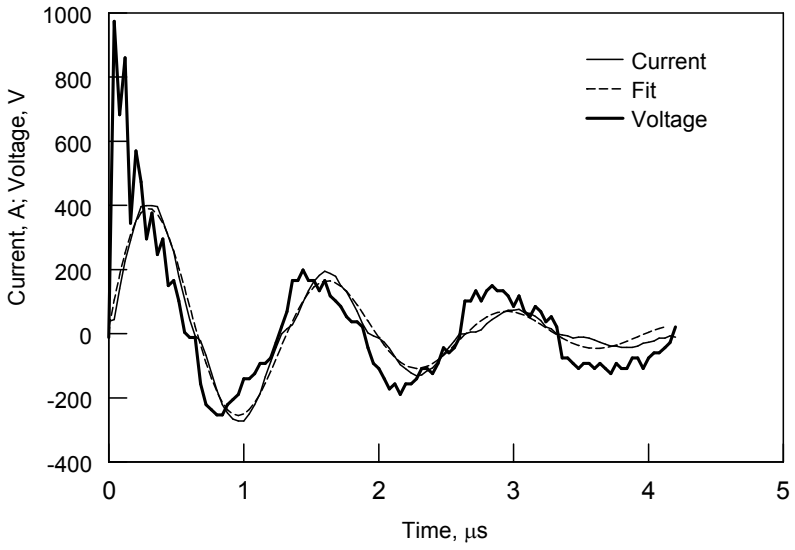

Figure 3.4 Experimental current and voltage traces for a spark and a current trace obtained fitting the experimental data and assuming the spark as a series LRC circuit.

The fit was obtained using the equation of current for an LRC series circuit with no voltage source applied after the capacitor is charged to a specified voltage [35]:

$$I(t) = -\frac{2CV_A}{\sqrt{4LC - R^2C^2}} \cdot \sin\left(\sqrt{\frac{1}{LC} - \frac{R^2}{4L^2}}t + \theta\right) \cdot \exp\left(-\frac{R}{2L}t\right) \tag{3.1}$$

where *I(t)* is the spark current as a function of time, *t*; V_A is the voltage applied to charge the capacitor, and θ is the phase angle. The values of *L*, *R*, and *C* were adjusted to obtain the fit of the current trace predicted by Equation (3.1) and the experimental trace. Note that in order to produce estimates meaningful for description of spark ignition events, it should be recognized that the assumption of the constant impedance made above to find the *L, R,* and *C* values by matching the experimental current trace and prediction using

Equation (3.1) cannot be entirely accurate. The impedance of the spark/powder system is likely to change in time, both due to substantial changes in the conductivity of non-equilibrium plasma existing in the spark gap [36-37], and due to changes in the properties of Mg powder while it is being heated and melted. In initial analyses it was noticed that the quality of match between the experimental and calculated curves (as shown in Figure 3.4) was consistently different for the earlier and later spark times. The earlier times play a greater role for the energy transfer from the spark to the powder, both because of the initially higher conductivity of the spark kernel [36-37] and because of the rapid decrease in the amplitude of the discharge current with time. Therefore, to obtain the current fitting curves and identify the values of *R, L,* and *C*, most useful for description of the energy transfer from the spark to powder, the experimental current and voltage traces were truncated to remove weaker oscillation periods observed by the end of the recorded signal. This resulted in a description matching better with the experimental current at the earlier times.

The spark energy was determined as:

$$E = \sum IV\Delta t \tag{3.2}$$

where the summation was performed over the entire spark duration with the time step Δt equal to the sampling time of the digital oscilloscope and using the recorded values of I and V as a function of time. For all current and voltage measurements the time step was Δt = 40 ns. Equation (3.2) estimates the true or active portion of the total released energy available for heating the conductive elements of the circuit. It does not include the reactive energy, which might result in some losses through electromagnetic radiation

produced by the phase-shifted components of the current and voltage existing due to the inductive nature of the spark circuit impedance.

3.1.4 Measured Spark Energy as a Function of Capacitor Energy

Similar measurements were performed and processed for empty sample holders and for the sample holders with Mg powder. The results of this signal analysis and obtained values of the spark energy for sample holders with Mg powder are shown in Figure 3.5.

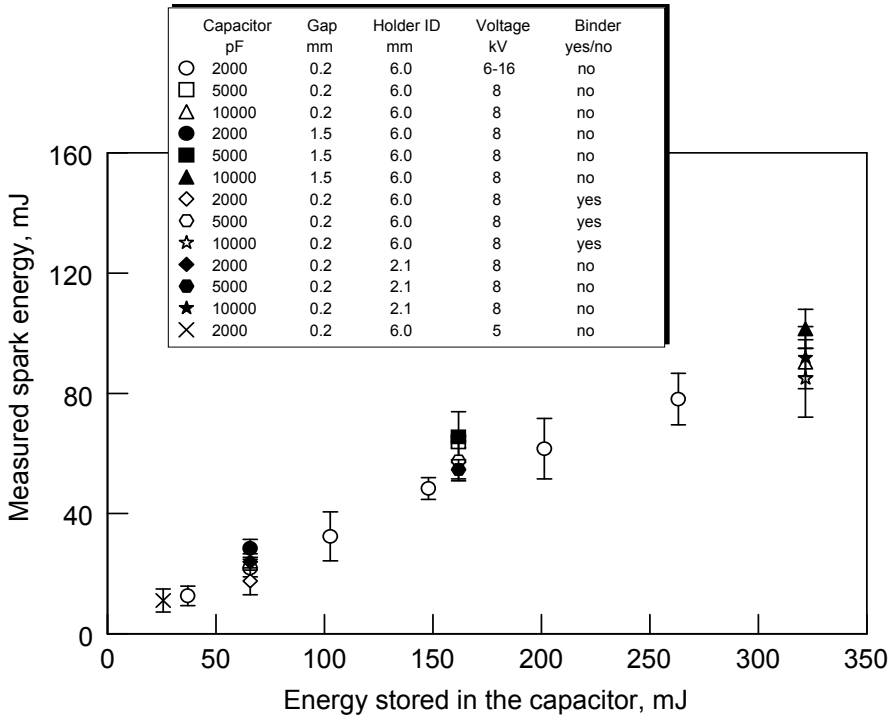

Figure 3.5 Measured active spark energy as a function of the energy stored in the capacitor for sample holders filled with Mg powder.

Each measurement was repeated 10 times. The error bars show one standard deviation of the 10 repetitions. It is observed that the measured spark energy is about 1/3rd of the energy stored in the capacitor. The results of the current signal analysis and obtained values of the energy for a spark striking the sample holder without powder are shown in Figure 3.6. Each measurement was repeated 10 times. The error bars show one

standard deviation of the 10 repetitions. Only about $1/6^{th}$ of the capacitor's energy is recovered as determined from the recorded current and voltage traces and using Equation (3.2). A small part of the capacitor's energy is unaccounted for because of the truncated current trace. It is also possible that the capacitor retains some small charge after the spark discharge is over. Furthermore, it is hypothesized that a substantial part of the capacitor's energy is unaccounted for by Equation (3.2) due to the inductive nature of the spark's impedance. Slightly higher measured spark energies correspond to the longer spark gap, while the effect is weak. No effect of the sample holder size can be detected.

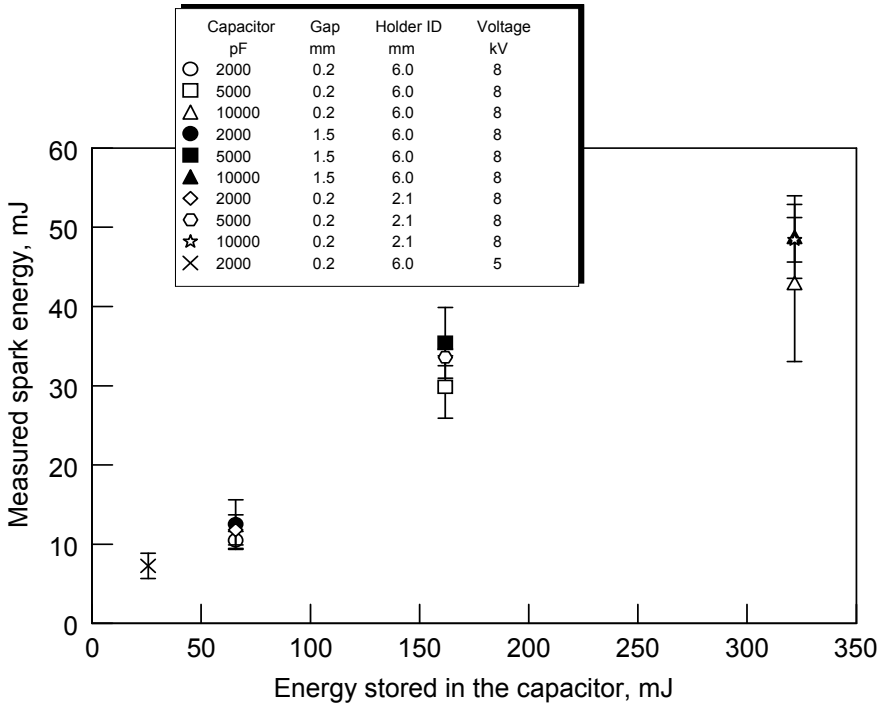

Figure 3.6 Measured active spark energy as a function of the energy stored in the capacitor for an empty sample holder.

3.1.5 Spark Impedance and Powder Resistance

The spark impedance values obtained from matching the current traces using the current description given by Equation (3.1) are shown in Figures 3.7 and 3.8 for empty and filled sample holders, respectively. The capacitance shown is a correction to the pre-set capacitance of the FTS required for the best fit for the measured current trace using Equation (3.1). Clear trends of reduced resistance and inductance and increased capacitance at the higher spark energies are observed. The effect of the spark gap on the determined spark impedance is negligible.

Additional experiments were conducted with the spark gap shorted by moving the discharge pin until the pin tip touched the sample cup. The impedance determined in these experiments matched the impedance shown in Figure 3.7 for the respective capacitors used. Therefore the measured impedance is primarily determined by the internal FTS circuit and connecting wires.

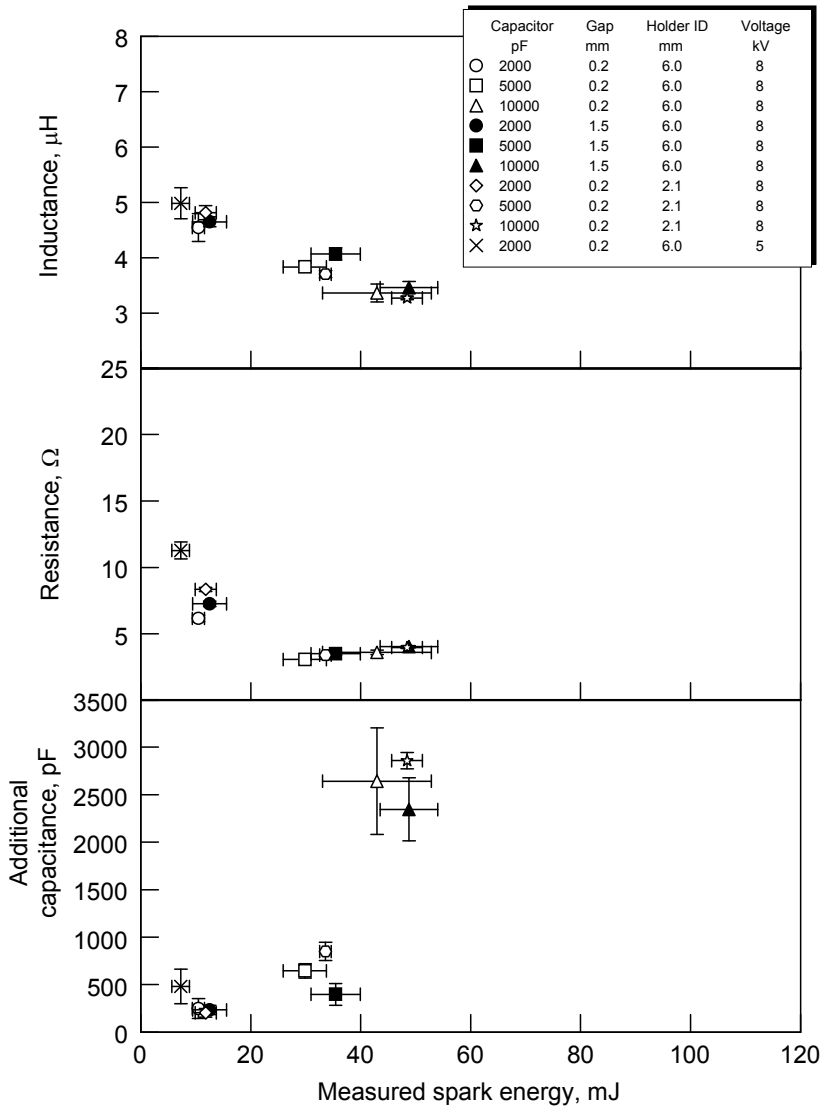

Figure 3.7 Circuit impedance as a function of the measured spark energy for experiments with empty sample holders.

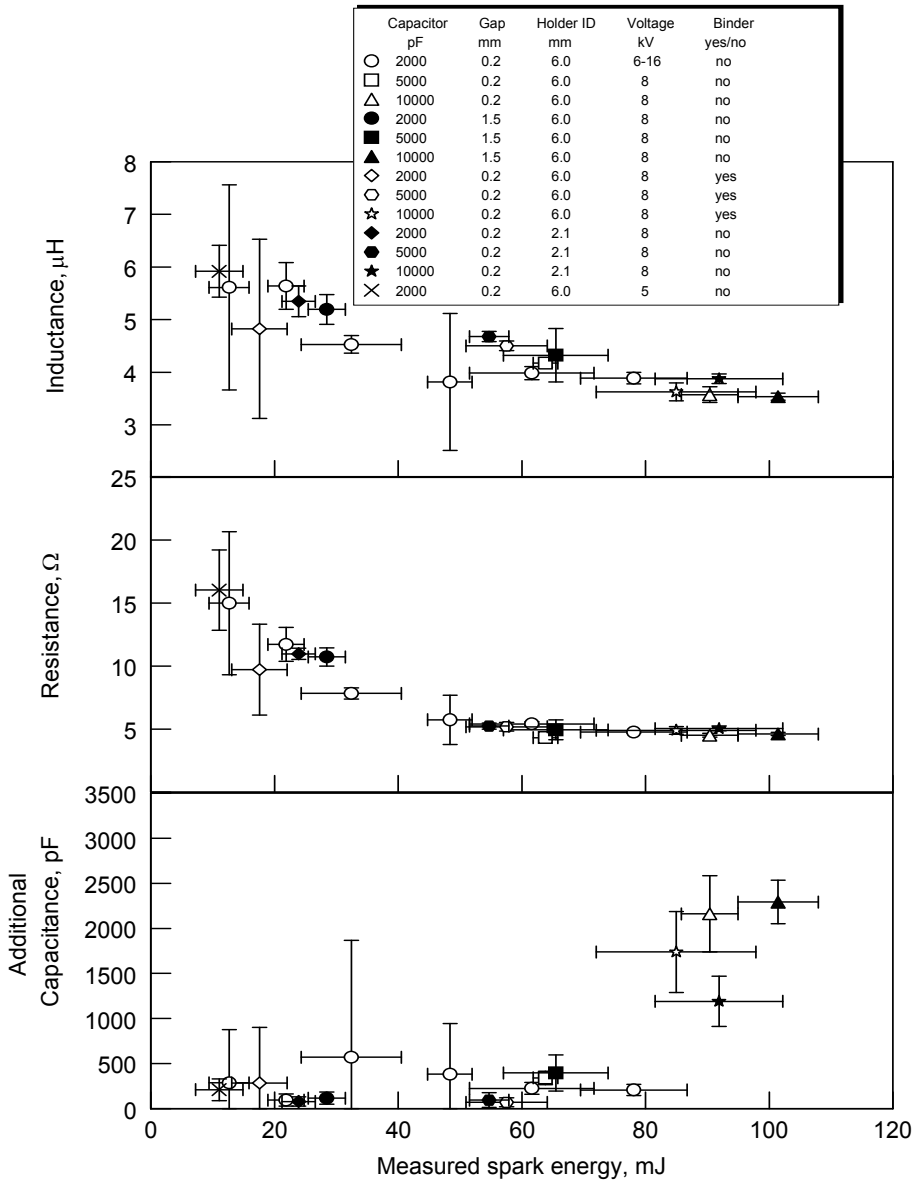

Figure 3.8 Circuit impedance as a function of the measured spark energy for the experiments with igniting Mg powder.

For experiments with Mg powder, impedance values are shown in Figure 3.8. Results are shown for ignited Mg placed in both 2.1 and 6 mm diameter custom-made sample holders with the latter used with and without binder added to the powder. In addition, results obtained for measurements with different spark gap lengths are shown. It is observed that adding powder slightly increases the values of resistance and

inductance necessary to fit the experimental data with the shape predicted by Equation (3.1) for all spark energies. This is consistent with the observed greater portion of the capacitor's energy recovered as calculated by Equation (3.2). There is no detectable effect of the spark gap or binder on the resistance and inductance values. The trends of reduced inductance and resistance and increased capacitance with increased spark energies are clearly visible and similar to those observed from Figure 3.7. The measured increase in the circuit resistance for the filled sample holder as compared to an empty one was used to estimate the added resistance produced by the powder load. This resistance was used in Equation (3.3) to estimate the energy released in the powder as a result of its direct Joule heating by the spark current.

The correction for the capacitance value is relatively small for all, except for the largest used capacitor (10,000 pF), for which it reaches about 20% of the capacitor value. In most cases, the additional capacitance decreases with powder included. Binder addition and sample holder size do not have a clear effect on the additional capacitance.

The values of inductance on the order of a few μH are consistent with the measurements reported in [38] for a similar spark configuration. The relatively large additional capacitance values in Figures 3.7-3.8 are clearly not affected by powder or powder/binder mixtures. The additional capacitance values are mostly likely associated with deviations of the capacitor characteristics from their nominal values, stray capacitances produced by the contact between the aluminum substrate and sample holder support, and parasitic capacitance of the output circuit of the FTS. The effect of stray capacitance is further supported considering that the two custom sample holders with

different size aluminum substrates and different contact areas were characterized with consistently different capacitance corrections based on experiments.

The equivalent resistance produced by the powder load, R_p, was determined from comparison of the circuit impedance measured with and without powder. Knowing R_p enabled the energy estimate resulting in the direct Joule heating of the powder by the spark current:

$$E_J = \sum I^2 R_p \Delta t \tag{3.3}$$

3.1.6 Minimum Ignition Energy

The experiments using the standard sample holder and spark gap of 0.2 mm suggested by the standard procedure [26] established the minimum ignition energy for Mg powder to be 25 mJ. This value is the energy stored in the capacitor. The measured spark energy available to the powder is 11 mJ and the energy delivered to the sample from Joule heating is 5 mJ.

3.1.7 Ignition Delays

It was observed that the optical signal produced by the ignited powder was noticeably delayed following the spark emission and current traces. The ignition delay is illustrated in Figure 3.9. The top plot shows the initial (shaded) portion of the recorded signal with the logarithmic time scale, so that it is clearly observed that the emission decreases to its baseline level after the spark and the ignition peak is only detected after a substantial delay. The delay times were measured using the recorded emission traces. Two different signal processing techniques were used and respectively two different values of ignition

delays were obtained for each of the recorded traces. In both cases, the baseline signal level was determined as the signal recorded prior to the spark ignition.

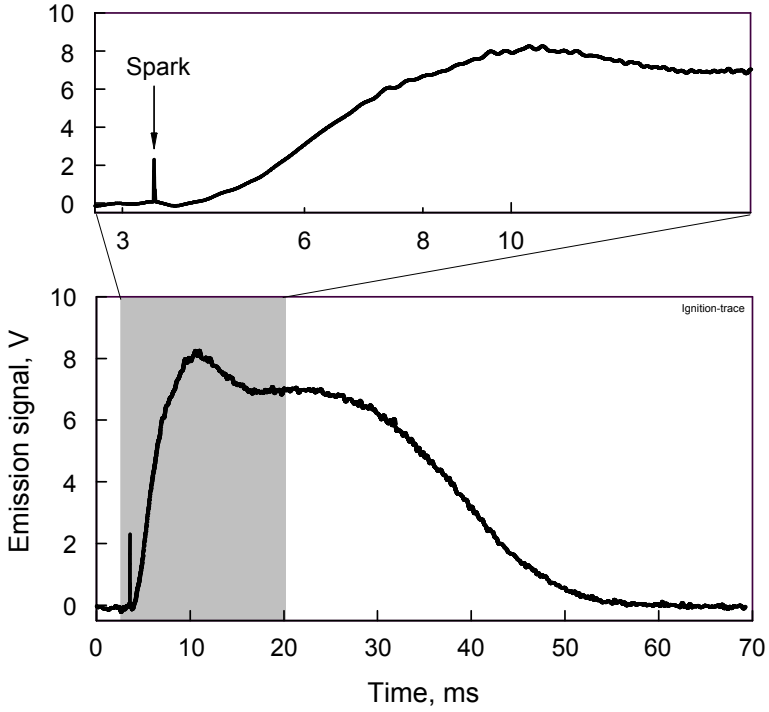

Figure 3.9 An emission signal produced by a spark-ignited Mg powder. A shaded portion of the signal is expanded with a logarithmic horizontal time scale to clearly illustrate a short spark pulse preceding a broad peak produced by Mg ignition.

In the first method, ignition was assumed to occur when the emission signal increased abruptly. Thus, the rate of ensuing combustion affecting the slope of the emission signal influenced the identification of the ignition moment. To find the delay by this method, a time derivative of the emission signal was obtained and both the instant and signal value of the emission trace corresponding to the maximum in its derivative were found. The signal slope at this point was projected as a straight line to cross the baseline signal level, as illustrated in Figure 3.10, so that the ignition delay could be determined.

In the second method, ignition was assumed to occur when the emission signal produced by the ignited powder exceeded the baseline signal. Specifically, the ignition instant chosen was when the emission signal following the spark increased 3 standard deviations above the baseline level, as also illustrated in Figure 3.10.

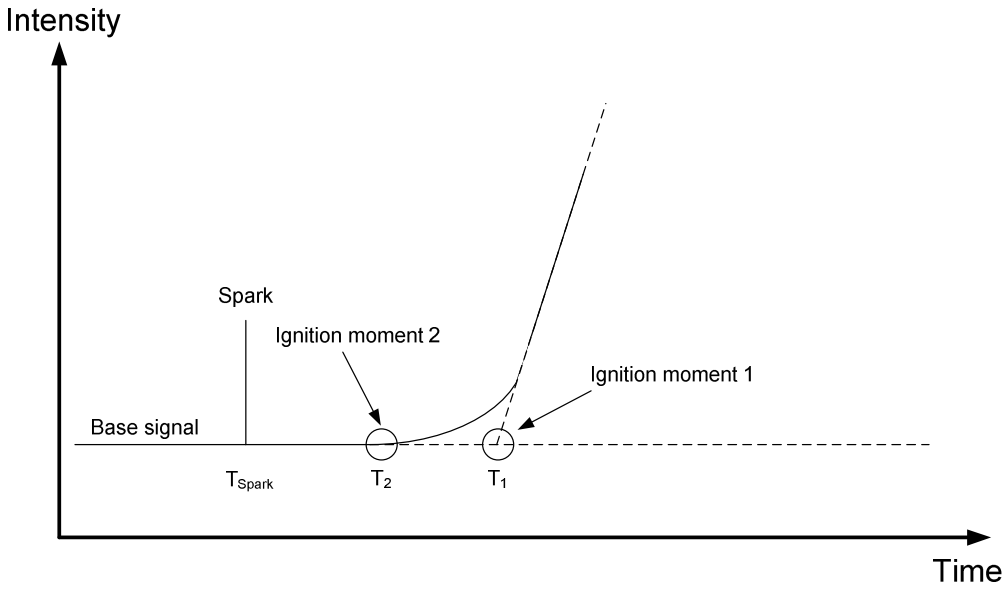

Figure 3.10 Illustration of the two methods used to determine ignition delay. First method: the ignition moment is identified as the point where the projection of the maximum slope of the 500-nm emission signal intersects the baseline. Second method: the ignition moment is identified when the 500-nm emission signal exceeds the baseline more that 3 standard deviations of the baseline level. The ignition delay is the time difference between the spark and ignition moment.

Figures 3.11-3.12 show ignition delays versus measured spark energies for loose Mg powder in the 6 mm diameter sample holder where delays are determined by methods 1 and 2, respectively. Ignition delays vary in the range of 0.5-3 ms and correlate with the measured spark energy, with shorter delays corresponding to greater spark energies. This trend is also observed in experiments with Mg/binder in the 6 mm diameter sample holder and loose powder in the 2.1 mm diameter sample holder, as shown in Figures 3.13 and 3.14, respectively. Results presented in Figures 3.11 and 3.12 show no effect of the

spark gap on ignition delay. Ignition delays are shorter in Figures 3.13-3.14 as compared to Figures 3.11-3.12 (loose powder on a 6 mm diameter sample holder). Interestingly, the effect of the spark energy on the ignition delay for experiments with binder is different from that for the loose powder. For the powder with binder, the ignition delay continues to decrease when the spark energy increases above 60 mJ (Figure 3.14); at the same time the ignition delay becomes roughly constant above 60 mJ for the loose powder (Figures 3.11-3.12). The specific value assigned to the ignition delay is affected by the method used for its quantification.

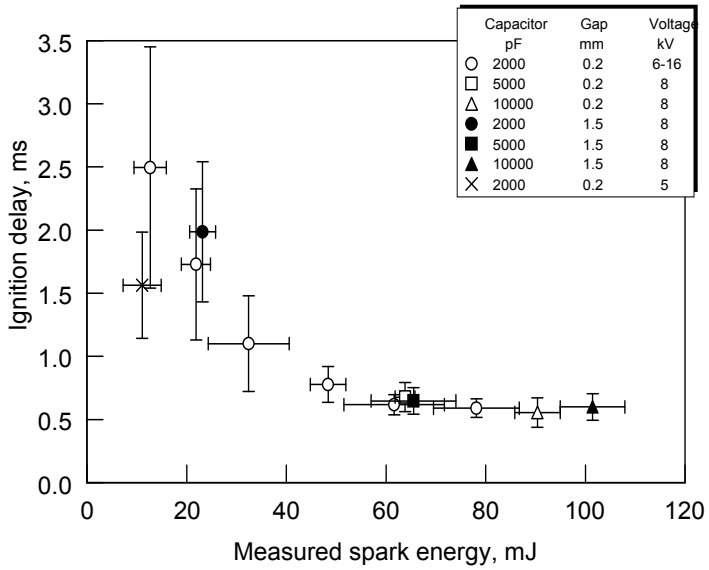

Figure 3.11 Ignition delay (method 1) as a function of the measured spark energy for experiments conducted with the 6 mm diameter sample holder and no binder.

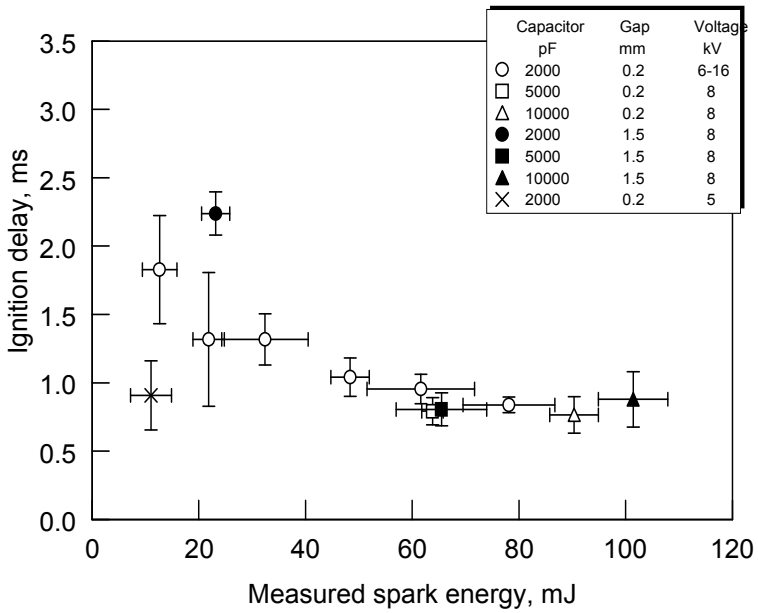

Figure 3.12 Ignition delay (method 2) as a function of the measured spark energy for experiments conducted with the 6 mm diameter sample holder and no binder.

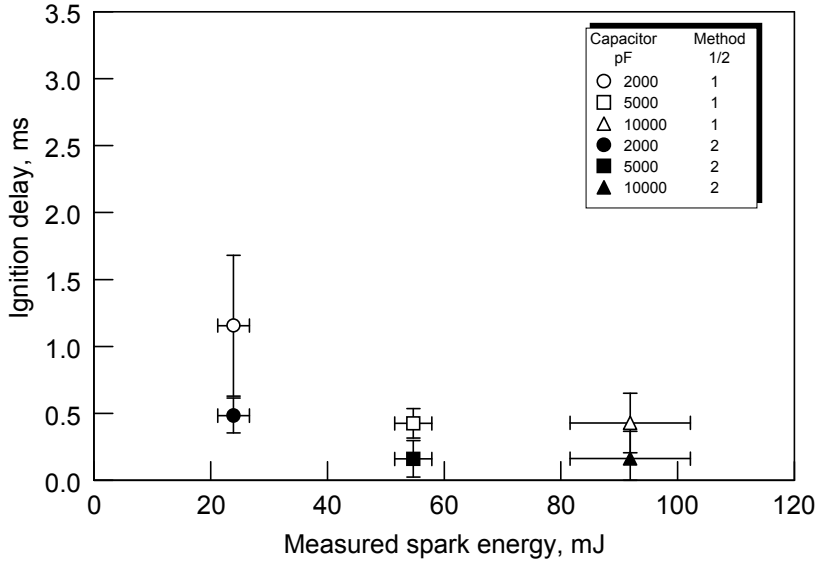

Figure 3.13 Ignition delay (both methods) as a function of the measured spark energy for experiments conducted with the 2.1 mm diameter sample holder and no binder at 8 kV and a gap of 0.2 mm.

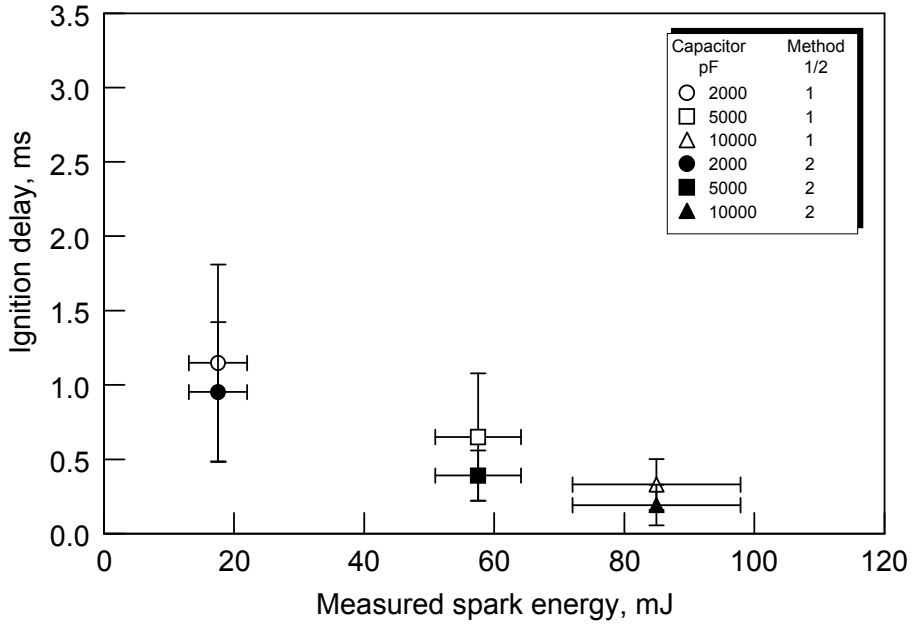

Figure 3.14 Ignition delay (both methods) as a function of the measured spark energy for experiments conducted with the 6 mm diameter sample holder and binder at 8 kV and a gap of 0.2 mm.

3.2 Interpretation of Magnesium Experimental Results

3.2.1 Direct Joule Heating of the Powder by the Spark Current

The experimental data were processed to determine the portion of the spark energy delivered to the powder as a result of its direct Joule heating by the spark current, as described by Equation (3.3). The energy calculated by Equation (3.3) is shown in Figure 3.15 versus the measured spark energy determined using Equation (3.2). A line where both energies are equal to each other is also shown for reference. For the experiments with binder, the values of Joule heating energy and the total spark energy are approximately the same. A slightly higher Joule heating energy as compared to the measured spark energy observed for a couple of points is indicative of an inaccuracy in quantifying the powder resistance for cases when the binder was used. For the

experiments with no binder used, the Joule heating energy varies from 50 to 90 % of the total measured spark energy.

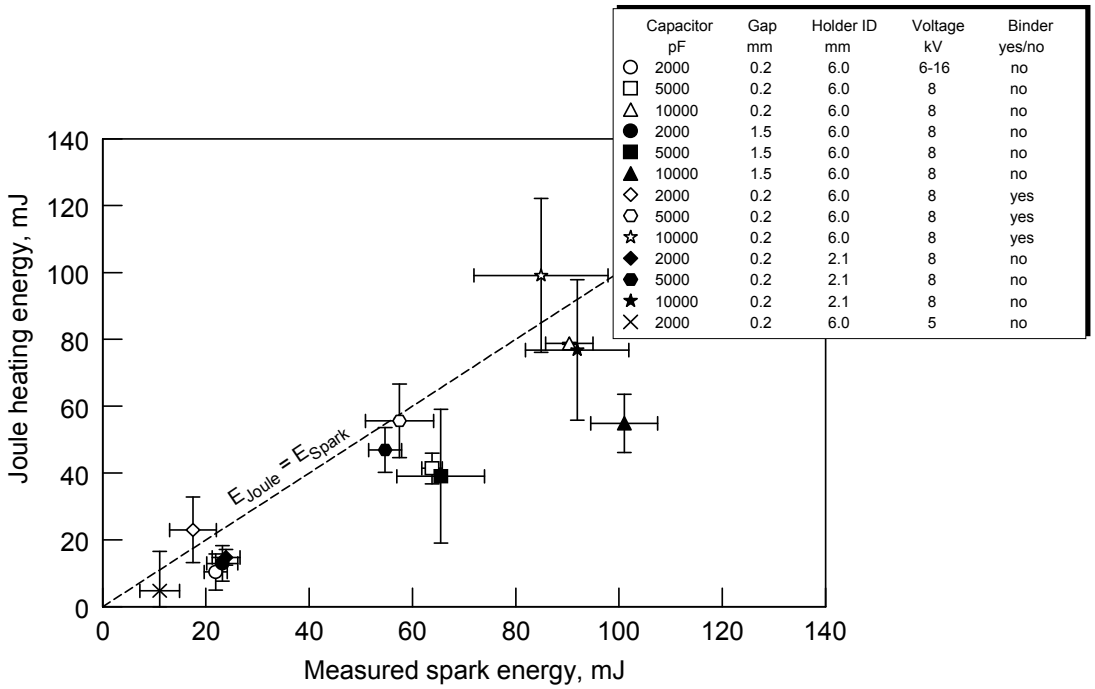

Figure 3.15 Joule heating as a function of the measured spark energy.

Note that there is a correlation between the generic trends observed for ignition delays and the Joule heating energies: the experimental configurations characterized by greater Joule heating energies (smaller sample holder, binder used) are also characterized by shorter ignition delays.

The energy transferred to the powder as a result of its Joule heating is substantial and must result in its significant heating. The role of this heating in triggering powder ignition is further discussed below.

3.2.2 Powder Heating and Ignition by the Spark

Spark discharge breaks down the air gap producing a relatively narrow (~ 100 μm diameter) [37, 39] plasma channel with a small resistance. When an empty sample holder is used, this channel is reaching the metal surface with electrical resistance negligible compared to that of the plasma. However, when metal powder is placed in the sample holder, its electrical resistance is much greater than that of a bulk metal because of the substantial contact resistance between adjacent particles. Thus, in order to achieve comparable currents in both cases, the spark plasma must be extended through the powder layer. In other words, local micro-discharges occur between particles placed under the plasma channel, effectively reducing the contact resistance between these particles. The local discharges between the particles serve as hot spots heating the powder during the spark discharge, while the resistance of the individual particles is much smaller so that their Joule heating by the current existing inside the particles is negligible.

Assuming that the spark discharge for multiple local micro-discharges described above directly heat only the powder layer directly under the plasma channel, both radius, R, and initial temperature, T_{in} of the directly heated powder cylinder can be estimated. This estimate will use the experimentally determined minimum ignition energy for the spark ignition of Mg powder.

First, note that the distance the heat can travel within the powder during the spark duration is negligible. Indeed, using the thermal diffusivity for a Mg powder layer measured to be, $\alpha = 2.29 \times 10^{-7}\, m^2/s$ [29] it can be readily estimated that in τ = 1 μs (characteristic spark duration) the heat can only travel within the powder for about

$\sqrt{\alpha\tau} \approx 0.5$ μm. Thus, for a crude estimate it can be assumed that the powder cylinder of a fixed radius, R, is heated adiabatically and uniformly by the current passing through it. The height of the cylinder, H, is taken to be 0.5 mm, which is close to the height of the powder sample placed in the sample holder. For such a cylinder, the temperature achieved as a result of its Joule heating will be a function of the cylinder radius, R, as expressed by Equation (3.4):

$$\begin{aligned} &if\ T_{in} < T_m; \quad T_{in} = T_0 + \frac{E_{Joule}}{\pi\rho\eta C_{PS} R^2 H} \\ &if\ T_{in} > T_m; \quad T_{in} = T_m + \frac{E_{Joule}}{\pi\rho\eta C_{PL} R^2 H} - \frac{C_{PS}}{C_{PL}}\left(T_m - T_0\right) - \frac{L}{C_{PL}} \end{aligned} \tag{3.4}$$

where T_0 is the initial powder temperature assumed to be equal to the room temperature, 298 K, T_m = 923 K is the magnesium melting temperature, η is packing density, and for densely packed spheres η = 0.75, $C_{PS} = 1023\,{}^{J}\!/_{kg \cdot K}$ and $C_{PL} = 1411\,{}^{J}\!/_{kg \cdot K}$ are the values of specific heat for solid and liquid magnesium respectively, L=357.9 kJ/kg, is the latent heat of melting for magnesium, E_{Joule} is the spark energy released in the powder as a result of its Joule heating, and $\rho = 1738\,{}^{kg}\!/_{m^3}$ is the Mg powder density. Assuming that E_J = 5 mJ corresponding to the experimentally determined minimum ignition energy, a correlation between T_{in} and R is obtained and plotted at the top of Figure 3.16

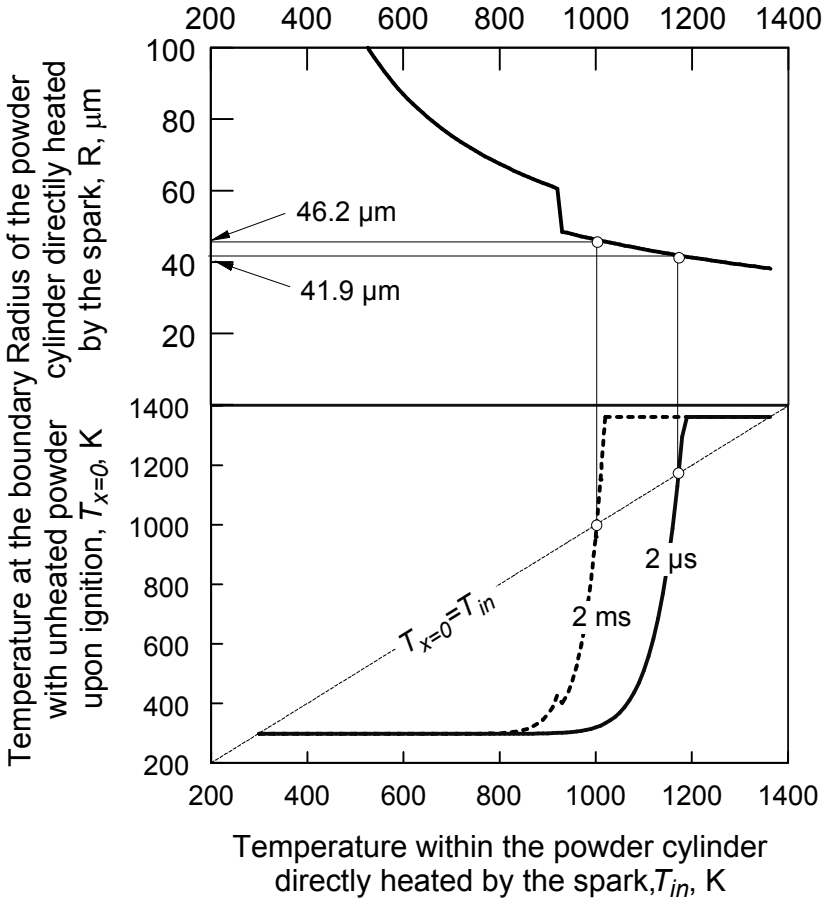

Figure 3.16 Illustration for evaluation of the radius of the powder cylinder directly heated by the spark. The top plot shows how this radius changes depending on the temperature achieved in the cylinder and assuming that the spark energy is equal to the minimum ignition energy for Mg. The bottom curves show temperatures at the boundary with the cold portion of the powder required to remove the heat generated by chemical reaction within the directly heated cylinder for the time delays of 2 μs and 2 ms.

Two different scenarios leading to the ignition of the heated powder can be considered. These two scenarios are illustrated in Figure 3.17. In one case, a particle heated by the spark is ejected from the powder layer and ignited in the surrounding gas. Respectively, to assess the temperature such a particle needs to be heated to, heat generated as a result of oxidation reaction should be balanced by radiation and convection heat losses to the surroundings. In another case, ignition of particles remaining inside the powder layer can be considered. In the latter situation, the heat

release due to oxidation should be balanced by the conductive heat transfer to the colder part of the powder layer. An ignition temperature required for each case can be estimated using the expression for Mg oxidation rate reported in the literature [29]. Further, because the temperature to which the particles in the powder layer are heated by the discharge depends on the discharge column diameter, the diameter corresponding to the ignition temperature can be estimated and compared to that expected based on the electrostatic discharge characteristics and respective literature references.

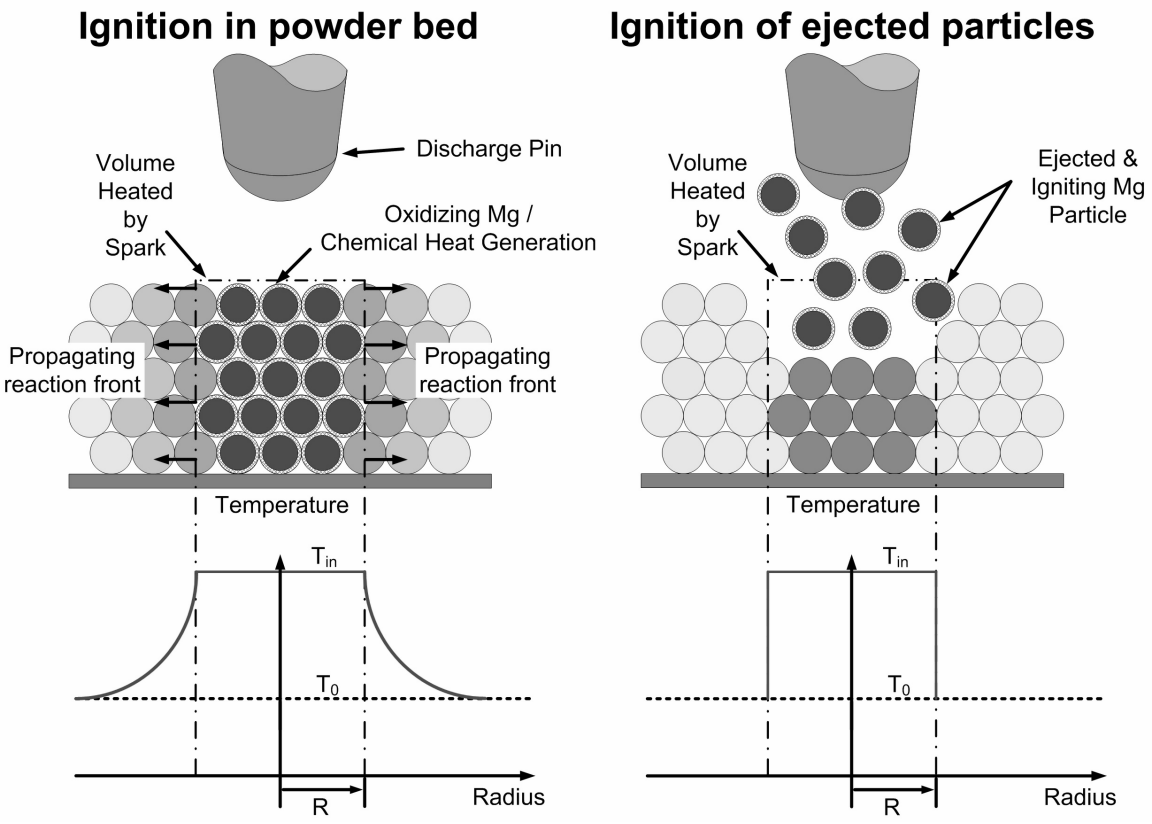

Figure 3.17 Ignition scenarios that can occur during experiment. The left image shows ignition occurring in the powder bed, where individual particles in the powder bed can chemically self heat and by conduction lose heat to the surrounding cold particles not directly heated by the spark. The right image shows ignition of individual particles that ignite in air, where ejected particles can chemically self heat and loses heat to the surrounding cold air and environment by convection and radiation, respectively.

Based on two different ignition scenarios outlined above (powder layer and single particle in the gas environment), two separate estimates are made. In the case of ignition in the powder layer, consider the heat balance between the powder heated by the discharge directly and the rest of the sample, assuming that the powder remains in the sample holder (i.e., neglecting powder ejection). The powder heated by the spark directly will start oxidizing and heat the rest of the sample. Assuming that the oxygen is available to the powder directly heated by the spark (after some ignition delay), the respective heat flux can be described as:

$$q_s^{"} = \frac{A}{A_v} Z \Delta H \exp\left(-\frac{E_A}{R_u T_{in}}\right) = \frac{3R\eta}{2r} Z \Delta H \exp\left(-\frac{E_A}{R_u T_{in}}\right) \tag{3.5}$$

where A is the area over which oxidation occurs equal to the total surface area of all the particles inside the directly heated cylinder and A_v is the surface area of the heated cylinder in contact with the rest of the surrounding powder; it is assumed that all particles have the same radius, r, equal to the mean radius of the powder used in experiments (5.15 μm), Z is the pre-exponent, ΔH is the enthalpy of oxidation, E_A is the activation energy, and R_u is the universal gas constant. The values of Z=10^{10} kg/m^2 s and E_A=215 kJ/mol are for Mg powder [29]. For powder ignition to occur, this heat flux needs to be balanced by the heat flux produced in the conductive colder powder outside of the directly heated volume. For a simple estimate, the transient temperature profile in that portion of the sample, T_x as a function of, x, the distance from the interface with the directly heated volume, can be approximately described by an analytical expression available for a semi-infinite solid heated at its boundary by a constant heat flux [40]. For x=0, the heat flux is expressed through temperature at the interface, $T_{x=0}$ as:

$$q_s'' = \frac{2}{k} \cdot \frac{\sqrt{\alpha t / \pi}}{T_{x=0} - T_0} \tag{3.6}$$

where α is thermal diffusivity, k is thermal conductivity, and t is elapsed time. The value of q_s'' can be taken as a function of temperature from Equation (3.5), so the radius R of the directly heated cylinder can be found, for which the Equation (3.7) below is satisfied:

$$T_{x=0} = T_{in}(R) \tag{3.7}$$

The elapsed time is assumed to be equal to the characteristic ignition delay, t=2 ms. For this time, Equation (3.7) is fulfilled for R = 46.2 μm. This calculation is illustrated in Figure 3.16. Another borderline case corresponding to ignition with a negligible delay, with the elapsed time close to the spark duration, t = 2 μs is also considered.

The simple estimates above can be used to assess the radius of the powder cylinder directly heated by the spark. Based on results presented in Figure 3.16, this radius is limited by 41.9 and 46.2 μm. This size compares well with the reported dimension of the plasma kernel produced in similar spark discharges [37,39].

The second estimate corresponding to the ignition of a single ejected particle is described below. To determine to what temperature the particle needs to be heated prior to its ejection so that it will ignite when exposed to cold air, a heat transfer balance between chemical reaction heat release and convective and radiative heat losses can be considered for an individual particle:

$$Z\Delta H \exp\left(-\frac{E_A}{RT_{Particle}}\right) = \frac{Nu}{D} k\left(T_{Particle} - T_\infty\right) + \varepsilon\sigma\left(T_{Particle}^4 - T_\infty^4\right) \tag{3.8}$$

where $T_{Particle}$ is the temperature of the particle that needs to be reached in order for ignition to occur, Nu is the Nusselt number, D is the particle diameter, k is the thermal

conductivity of air taken at the film temperature, T_∞ is the temperature of the surrounding air and surfaces, ε is the emissivity of the particle surface, and σ is the Stefan-Boltzmann constant. The particle is assumed to have a low Reynolds number and therefore the value of *Nu=2* is used corresponding to a stationary sphere. The temperature at which Equation (3.8) is satisfied is assumed to be the ignition temperature for a single Mg particle in cold air. Using the heat balance (3.8) it is estimated that for a particle of 10.3 μm diameter (the mean diameter of the Mg powder used in experiment) the ignition temperature is 1067 K. From the top curve shown in Figure 3.16, this temperature corresponds to the radius of the heated powder cylinder of approximately 45 μm, which is very close to the previous estimate.

Both estimates assuming ignition of the powder layer and of individual ejected particle produce very similar required spark discharge diameters implying that for the same spark source, ignition is to be observed at the same spark energy for both cases. Indeed, the experimental minimum ignition energy was not affected by the use of binder, which prevented particle ejection.

Assuming that the radius of the powder cylinder directly heated by the spark does not change significantly as a function of the spark energy, the ignition delays for different spark energies can be evaluated. It is generally clear that shorter delays will be predicted to correspond to the greater spark energies, as observed experimentally. However, the simple estimates are limited because once the powder in the volume directly heated by the spark starts boiling, the regime of heat transfer between this boiling powder and the colder external portion of the sample change substantially. It also is clear that the description of the oxygen transfer to the heated powder is of critical importance since this

transport will determine the rate of reaction in the powder cylinder directly heated by the spark, which, in turn, will likely determine the observed ignition delay. By using Equation (3.5) it was assumed that oxygen is available to the powder, while this may not be the case immediately after the spark is over. Indeed, the oxygen available for reaction is contained inside the porous powder layer. An estimate shows that if all this oxygen is consumed, the powder temperature can only be increased by about 2 K. Additional oxygen is therefore required and must be supplied by diffusion and/or convection flux which is likely established during the observed ignition delay.

3.2.3 Effect of Powder Ejection

Based on the observed velocities of the ejected particles, it can be concluded that the powder effectively remains in place during the spark. The particle velocities do not exceed 1 m/s, so the particles do not move more than 1 μm during the 1 μs long spark discharge. On the other hand, the particles do get displaced during the time comparable to the typical ignition delay. The displacement is of the order of 0.5-1 mm, which is close to the height of the sample. The powder ejection during the ignition delay affects the heat transfer between the powder heated by the spark directly and the rest of the sample. It can be generally expected that the heat transfer becomes less efficient when part of the directly heated powder is removed, resulting in longer ignition delays. This effect is qualitatively consistent with the results presented in Figures 3.14–3.16, shorter delays are observed for the powder with binder. Also, the delays at higher spark energies and no binder do not decrease with further increase in the spark energy, indicating that the powder removal due to ejection impedes the heat transfer within the powder more significantly at higher spark energies.

CHAPTER 4

ESD STIMULATED IGNITION OF ALUMINUM POWDER

4.1 Results of Aluminum Experiments

4.1.1 Spark Radius

For bulk metal targets (e.g., empty sample holders), the only readily detectable spark signature was a small molten pool, as illustrated for different materials in Figure 4.1. For each observed signature, its widest and narrowest dimensions were measured. These dimensions were treated as the major and minor axes of an ellipse. The ellipse area was calculated, and the radius of the circle with the same area as the ellipse was considered to represent the spark column radius. Readily detectable signatures were only formed at high spark voltages, exceeding the settings used in ignition experiments.

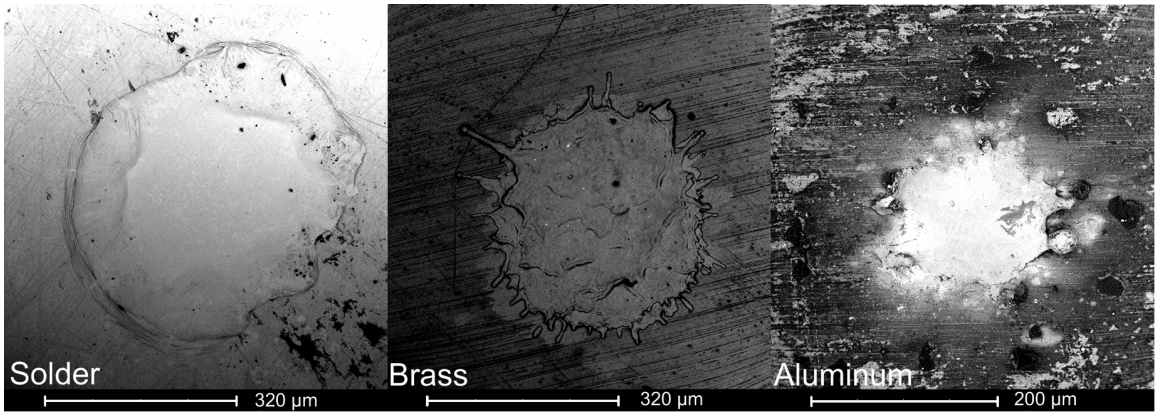

Figure 4.1 SEM images of spark spots striking solder (left), brass (middle), and aluminum (right).

For the soot-covered brass plates, detectable signatures could be obtained for a wider range of spark voltage settings, including those used for ignition measurements. For such targets, the spark resulted in cleaning of a portion of the soot, so that "bald" spots were formed and observed under SEM. Characteristic signatures obtained for

different spark energies are shown in Figure 4.2. Unlike the molten spots shown in Figure 4.1, the signatures observed on the soot-covered plates are discontinuous and include several spots located relatively close to one another. Such spots are likely produced by the individual streamers of the spark striking the surface. As the spark energy increases the individual streamer spot dimensions grow and spots appear to begin overlapping. To estimate the combined spark spot area, an image processing software, UTHSCSA Image Tool v 3.0 [41] was used. For each image, the image brightness was thresholded, so that bright spots became black whereas the rest of the image was white. The total number of the black pixels was then counted and transferred into the respective area. The equivalent spark radius was then calculated.

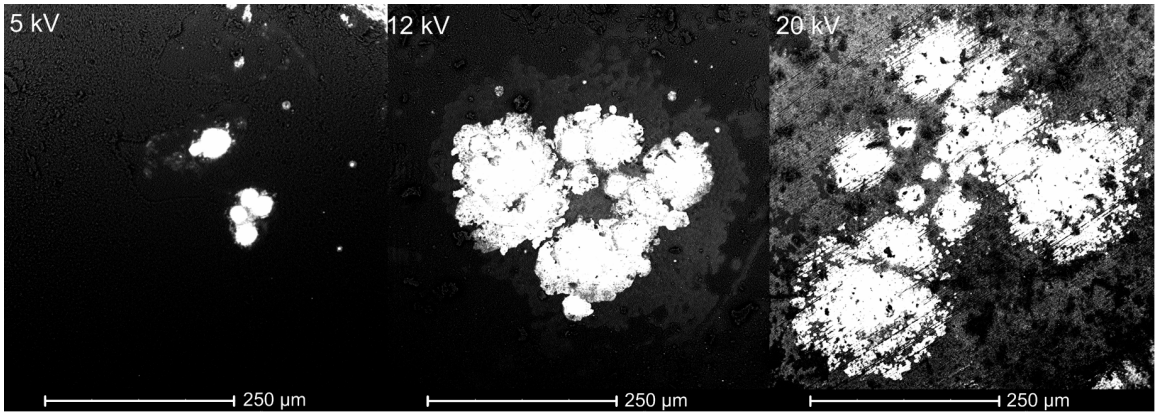

Figure 4.2 SEM images of spark spots striking soot covered brass plates at 5 kV (left), 12 kV (middle) and 20 kV (right).

Figure 4.3 shows a summary of the spark radius measurements obtained using different targets and different discharge voltages. For aluminum, solder, and for soot-covered plates, different voltage settings could be used, whereas for brass targets the signatures were only obtained at one voltage. For all targets, a smaller spark radius is observed for lower voltages. Comparing signatures for different targets obtained at the

same voltage, it is noted that the dimension of the signature increases as the melting point of the target material decreases. Because the imprints left on the soot-covered target do not depend on melting and appear to most accurately represent the spark signature, these measurements were taken as the most accurate representation of the equivalent spark radius. In particular, the equivalent spark radii were estimated to be 60 and 95 μm at 5 and 8 kV, respectively. The spark radii at the intermediate voltage settings used for ignition measurements were obtained by linear interpolation between the above values.

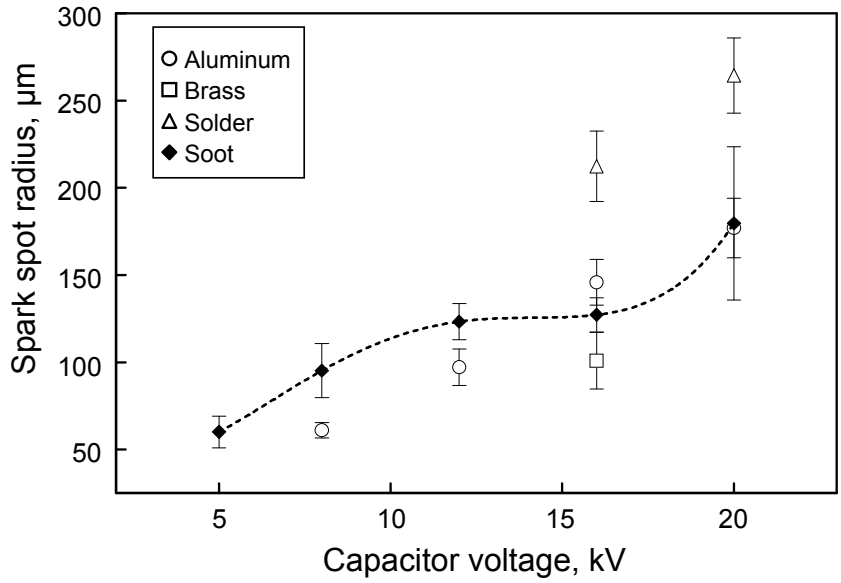

Figure 4.3 Equivalent spark spot radius as a function of voltage for different targets.

4.1.2 Image of Burning Particles

Visible streaks of the particles ignited by the spark are often used as a criterion for identifying the MIE for an ESD ignition. Figure 4.4 shows a set of still images with such streaks obtained during experimentation. Each image was taken at the spark voltage of 8 kV; the left image was recorded for a spark striking an empty steel sample holder, the middle and right images show streaks produced by igniting Al 10-14 μm powder. The

images on the left and in the middle show a bluish white glow corresponding to the light emission of the spark itself. The image on the right is mostly saturated and shows that the ignited powder produced an aerosol flame rather than individual igniting particles.

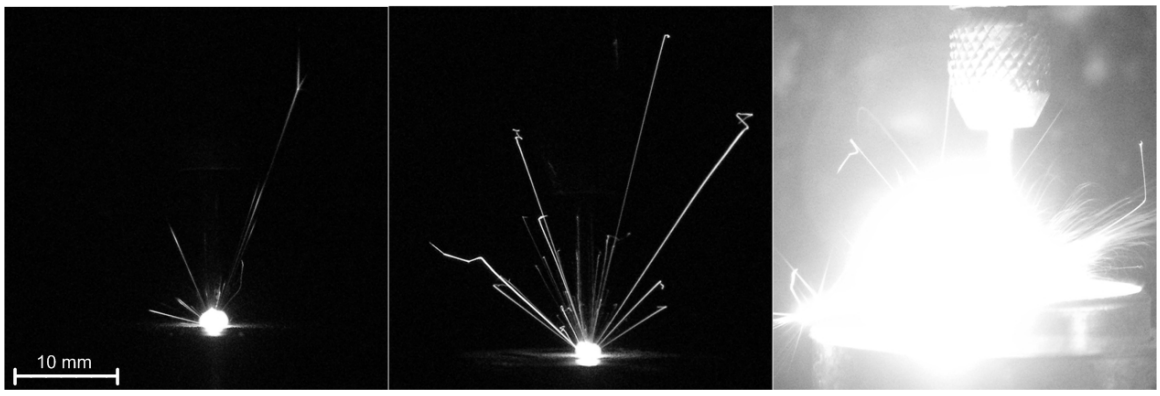

Figure 4.4 Images of streaks produced by the sparks striking an empty steel sample holder (left), and sample holder filled with 10-14 μm Al powder (center and right). All images were taken at a voltage of 8 kV.

Both the left and middle images show streaks of particles traveling away from the spark. As noted above, the left image is taken with an empty sample holder, and the streaks are produced by microscopic steel particles eroded from the sample holder surface. Note that such streaks disappear when the sample holder surface is polished using a fine sand paper (1200 grit). Because appearance of visible particle streaks is often considered as an indicator of ignition, it is important to realize that such streaks can be produced and detected even without metal powder being present. Therefore, a simple reference to the visible particle streaks should be considered inadequate as an ignition indicator.

Comparing streaks observed in the left and middle images, it is noted that there are fewer streaks on the left and they are noticeably dimmer than the streaks in the middle. Another distinguishing feature between the streaks produced by the eroding steel sample holder and igniting Al particles is that Al particle trajectories end with

characteristically curved streak portions. This feature was explicitly discussed in the literature, e.g., [42]. To avoid further confusion between the eroding sample holder and igniting Al particles, further experiments in which streaks were registered were performed with a custom-made brass sample holder. It was preliminarily tested and observed not to generate detectable streaks while being struck by the spark.

The image on the right shows a flame that was on occasion produced upon ignition of the Al 10-14 μm powder. The flame is produced by the simultaneous burning of particles within the cloud. Quite a few streaks can also be seen leaving the flame region. To avoid formation of aerosol flames, as shown in this image, the spark voltage used in ignition experiments was limited to 8 kV.

In all images shown in Figure 4.4, particles are observed to travel away from the spark region. As discussed in the literature [34], such particle motion is most likely associated with a shock wave produced by the spark and reflected by the surface of the sample holder. An image shown in Figure 4.5 is produced using a modulated laser sheet placed perpendicular to the powder surface enabling visualization of particles lifted by the spark even when such particles are not incandescent. Brightly lit and saturated portions of the image are produced by the laser light scattered from the pin electrode, electrode holder, and the powder sample holder. Of interest are the particle streaks visible in the central part of the image. The cold lifted particles scatter the laser light and produce green, dashed streaks. Only particles moving within the laser sheet are so visualized. Considering the modulation frequency of 1000 Hz and the lengths of the observed dashed streaks, the velocities of the lifted particles in vicinity of the spark are close to 0.5 m/s. The streaks of laser-illuminated, cold particles are curved down

smoothly, showing characteristic trajectories of particles freely moving in the gravity field. On the other hand, ignited particles produce continuously bright streaks, which are also different in color from the scattered light streaks. The streaks of burning particles also show abrupt changes in the particle direction, most likely caused by sudden ejections of gas or particle micro-explosions. Both types of streaks are well visible in Figure 4.5. One important conclusion suggested by such images as shown in Figure 4.5 is that only a small fraction of particles ignite among a large number of particles lifted by the spark from the Al powder sample. Therefore, the mechanisms of particle ejection and ignition by the spark discharge are not directly related to each other.

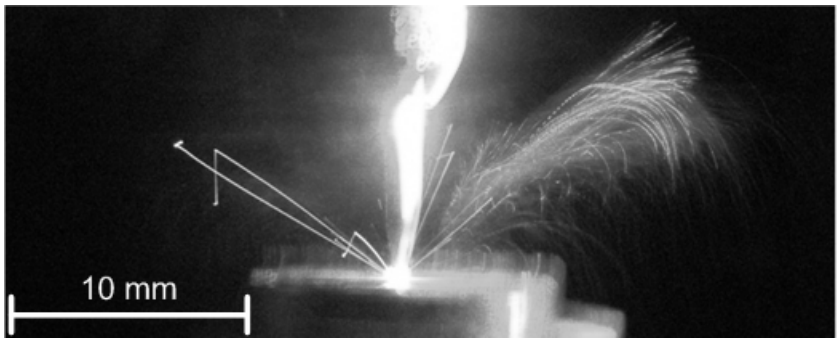

Figure 4.5 Image of burning particles showing both ignited and un-ignited particles illuminated by a modulated laser sheet.

4.1.3 Photodiode Traces

Figure 4.6 shows examples of photodiode traces and corresponding images of streaks produced by incandescent particles. As the spark energy decreases, the intensity, length, and number of the streaks decrease as well. At 5 kV the streaks are barely visible and below 5 kV the streaks are difficult to resolve. The corresponding photodiode traces are shown on the left. The photodiode signal is affected by both emission of the actual spark pulse and by the emission of the heated and ignited particles. The spark duration is

typically less than 1 μs, while the emission of the heated and ignited particles lasts much longer, up to several ms. In these experiments, in order to capture relatively dim streaks

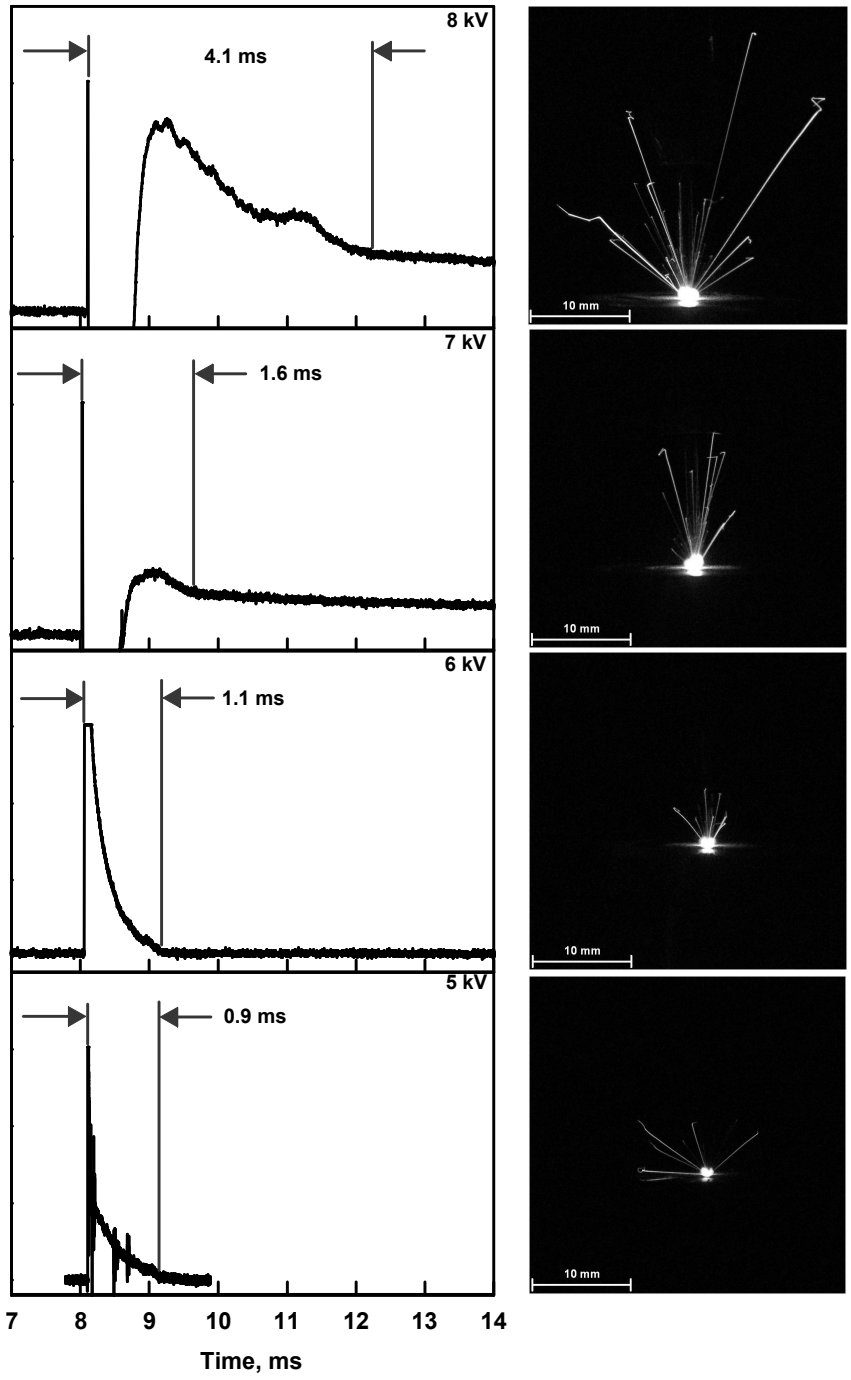

Figure 4.6 Photodiode traces and corresponding still images produced by particles ignited by sparks initiated with the capacitor charged to 8, 7, 6, and 5 kV (top to bottom).

produced by fine igniting particles, the photodiode was placed very close to the spark gap. An additional and undesirable result was that the photodiode output was often influenced by the electromagnetic field generated by the spark, so that the measured signal was saturated to either positive or negative level immediately following the spark. The data acquisition system could remain overwhelmed by the spark's interference for up to 500 μs, for the greatest used spark energies. After that time, meaningful optical emission traces were recorded. As shown in Figure 4.6, the photodiode signals exhibit one or more peaks with durations substantially greater than the spark duration. Amplitude, duration, and number of the peaks typically decrease with decreasing spark energy. Accordingly, the number and lengths of the streaks registered in the photographs acquired simultaneously to measuring optical signatures (cf. Figure 4.6) were decreasing at reduced spark energies. It is interesting that with the current experimental setup, the streaks could be photographed even for the spark energies reduced below the level needed to detect measurable photodiode traces. Thus, the significance of the MIE determined based on the visual detection of the igniting particles is questioned. Depending on the sensitivity of an optical sensor used, the MIE can vary widely even for the same powder ignited by the same ESD apparatus. In addition the MIE of Al dust explosions can vary considerably, ranging from 1-600 mJ, from which there can be significant variability even within the same experimental technique used [43–48].

To interpret the measured photodiode traces, note that the peaks observed represent the combined emission of all ignited particles. Assuming that all particles ignite within a relatively narrow time interval, during the spark discharge, it is possible to neglect the small difference in their ignition delays compared to the relatively long burn

times. Further, it is reasonable to suggest that the duration of the measured photodiode pulse is controlled by the longest particle burn time, corresponding to the ignited particle of the greatest size. Therefore, it is of interest to systematically measure the duration of the recorded photodiode pulses as a function of the applied spark energy (or voltage), to assess the burn times and estimate respective dimensions of the largest ignited particles.

Prior to discussing these measurements, it is noted that the measured durations of the recorded photodiode signals and lengths of the photographed streaks can serve as convenient and useful practical indicators of the powder ignition sensitivity. These parameters can be measured for a specified ESD energy or energy range and can characterize both temporal and spatial effects produced by the igniting powder. The smaller are the measured times and distances, the less likely the igniting particles are to present a fire hazard.

4.1.4 Burn Time as a Function of Joule Heat Energy

The particle burn time was taken to be the difference between the instant the spark strikes the powder and the time when the measured particle emission signal decreases to the background level. It was assumed that all particles start burning at the same instant, immediately after the spark. The measured burn times as a function of the Joule heat energy are shown in Figures 4.7 and 4.8 for Al 3-4.5 μm and Al 10-14 μm, respectively. A linear trend line is also included for each case. There is much more scatter in the data for Al 3-4.5 μm than for Al 10-14 μm. For Al 10-14 μm the trend shows that longer burn times are observed for greater Joule heat energies. There is a qualitatively similar, but very weak correlation between the burn time and Joule heat energy for Al 3-4.5 μm.

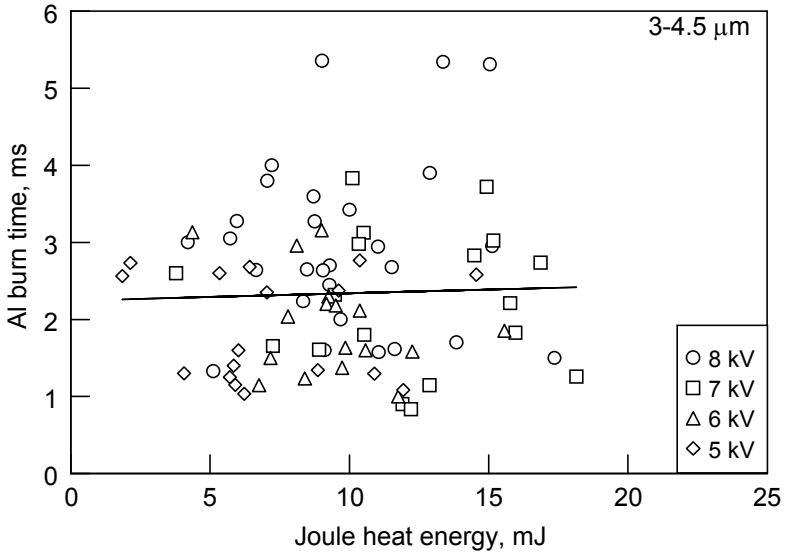

Figure 4.7 Particle burn time as a function of the Joule heat energy for Al 3-4.5 μm.

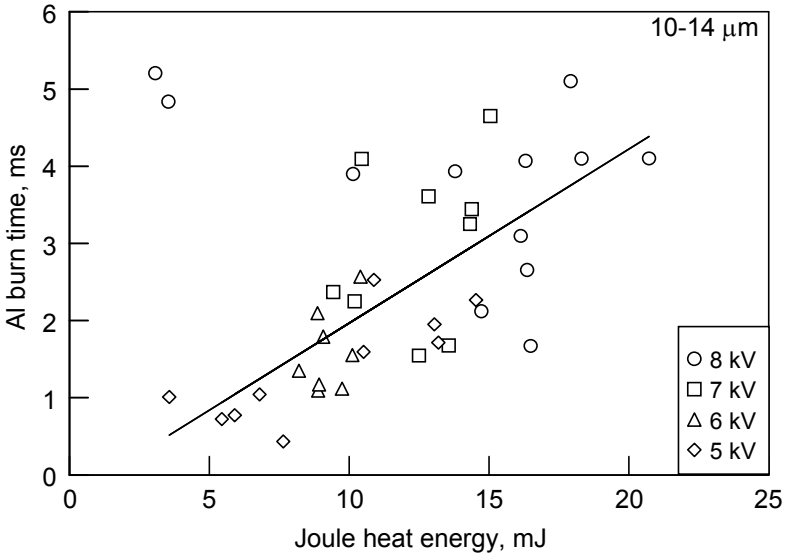

Figure 4.8 Particle burn time as a function of the Joule heat energy for Al 10-14 μm.

4.2 Interpretation of Aluminum Experimental Results

4.2.1 Largest Particle Ignited by Spark

The particle diameters are estimated using reported relationships between burn times and diameters for aluminum. Among several expressions reported in the literature, two trends proposed recently for micron-sized particles [49, 50] were selected. A linear relation was proposed based on aerosol flame measurements in Reference [49]:

$$\tau = 310d \tag{4.1}$$

where τ is the particle burn time in μs and d the particle diameter in μm. Experiments with aluminum particles ignited in a heterogeneous shock tube [50] were used to derive a different relation between the particle burn time and its diameter, where effects of the ambient pressure, P, and mole fraction of oxidizer, X_{OX}, are also incorporated:

$$\begin{aligned} \tau &= 200 X_{OX}^{0.5} \left(\frac{P}{P_0} \right)^{-0.5} d^n \\ n &= 2 \exp\left(-4.3 X_{OX}\right) \left(\frac{P}{P_0} \right)^{-0.3} \end{aligned} \tag{4.2}$$

where d is in μm, $X_{OX} = 0.21$ for air, and $P_0 = 8.5$ atm.

A plot recalculating measured burn times into expected particle diameters using data shown in Figure 4.8 is presented in Figure 4.9. Diameters based on Equation (4.2) are somewhat smaller than predicted by Equation (4.1), with the difference increasing at greater Joule energies. Note that similar processing for the results shown in Figure 4.7 for the 3-4.5 μm powder was also performed, but is not shown for brevity, and because of a strong scatter in the measured burn times making it difficult to interpret the measurements.

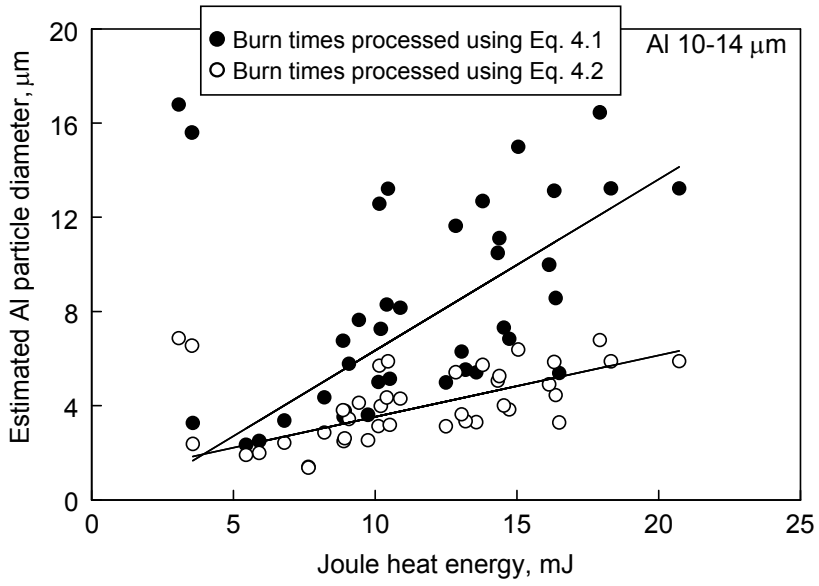

Figure 4.9 Estimated particle diameters based on expressions Equation 4.1 and Equation 4.2 as a function of the Joule heat energy for Al 10-14 μm (from data shown in Figure 4.8).

4.2.2 Particle Diameter Estimated Based on the Measured Burn Time

As in the previous work with Mg ignition, it is assumed that the spark discharge adiabatically heats the powder in a cylindrical volume, within which the spark current flows [51]. However, previously, a simplified assumption of the uniformly sized powder particles was used. Here, this approach is modified to account for different heating of particles of different sizes present within the volume directly heated by the spark, as illustrated in Figure 4.10. The spark energy is divided between powder size bins, obtained from the particle size distribution measurements. The particles are assumed to be heated from the hot spots formed at the particle-particle contact points. At such points, the local resistance is high and respectively, the heat release due to Joule heating is strongest. For a polydisperse powder, the number of such hot spots per particle is proportional to the particle surface area. Therefore, for an estimate, the fraction of the

spark energy supplied to each size bin is taken to be proportional to the respective bin's surface area.

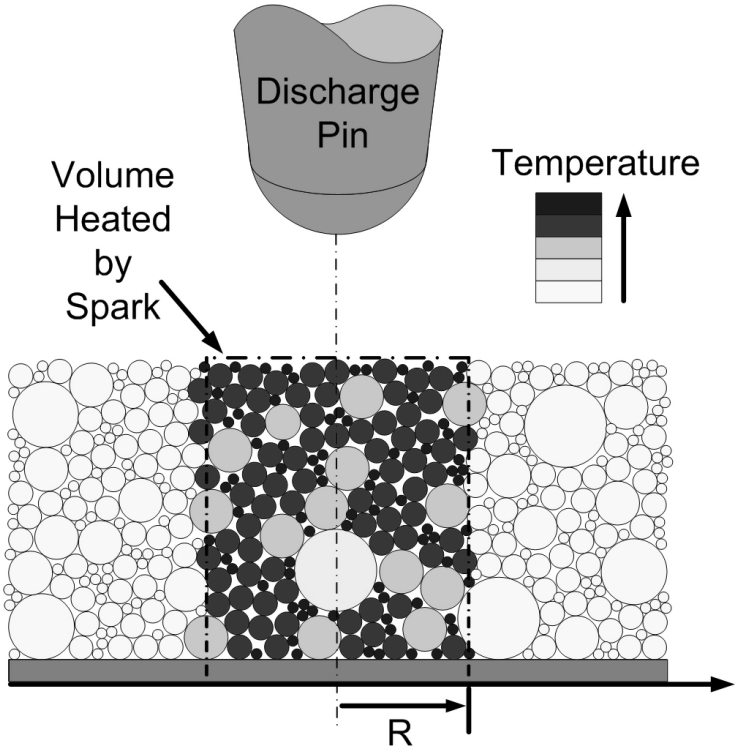

Figure 4.10 Schematic diagram of the model accounting for the powder Joule heating within a cylinder limited by the equivalent spark radius, *R*. The spark energy is distributed proportionally to the particle surface areas.

Within each size bin, all particles are heated uniformly so that the energy per particle is computed as the fraction of the energy supplied to the entire bin divided by the number of particles in the bin. Following this approach, the temperature of a particle is calculated by:

$$T = T_m + \frac{6E_{D,i}}{\rho D_i^3 C_{PL}} - \frac{C_{PS}}{C_{PL}}\left(T_m - T_0\right) - \frac{L}{C_{PL}} \tag{4.3}$$

where T_0 is the initial powder temperature assumed to be equal to the room temperature, 300 K, T_m = 933 K is the aluminum melting temperature, C_{PS} = 977 J/kg K and C_{PL} = 1096 J/kg K are the values of specific heat for solid and liquid aluminum, respectively, L

= 398 kJ/kg, is the latent heat of melting for aluminum, ρ = 2700 kg/m^3 is the density of aluminum, and D_i is the particle size of a bin from the particle size distribution. $E_{D,,i}$ is the portion of the Joule heating energy per particle, given by:

$$E_{D,i} = \frac{E_i}{n_{D,i}} \tag{4.4}$$

where E_i is the total energy delivered to all the particles of a given size bin and $n_{D,i}$ is the total number of particles in this bin. The total number of particles in a size bin is given by:

$$n_{D,i} = \frac{6\eta m_{D,i} R^2 H}{D_i^3} \tag{4.5}$$

where η = 0.5 is the packing density for loosely packed spherical particles, $m_{D,i}$ is the relative mass fraction of a size bin, R is the equivalent spark radius (measured as discussed above), and H is the height of cylindrical volume directly heated by the spark (in these experiments, it was equal to the thickness of the powder layer in the sample holder, approximately 0.5 mm). The equivalent spark radius varied as a function of the spark voltage setting (see trend-line in Figure 4.3). The total energy delivered to all the particles of a size bin is proportional to its total surface area:

$$E_i = J_j \times \frac{n_{D,i} D_i^2}{\sum n_{D,i} D_i^2} \tag{4.6}$$

where J_j is the Joule heat energy recovered from the spark current and powder resistance, and j is the level of the spark energy chosen for the estimate.

For a simplified data processing, three levels of the experimental Joule heating energies were chosen (see Table 4.1) corresponding respectively to the minimum, median, and maximum energies (j=1, 2 or 3) from the data shown in Figures 4.7 and 4.8.

For each energy level, and taking into account respective equivalent spark radius (cf. Figure 4.3 and Table 4.1), temperatures achieved by particles of different sizes were calculated. These temperatures are shown as solid lines in Figure 4.11. Note that data and processing discussed here are for the coarser, and less agglomerated Al 10-14 μm powder. Similar processing was also done for the data shown in Figure 4.7 for the 3-4.5 μm powder; however because of substantial scatter in the experimental data these results are omitted.

Table 4.1 Energy Levels used in Equation (4.3) and Corresponding Equivalent Spark Spot Radii

Energy level, j	Joule energy, mJ	Spark radius, μm
Minimum	3.6	60
Median	12.5	78
Maximum	20.7	95

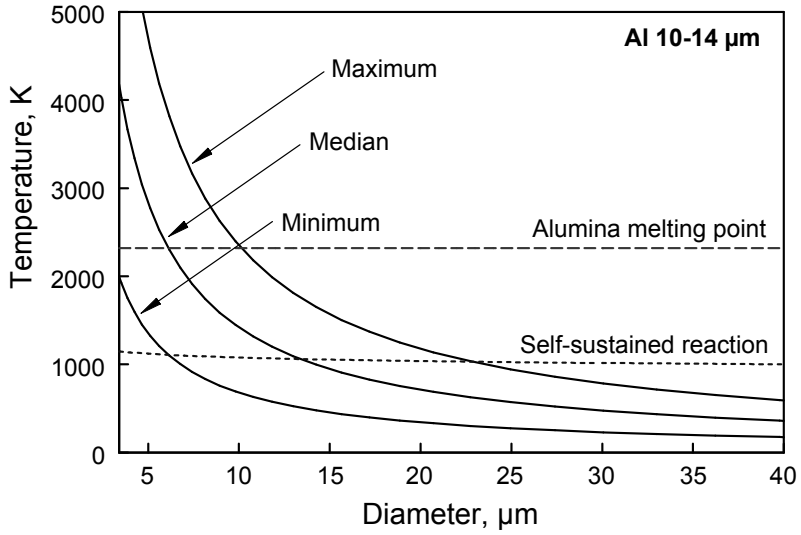

Figure 4.11 Solid lines show temperatures of particles heated by the spark as a function of their diameter based on Equation 4.3 for Al 10-14 μm for three spark energy levels. Dashed lines show temperatures for which ignition criteria are satisfied (see text).

The estimated particle temperatures shown in Figure 4.11 are higher than those expected in experiments because heat losses were neglected. The effect of heat losses is particularly important for finer particles, for which very high temperatures are predicted.

Two ignition criteria were considered. One criterion assumes that the particle ignites when it is heated to the alumina melting point, 2320 K, shown as a dashed horizontal line in Figure 4.11. A second criterion was considered based on the heat balance between the exothermic surface reaction and convective heat losses to surrounding cold air. The temperature, at which chemical heat generation surpasses heat losses, assumed to be the minimum ignition temperature. Using this second ignition criterion, the minimum ignition temperature can be determined from the following equation solved for T:

$$PZ\Delta H \exp\left(-\frac{E_A}{R_u T}\right) \geq \frac{Nu}{D} k\left(T - T_\infty\right) \tag{4.7}$$

where P = 21278 Pa is the partial pressure of O_2 in air, ΔH = 1675.7 kJ/mol is the enthalpy of oxidation, Nu is the Nusselt number, k is air thermal conductivity, and T_∞ is the surrounding gas temperature and the Arrhenius type term taken from Reference [52]: activation energy E_A = 179 kJ/mol and pre-exponent Z = 5630 s/m. The respective dashed curve is labeled by "self sustaining reaction" in Figure 4.11.

The curves showing the temperatures to which particles of different sizes are heated by the spark cross both the horizontal temperature level corresponding to melting of alumina, and the line showing a minimum ignition temperature obtained from Equation (4.7). It is immediately noted that the particle sizes predicted to ignite using the criterion determined by Equation (4.7) are unreasonably large. This could be due to an inaccurate description of the oxygen concentration and temperature of the surrounding

gas in the post spark heating environment, which are not accounted for by used Arrhenius kinetics parameters obtained for Al ignition in cold air. In addition, for small particles approaching one micron and below in size, the Knudsen number increases so that the convective environment can no longer be described by a continuum model (effective Nu number becomes less than 2).

Figure 4.12 shows plots of particle diameters obtained from the experimental burn times and Equations (4.1) and (4.2) for Al 10-14 μm compared to the particle diameters for which the temperatures given by Equation 4.3 are equal to the alumina melting point for different Joule heat energies. It appears that the prediction by Equation (4.2) matches quite well the diameters of particles heated to the alumina melting point. The experimental diameters expected based on the Equation (4.1) are over-predicted for the greater spark energies. As noted above, the temperatures to which the particles are heated are over-predicted because of neglected heat losses. Accounting for the heat losses would shift the curve with open symbols in Figure 4.12 down, which would further improve the match with the predictions by Equation (4.2). Equation (4.1) is not matched as well, which could be explained because it was derived for a burning aerosol, not a single particle. In aerosol, the particles compete for the oxidizer, so that the overall burn time becomes longer.

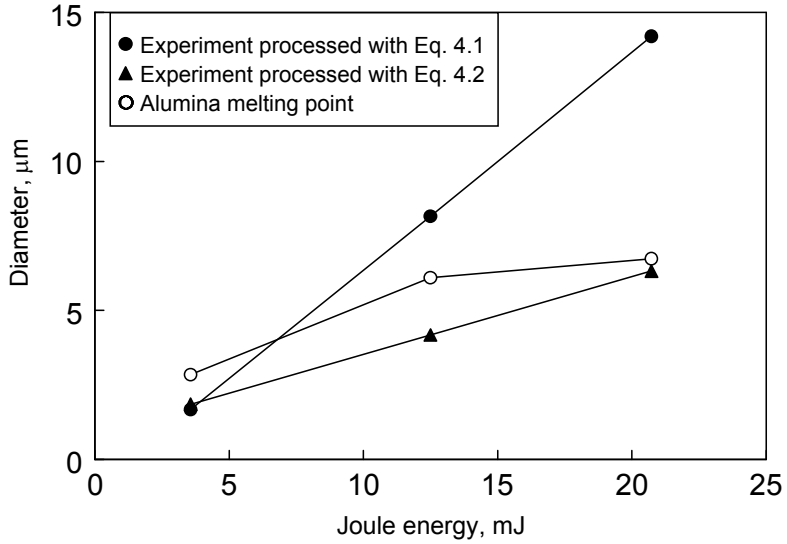

Figure 4.12 Filled symbols show diameters of the largest ignited particles obtained from experimental burn times and correlations (Equation 4.1) and (Equation 4.2). Open symbols show particle diameters predicted to be heated to the alumina melting point for different Joule heat energies. All processing is based on results for Al 10-14 μm powder.

CHAPTER 5

ESD STIMULATED IGNITION OF TITANIUM POWDER

5.1 Results of Titanium Experiments

5.1.1 ESD Effect on Powder Morphology

Titanium powders placed in a sample cup (except for the monolayer samples) struck by the spark remained mostly undisturbed. This was markedly different from Al and Mg powders, for which the spark was earlier reported to form an empty crater, whether the powder was or was not ignited [51, 53]. Inspection of Ti powder samples struck by the spark indicated that large particle agglomerates formed in the sample directly under the pin electrode. The agglomerates could be extracted from the powder with tweezers; they could also be retained on surface of the sample cup after pouring off the surrounding un-agglomerated powder. To examine agglomerates better, powder samples were prepared and struck by the spark in several locations; the unagglomerated powder was then removed and agglomerates adhering to the substrate were examined under a microscope. Four such agglomerates are shown in Figure 5.1. The size of each agglomerate is close to 1 mm. The particles are fused together to form nearly cylindrical volumes that are weakly bonded to the brass support. The fused particles were inspected under SEM, which showed that the particles formed chain-like structures, as shown in Figure 5.2. Such chain-like structures were most noticeable for thicker powder layers, in which they grew from three-dimensional agglomerates observed at the sample surface. The particle chains penetrated through the powder to the sample holder surface. Upon closer inspection of the particle surfaces and interfaces between the fused particles, it was

observed that the particle shapes were generally preserved, indicating that it is unlikely that particles were fully molten. An additional substance fusing particles together is observed, as shown in Figures 5.3 and 5.4 for spherical and sponge powders, respectively. For the sponge powder, the distance between the fused particles could be greater than for spherical powder; however, the fused areas were generally smaller. Energy-dispersive spectroscopy did not identify any difference in the elemental compositions between undisturbed particle surfaces and their fused interface regions. To examine the effect of possible oxidation or nitridation on particle agglomeration, additional experiments were performed with the entire ESD sample holder and electrodes assembly placed in a sealed chamber filled with argon. The agglomerates were observed to form exactly as in air, suggesting that the substance bonding particles to one another is generated from the heated particles themselves, with no apparent effect of the surrounding gas environment.

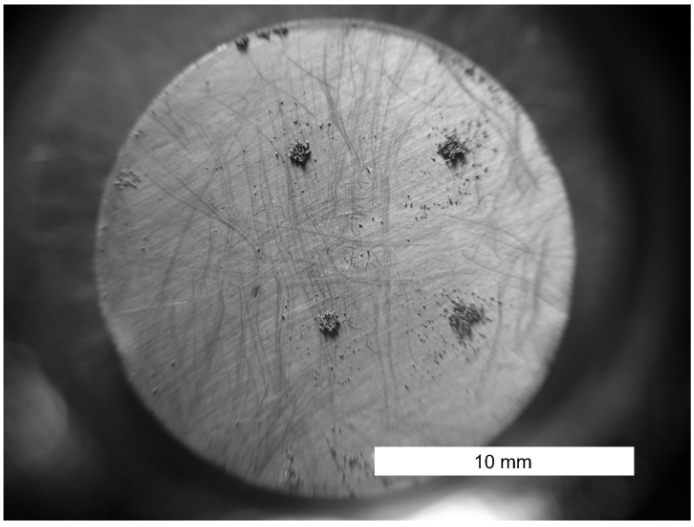

Figure 5.1 Optical microscope image of fused spherical Ti particles formed in a 0.5-mm thick sample placed in a brass sample cup.

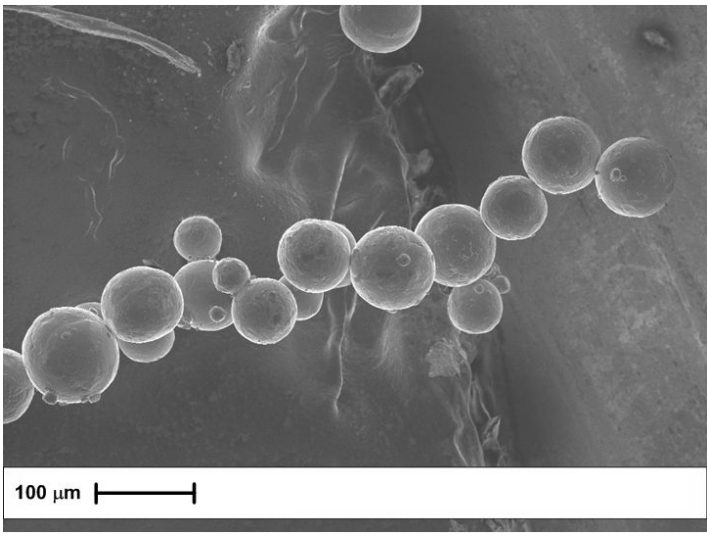

Figure 5.2 SEM image of spherical Ti particles fused together into a chain. Such chains penetrated from the top to the bottom of the fused agglomerate.

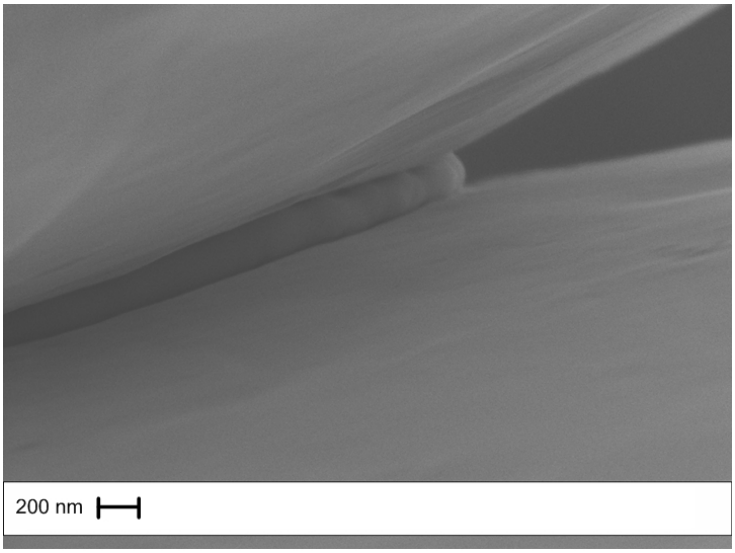

Figure 5.3 SEM image showing a close up view of two spherical particles fused together.

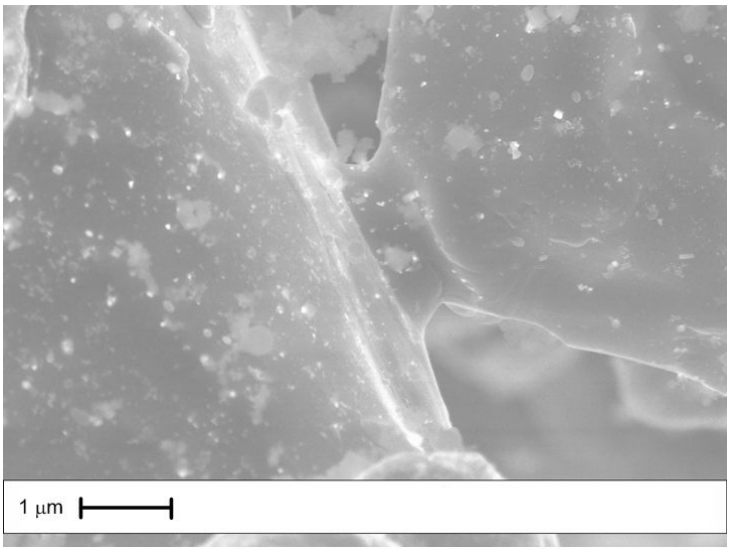

Figure 5.4 SEM image showing a close up view of two "sponge" particles fused together.

Effect of ESD on monolayers of Ti powders was markedly different compared to thicker powder samples. Instead of agglomerating, a fraction of the powder directly under the pin electrode was removed from the sample holder after the spark. Images of the sample holders coated with carbon tape, containing Ti powder monolayers after being struck by the spark are shown in Figure 5.5. As further discussed below, the powder

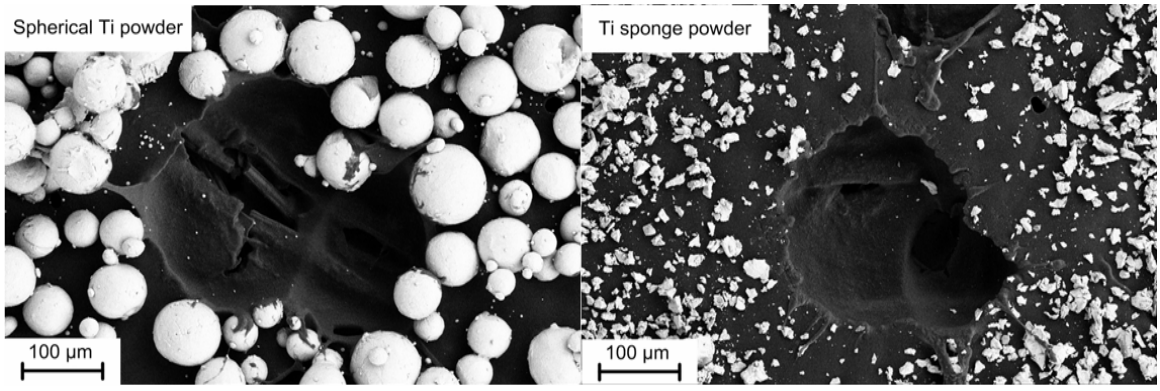

Figure 5.5 SEM images of Ti spherical and sponge powders placed in monolayers and struck by the spark. The center of each image shows a region where the powder was removed by the spark.

removed from the monolayer sample always ignited. Some of the spherical particles surrounding the area struck by the spark in Figure 5.5 appear to be fractured. As will be discussed later, indeed, most of the particles placed as a monolayer and directly affected by ESD are fractured producing very fine burning metal droplets.

5.1.2 Spark Radius Measurements

To describe the energy transfer from ESD to powder, a quantitative assessment of the powder surface directly struck by the spark or spark radius is desired. Separate measurements of spark radii were performed for samples placed in monolayers on carbon tape and for thicker samples.

For powder monolayers, the area of the spark imprint left on the carbon tape was assumed to represent the powder area directly heated by the spark. ESD with different energies were produced using different starting voltages. The sparks were produced between the pin electrode and a blank carbon tape. The imprint left by the discharge on the tape was examined using an SEM and the results are shown in Figure 5.6. The spark radius is approximated by one half of the Feret diameter calculated from the area of the detectable spark imprint. Similar to data presented in Chapter 4 in which spark radius was determined from the size of the spark imprint left on a carbon-coated metal plate, the radius measured here was increasing at higher voltages.

For thicker powder samples, the spark radius was measured collecting and examining particle agglomerates, assumed to be formed by the passing electric current. The radii of the agglomerated powder cylinders were anticipated to be equal to the respective spark radii. The experiments were performed with both spherical and sponge powders.

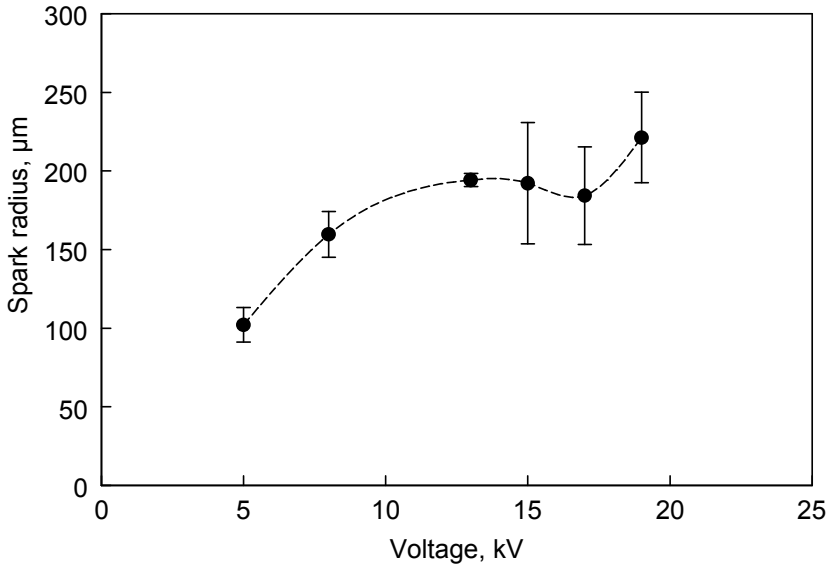

Figure 5.6 Spark radius as a function of capacitor voltage for powder monolayer obtained from the spark imprint areas on a blank carbon tape.

The size of agglomerates as a function of the sample layer thickness was determined for the spark voltage set at 13 kV. These results are shown in Figure 5.7. The filled and open circles show the radii obtained as dimensions of the agglomerated powder cylinders, for spherical and sponge Ti powders, respectively. The square symbols are the spark imprint radii obtained with monolayer samples (cf. Figure 5.6), shown for comparison. For both spherical and sponge powders, the spark radius implied from Figure 5.7 is increasing at the increasing sample thickness; the spark radii measured for monolayers appear to fit well with trends observed for thicker powder samples. It is interesting that the radii of agglomerates for sponge powder are consistently greater than those observed for spherical powder.

The size of agglomerates as a function of the applied spark voltage (or the capacitor voltage prior to spark initiation) was measured for a constant layer thickness of 0.5 mm. Results are shown in Figure 5.8. The spark radius for the multilayered powder

samples inferred from this measurement appears to be a weak function of the voltage, increasing only slightly over a relatively broad range of voltages considered.

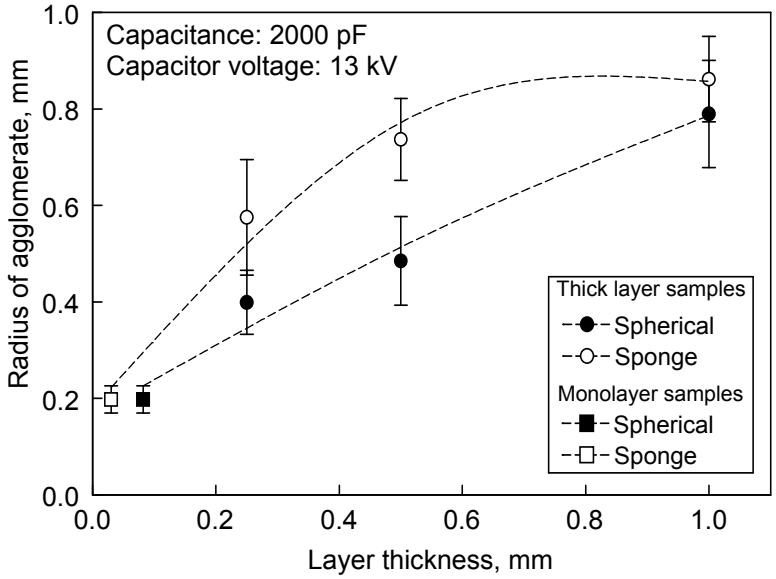

Figure 5.7 Agglomerate radius of fused Ti particles as a function of powder layer thickness for spherical and sponge powders at a capacitance of 2000 pF and a capacitor voltage of 13 kV.

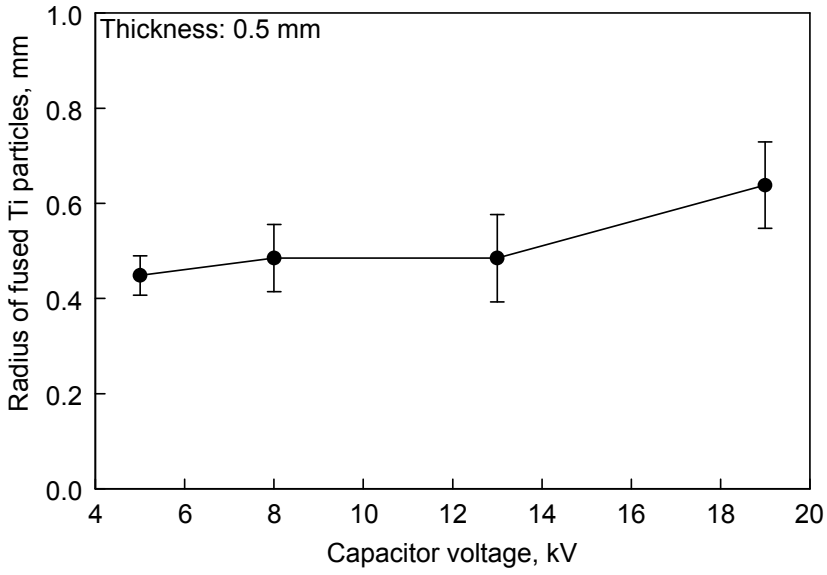

Figure 5.8 Agglomerate radius of fused Ti particles as a function of the capacitor voltage for the spherical powder placed in a 0.5-mm thick layer.

5.1.3 Electrical Characteristics of Spark and Powder Layers

Measurements of ESD current and voltage as a function of time were used to determine phase shift between the current and voltage, the resistance of the powder layer, energy dissipated in the discharge, and energy transferred to the powder as a result of its Joule heating. Characteristic examples of the measured current and voltage traces are shown in Figures 5.9 and 5.10 for two powder samples with different thicknesses. In both cases, the current and voltage amplitudes decay in time, as reported earlier for similar experiments with Mg powders [51]. There is a marked difference between the sets of traces shown in Figures 5.9 and 5.10: for the sample prepared as a monolayer (Figure 5.9), the phase shift between current and voltage is relatively small, indicating a mostly active electric load for the spark; however, for the thicker layer, the voltage lags behind current noticeably, suggesting a capacitive impedance. A more systematic analysis of the phase shift between the spark current and voltage for different experimental configurations is presented in Table 5.1. For spherical Ti monolayers, the phase shift appears to remain close to zero for a range of ESD voltages. For thicker layers of spherical Ti powders, the phase shift is consistently in the range of about 50-90º irrespective of the voltage or layer thickness. There is no clear correlation between the phase shift and powder layer thickness for multilayered samples of the sponge powder, for which the phase shift increases at lower capacitor voltages. For monolayers of the Ti sponge powder, the phase shift does not appear to be a function of the capacitor voltage.

As in the previous work [51, 53], the measured ESD current traces were curve-fitted using an expression for a decaying current for an L-R-C circuit connected in series [35], treating the L, R, and C values as adjustable parameters. The measurements and

data processing were performed for both empty sample holder and sample holder filled with the powder. In both cases, the value of C was usually very close to that of the capacitor used. The powder resistance, R_p, was determined as a difference between resistances found in experiments with filled and empty sample holders. The value of R_p was used to quantify the Joule heating of the powder by the spark current. The powder resistance for different layer thicknesses and voltages is presented in Table 5.1 and Figure 5.11. For voltages of 13 kV and above, changes in the resistance are small. Below 13 kV, the resistance increases with decreasing voltage. It is interesting that the resistance does not appear to be a function of the powder layer thickness. It also appears to be similar for spherical and sponge powders. The energy transferred to the sample as a result of its Joule heating was determined by Equation (3.3). In addition, the total ESD energy dissipated in the discharge was calculated as:

$$E_{total} = \int_0^{\tau} I(t)V(t)\cos\left[\varphi(t)\right]dt \tag{5.1}$$

where $V(t)$ is the voltage measured as a function of time τ, $I(t)$ is the measured current as a function of time, τ is the ESD pulse duration, and φ is the phase shift between current and voltage.

A correlation between the two values of energy is shown in Figures 5.12. The individual points are widely scattered. Most of the data scatter is explained by a significant error involved with interpretation of relatively noisy voltage traces. At low capacitor voltages, the total dissipated energy is relatively close to the Joule heating energy; however, the discrepancy between the two quantities grows as the ESD voltage

increases, indicating an increased dissipation of the spark energy by radiation and heating the spark plasma in addition to the Joule heating energy, mostly dissipated in the powder.

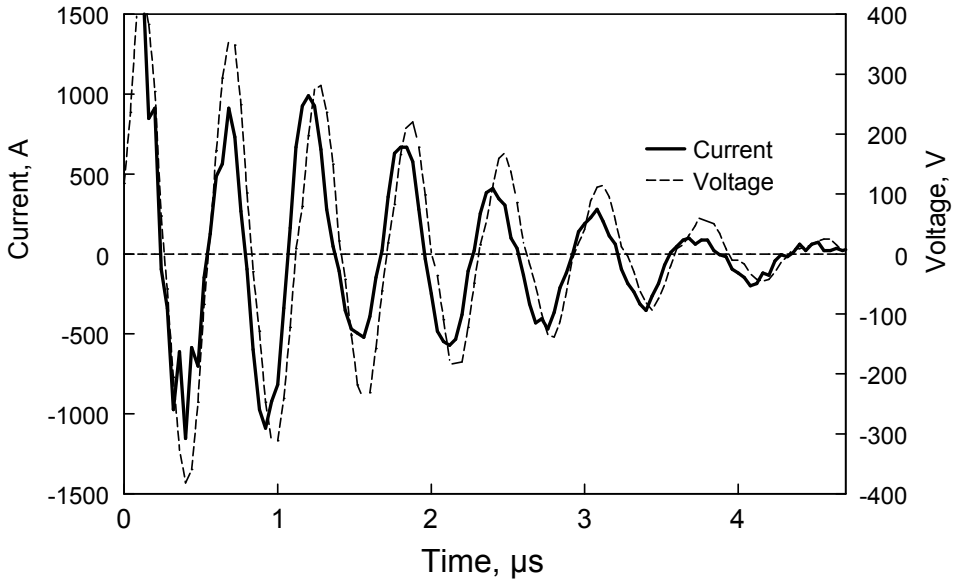

Figure 5.9 Example of current and voltage signals acquired for a monolayer sample of spherical Ti powder.

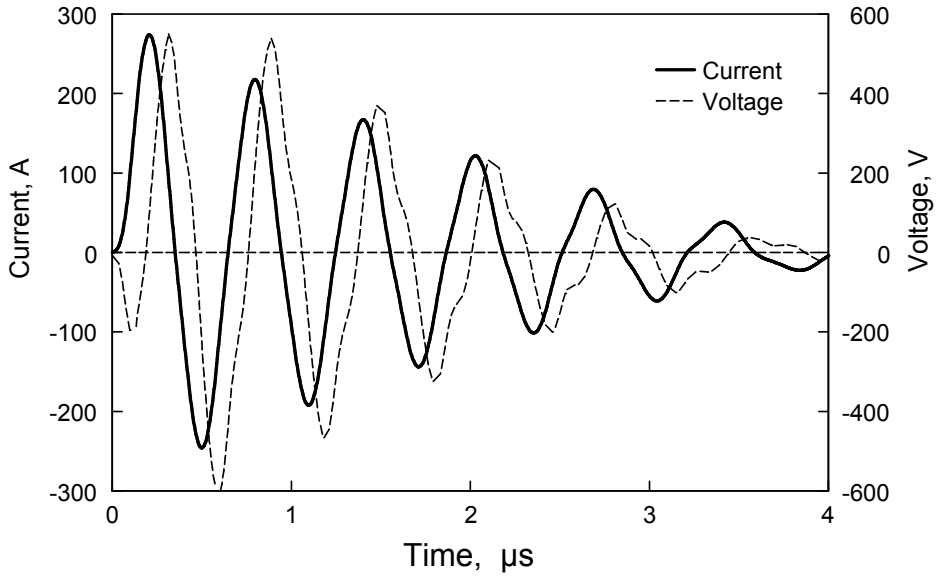

Figure 5.10 Example of current and voltage signals acquired for a 0.5 mm powder layer sample of spherical Ti powder.

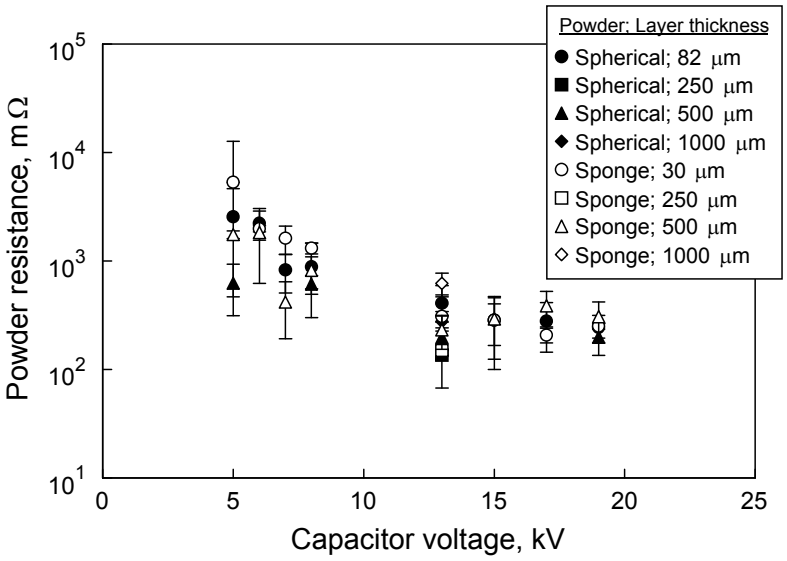

Figure 5.11 Resistance as a function of capacitor voltage for both spherical and sponge powders for different powder layer thicknesses.

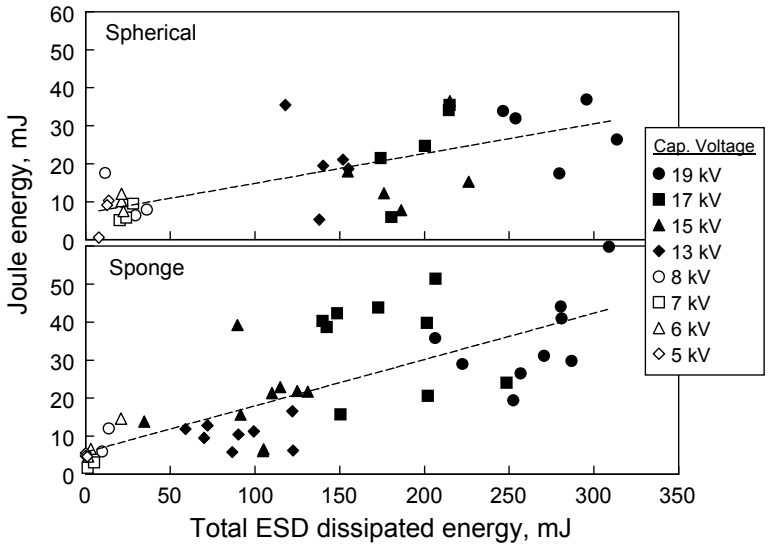

Figure 5.12 Correlation between calculated Joule energy and total ESD-dissipated energy for sponge and spherical powders. The experimental points are collected for samples prepared as 0.5-mm thick powder layers. Different symbols represent different capacitor voltages.

Table 5.1 Phase Shift Between Current and Voltage and Powder Resistance for Sparks Striking Ti Powders for Different Capacitor Voltages and Powder Layer Thicknesses

Material / holder	Thickness, μm	Capacitor Voltage, kV	Phase shift, θ	Powder resistance, mΩ
Spherical Ti (monolayer)	82	19	-21 ± 4	250 ± 70
		17	-17 ±7	280 ± 140
		15	-10 ± 8	290 ± 190
		13	-4 ± 22	410 ± 180
		8	-9 ± 18	880 ± 580
		7	-16 ± 2	830 ± 320
		6	-6 ± 5	2200 ± 660
		5	-23 ± 15	2600 ± 2100
Ti sponge (monolayer)	30	19	-12 ± 57	250 ± 20
		17	48 ± 33	210 ± 30
		15	55 ± 36	280 ± 120
		13	64 ± 26	310 ± 30
		8	101 ± 2	1310 ± 150
		7	59 ± 25	1620 ± 480
		6	98 ±18	1990 ± 130
		5	108 ± 51	5320 ± 7380
Ti sponge (dedicated 0.5-mm deep sample cup)	500	19	-13 ± 9	310 ± 110
		17	-17 ± 11	390 ± 140
		15	-25 ± 18	290 ± 170
		13	-19 ± 9	230 ± 80
		8	26 ± 64	820 ± 270
		7	80 ± 9	420 ± 230
		6	76 ± 23	1800 ± 1200
		5	122 ± 11	1750 ± 140
Spherical Ti (PVC/brass sample cup)	1000	13	73 ± 10	280 ± 210
	500	13	73 ± 17	200 ± 40
	250	13	72 ± 0	135 ± 10
	500	19	43 ± 49	200 ± 60
		8	87 ± 34	610 ± 120
		5	69 ± 2	620 ± 310
Ti sponge (PVC/brass sample cup)	1000	13	67 ± 14	620 ± 150
	500	13	48 ± 66	420 ± 140
	250	13	74 ± 14	150 ± 150

5.1.4 Images and Photodiode Traces Produced by Igniting Powders

As in the previous work with Al [53], images and photodiode traces were acquired for ESD-ignited Ti particles. Figure 5.13 shows a set of photodiode traces and their corresponding images of ignited particles for the spherical powder. Calculated Joule energy dissipated in the sample is shown for each pair of trace and image. Based on the photodiode traces, ignition occurred instantly upon spark heating and corresponds to 0 ms on the photodiode traces. The trace and image in Figure 5.13 (top) shows burning Ti particles for a sample prepared as a 0.5-mm thick layer. A single streak is observed, which produces a barely distinguishable signature on the respective photodiode trace. The burn duration was 0.7 ms and multiple ignition experiments with the sample prepared at this thickness produced burn times no longer than 1 ms. In many of these experiments with ESD voltage set between 5 and 19 kV, no ignition was observed on either the photodiode or on the image. The trace and image in Figure 5.13 (middle) show signatures of ESD-ignited spherical Ti particles prepared as a monolayer. The spark energy is smaller than for the case shown in Figure 5.13 (top), however, more particle streaks are visible and streaks are longer compared to Figure 5.13 (top). Optical signatures obtained for a powder monolayer struck by a spark with a greater energy (obtained at an increased capacitor voltage) are shown in Figure 5.13 (bottom). There is a substantial increase in both number and length of the observed particle streaks.

ESD initiation of the sponge powder prepared as a 0.5-mm thick sample resulted in multiple and relatively long streaks of burning particles. Both the number of the particle streaks and their lengths were greater than that for the similarly prepared sample of the spherical powder. In fact, the streaks were also noticeably longer than that for the

spherical Ti powder prepared as a monolayer (as shown in Figure 5.13, bottom). Ignition signatures produced by the sponge powder prepared as a monolayer were qualitatively indistinguishable from those observed for the spherical powder.

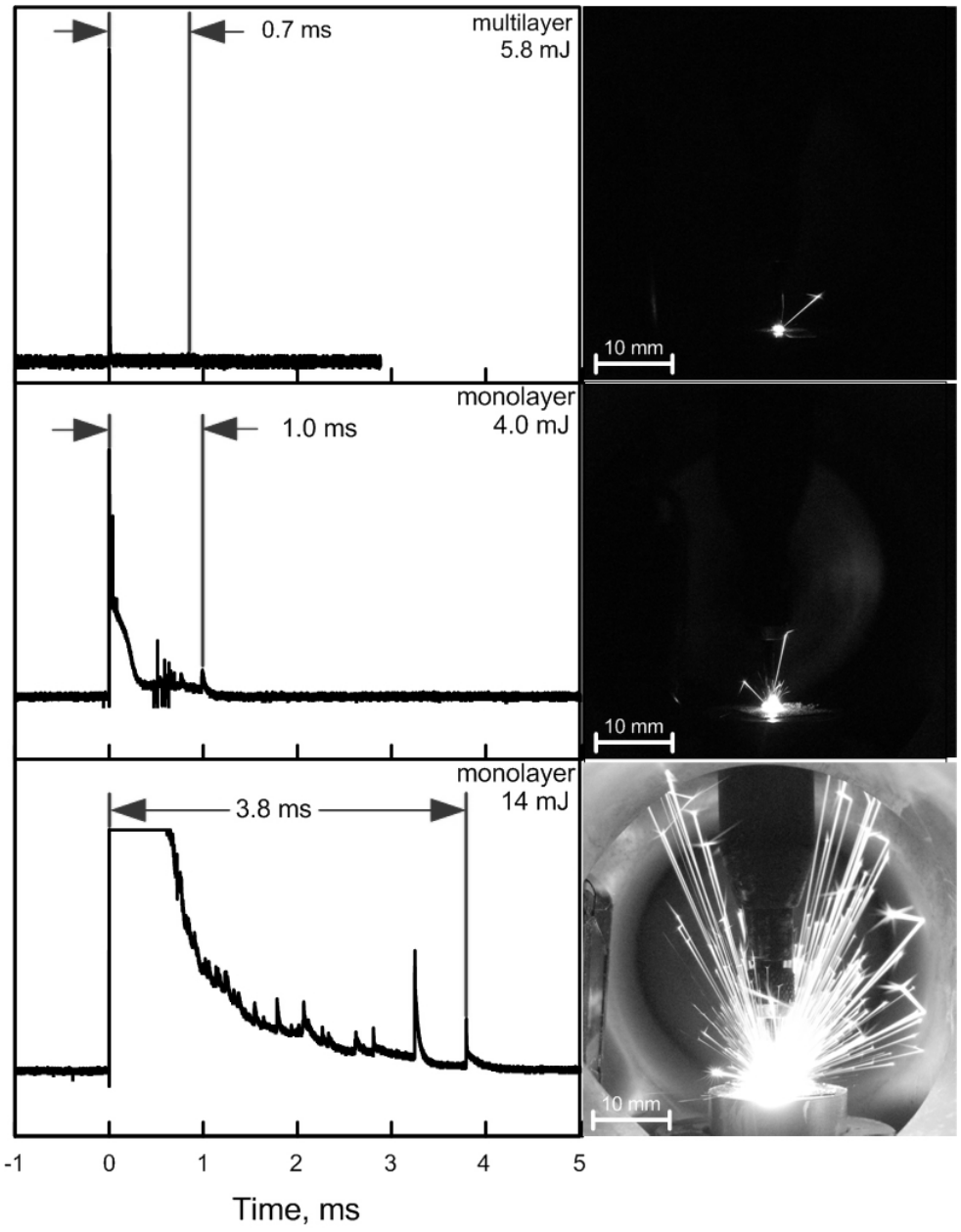

Figure 5.13 Photodiode traces and still images of spherical Ti powder prepared as a 0.5 mm thick sample (top), as a monolayer and low capacitor voltage (middle) and as a monolayer and high capacitor voltage (bottom). Labels show calculated Joule energies for each pair of trace and image.

The overall light intensities and particle burn times were evaluated for both spherical and sponge powders as shown in Figures 5.14 and 5.15 as a function of the total spark energy, E_{total}. The light intensity gives a qualitative indication of the size as well as number of the ignited particles. It was evaluated as the total pixel intensity for still images of burning particles (as shown in Figure 5.13) by Tracker 3.0 software [41]. The results are shown for monolayer samples for the spherical powder, for which thicker powder samples were difficult to ignite reproducibly. For Ti sponge powder, most of the shown results represent experiments with 0.5-mm thick samples, consistently with our earlier work for Mg and Al [51, 53],

Despite substantial scatter, it is observed that for spherical Ti powder the light intensity is a weak function of spark energy, it increases with increasing spark energy. For sponge powder, the light intensity is consistently low at low spark energies; the intensity is scattered in a broad range when the spark energy is increased.

The burn times are broadly scattered for both powders, and it is difficult to identify a trend for either case. The range of scatter generally expands at greater spark energies. It is striking that the burn times measured for the spherical powder (0.5-4 ms), are substantially shorter than those observed for a much finer sponge powder (up to 35 ms.)

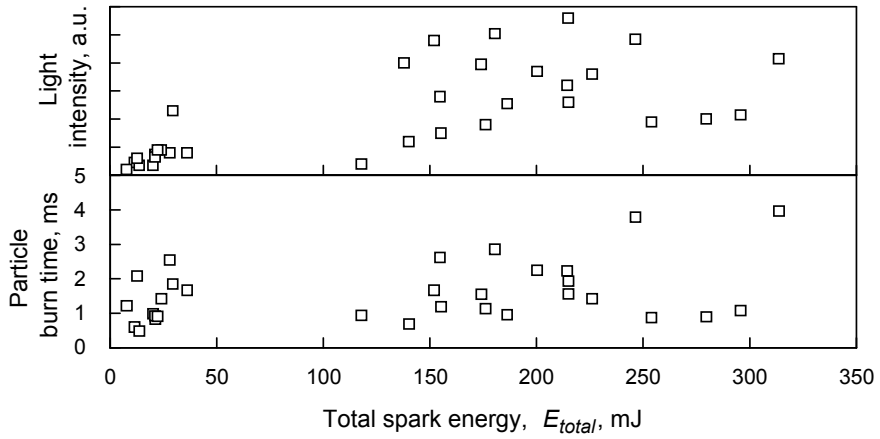

Figure 5.14 Light intensity and particle burn times as a function of the total spark energy for the spherical Ti powder prepared as a monolayer.

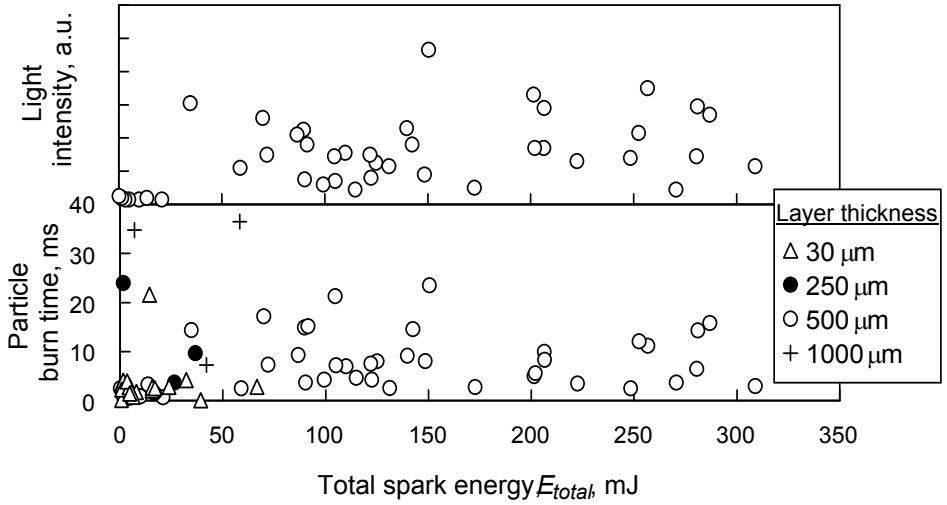

Figure 5.15 Light intensity and particle burn times as a function of the total spark energy for the sponge Ti powder. In addition to the results for the 0.5-mm thick layer, data for other layer thicknesses are also presented.

5.1.5 Captured Particles Lifted from the Sample Holder

The apparent discrepancy between relatively large particle dimensions and very short burn times observed for the spherical powder suggested a possibility that the particles are disintegrated so that combustion of smaller particle fragments is observed. To investigate this possibility, capture of ignited particles was attempted. In separate experiments, a cleaned Si wafer and double sided carbon tape were placed above the ESD initiated

powder sample. However, burning particles did not adhere to the capturing surfaces. Additional experiments were carried out in an Ar environment. The imprint left on a monolayer sample struck by a spark was similar to that observed in air, indicating that approximately the same amount of powder was removed from the substrate. The particles removed from the substrate were captured on a Si wafer placed 3-4 mm away from the substrate surface. Figure 5.16 shows an SEM image of such captured particles on the Si wafer. A higher magnification image of one such particle is shown in Figure 5.17. The particles are clearly formed upon splat quenching of fine metal droplets flying towards the Si wafer at an appreciable velocity. The sizes of the particles found on the Si wafer are much smaller than the parent particles, confirming the fragmentation of the initial powder by the spark.

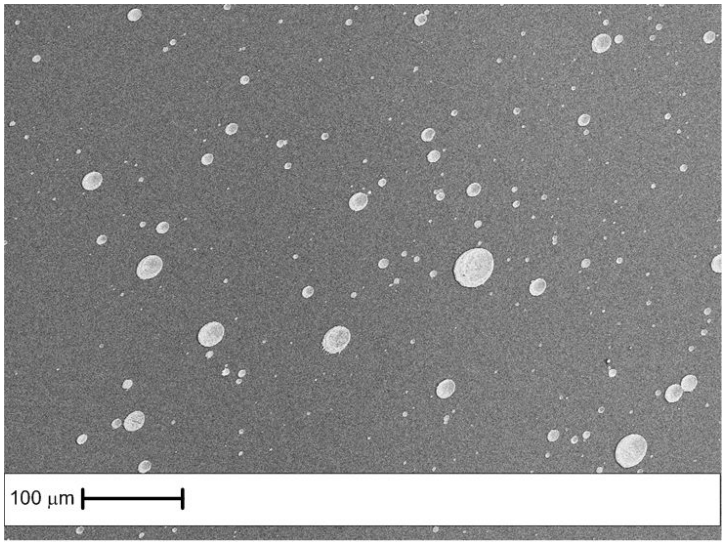

Figure 5.16 SEM image of molten Ti droplets splattered across a Si wafer.

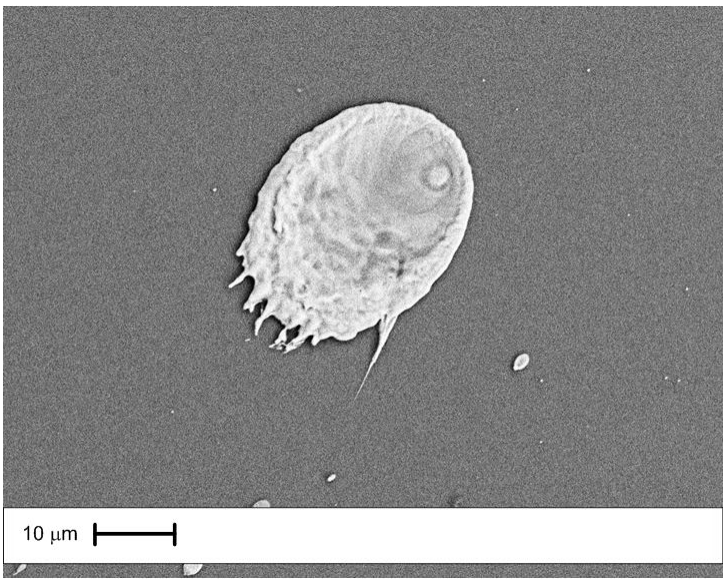

Figure 5.17 SEM image of a close-up of a molten Ti droplet.

5.1.6 Heated Filament Ignition Experiments

These experiments were aimed to characterize thermal initiation of titanium powder. Experiments were performed with the Ti sponge powder; details of the experimental methodology and processing are available in Reference [29]. The powder was coated on a nickel-chromium alloy filament which was electrically heated. The ignition moment, as well as the ignition temperature, were determined optically. The heating rates varied in the range of 450-35000 K/s. Figure 5.18 shows measured ignition temperatures, which are close to 1000 K independent of the heating rate. The constant ignition temperature is an indicator that the ignition is likely to be triggered by an invariant phase change. A related phase change in titanium is a well-known allotropic transition from α (hexagonal) to β (body-centered) phases occurring in pure Ti at about 1155 K [54]. This phase change has been reported to correlate with marked acceleration in the Ti oxidation [55-56]. The ignition temperature obtained from the heated filament measurements generally

agrees with the ignition temperatures for Ti which were reported by different authors to be in the range of 753 to 1878 K [55-58].

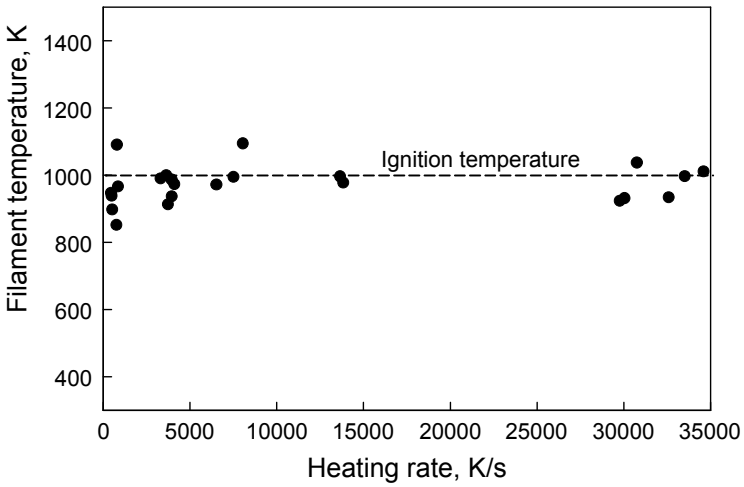

Figure 5.18 Ignition temperature vs. heating rate for Ti sponge powder measured using filament ignition experiments.

5.2 Interpretation of Titanium Experimental Results

5.2.1 Particle Fusing and Powder Layer Resistance

Particle fusing was observed in all experiments for Ti powders prepared as multi-layered samples. No such fusing was observed in previous experiments with Mg and Al powders [51, 53]. In qualitative agreement with the observed formation of fused particle-particle contacts for Ti, the resistance of the Ti powder samples (as shown in Table 5.1) is substantially smaller than that for the samples of Al or Mg with the same thickness [51, 53]. A smaller resistance for the fused powders generally reduces the powder heating by the spark and thus results in its reduced ignition probability and respective fire hazard.

Presence of fused agglomerates and the observed independence of the powder resistance on the sample thickness, as shown in Figure 5.11, suggest that ESD heats a relatively thin layer of Ti powder but not the entire sample depth. Indeed, the powder

resistance is due to inter-particle contacts and when such contact points are fused together, the resistance drops to nearly zero. The measured resistance (Figure 5.11, Table 5.1) is, therefore, due to the fraction of the powder that is not fused. That is the powder fraction heated by the spark and producing ignited particles. Assuming that fusing occurs faster for greater spark currents, it is reasonable to expect that the number of fused particles is expected to increase at increased voltages. The powder fraction that is not fused and thus is primarily Joule heated by the ESD current decreases, respectively. The above reasoning is consistent with the observed reduced powder resistance at higher voltages. When the powder layer thickness increased, the thickness of the fused agglomerate increased as well, which correlates with the relatively small change in the measured powder resistance. It is likely that the particles primarily heated by the spark are located at the top of the powder layer and are most easily lifted by the shockwave generated by the spark. Thus, the increase in the powder layer thickness results in two competing effects. On one hand, the reflected shock wave is more attenuated so that the particles in the top layer are less disturbed, and thus are more likely to fuse together. On the other hand, the voltage drop over each particle-particle contact decreases, resulting in a lower probability of particle fusing.

There are few reports of metal powders fusing in ESD sensitivity tests; however, the phenomenon appears to be similar to the particle fusing occurring at early stages of spark plasma sintering (SPS) [59]. While it is relatively well described in the literature, the mechanisms governing the formation of fused particle-particle contacts are currently unknown. Fusing can occur when the particle surface is heated substantially greater than its interior, a situation that is more likely to occur for Ti, for which the thermal diffusivity

is significantly lower than that for Al or Mg [40]. It is also likely that the electrical and thermal properties of the surface oxide layer determine the voltage at which the electrical breakdown of the particle-particle gap occurs, controlling the rate of heat release and its dissipation, and thus such properties are particularly important for understanding the particle fusing mechanisms. Because of the significant potential of the particle fusing to reduce the ESD sensitivity of powder samples, it is suggested that additional efforts are of interest to identify specific material properties responsible for this phenomenon.

5.2.2 Ignition of Titanium Powders by ESD

In previous work, it was shown that Joule heating of Al and Mg powders exposed to ESD causes their ignition [51, 53]. A similar analysis is of interest for Ti powder. Considering results of the filament ignition experiments (Figure 5.18), it is reasonable to suggest that the powder should ignite when it is heated to about 1000 K. The temperature to which the powder can be heated by the ESD Joule energy is easy to estimate knowing the volume in which the energy release occurs. This volume is defined by the spark radius, r, and the depth of the heated powder layer, h. For the simplest estimate, it can be assumed that the Joule energy, E_{Joule}, is distributed uniformly among all particles, so that the powder temperature, T, can be estimated as:

$$T = T_i + \frac{E_{Joule}}{\pi r^2 h \rho \phi C_p} \tag{5.2}$$

where T_i is the initial powder temperature, ρ, C_p, and ϕ are density, specific heat, and packing fraction of the powder, respectively. This simple estimate neglects particle melting, so T is calculated with a significant error if it exceeds the melting point of Ti, 1941 K. In this paper, Equation (5.2) is only used to identify ignition cases, for which,

based on Figure 5.19, the powder should be heated to 1000 K. Thus, errors made in calculating higher temperatures are unimportant for the purpose of this estimate.

Previously, the entire depth of the powder sample was assumed to be heated by the ESD nearly adiabatically [51, 53], while the spark radius was determined from its imprint on a coated surface [53]. As discussed above, it is likely that not the entire sample depth is heated by the spark, but the only initial estimate available for h is the entire sample depth. Two different evaluations for the radius of the powder cylinder heated by the spark, r, are available. Following earlier work [53], a spark imprint left on a substrate was used to determine the spark radius as shown in Figure 5.4. In addition, the dimensions of the formed agglomerates (Figure 5.5) were also used and gave much greater values for the discharge radii. Using these two different values for r, the entire depth of the powder sample for h, and experimental values of E_{Joule}, different estimated temperatures were obtained for the powders heated by ESD. An assumption that the sizes of the powder cylinders heated by ESD are equal to those of the recovered agglomerates (cf. Figure 5.5) resulted in very low temperatures predicted by Equation (5.2). Predicted powder temperature increase was only of the order of several degrees and was clearly inadequate. Results of the estimates assuming that the radius of the heated powder cylinder is given by the spark imprint radius (Figure 5.4) are shown in Figure 5.20. Different symbols represent experiments performed with different powder sample thicknesses. The estimate clearly predicts ignition for both sponge and spherical powders placed in monolayers. However, predicted temperatures for all other samples are very low, substantially under 1000 K. Once again, even this estimate assuming the smallest reasonable value for the spark radius is in disagreement with the experimental

observations of the ignited particles that must have been heated to higher temperatures. Therefore, it is suggested that the depth of the heated powder layer is actually smaller than the entire sample depth.

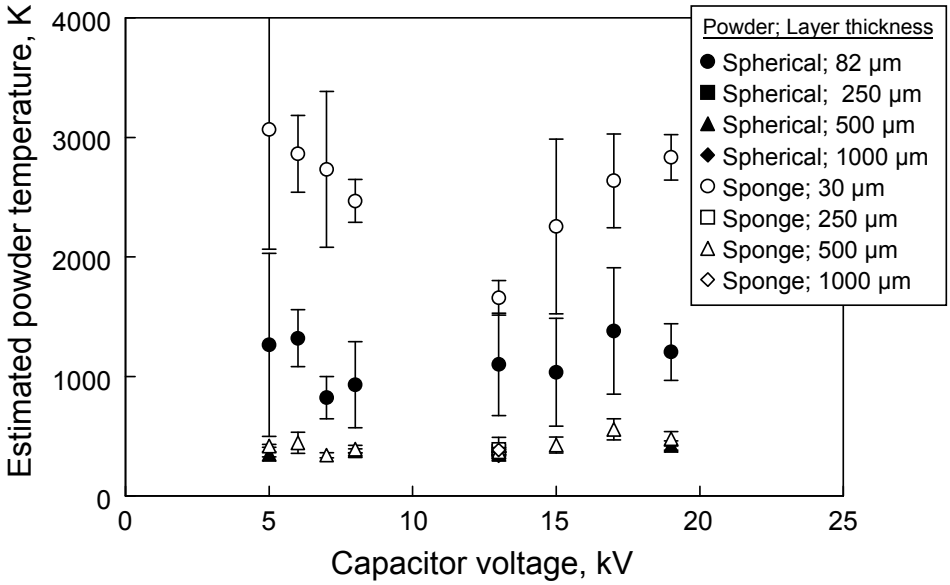

Figure 5.19 Powder temperatures estimated using Equation (5.3) and assuming that the radius of the heated powder cylinder is equal to that of the spark imprint. The depth of the heated powder volume is shown in legend and is assumed to be equal to the entire thickness of the sample tested.

It is possible to solve Equation (5.2) for h assuming a known ignition temperature. Using T=1000 K, values of h were thus calculated for different experimental conditions. These values are shown in Figure 5.20. These estimates suggest that only a monolayer of powder was heated for spherical Ti and possibly two to five layers were heated for sponge powder at the highest ESD voltage setting. It is noted that somewhat thicker layers are heated when higher voltages are applied. Because the thickness of the powder layer heated by the spark to or above the ignition temperature is relatively small, the number of particles ignited is limited. Therefore, interaction between igniting particles is

weak so that only individual particles were observed to burn with no cloud flame formation, independently of the applied voltage or sample thickness.

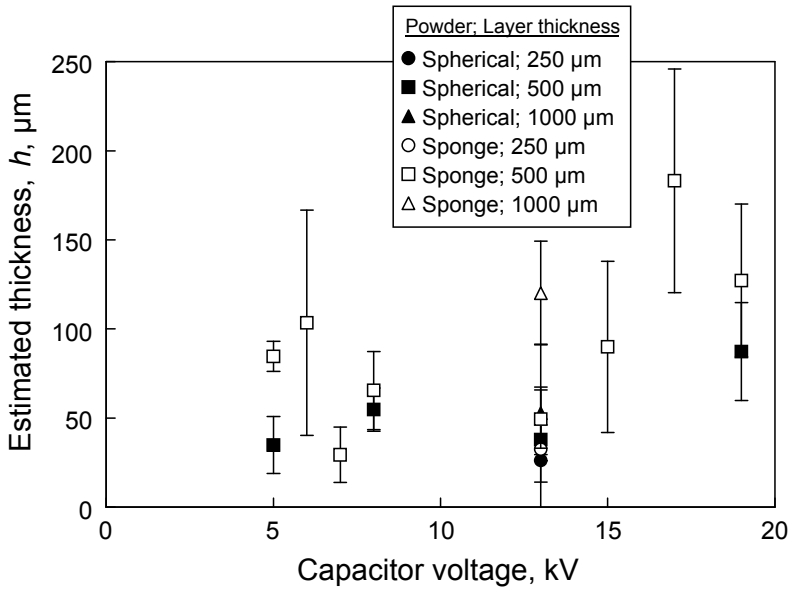

Figure 5.20 Estimated powder layer depths, h, expected to be heated to 1000 K by ESD using Equation (5.2) solved for h and using T=1000 K. The depth of the actual powder sample is shown in legend.

Based on the above estimates, it is suggested that Ti particles ignited by ESD are originated from a very thin powder layer directly heated by the spark. The rest of the sample is not heated, most likely due to the formation of fused particle agglomerates.

The burn times measured for the sponge powder (Figure 5.15) are close to those estimated using correlations suggested in earlier work [60] and particle sizes consistent with the measured particle size distribution (Figure 2.9). For the monolayers, heating particles above the ignition temperature is predicted based on the bulk heat transfer analysis. It also follows from the observed very short burn times (Figures 5.14, 5.15) and small dimensions of the quenched particles (Figures 5.16, 5.17) that the initial Ti particles were disintegrated by the spark, so that burning of the formed particle fragments was observed.

CHAPTER 6

IGNITION OF POWDER AS A FUNCTION OF LAYER THICKNESS

6.1 Experimental Results for Ignition at Different Layer Thicknesses

6.1.1 Powder Volume Heated by the Spark

The energy density of ESD interacting with the powder depends on both the total energy of the spark and on the powder volume in which this energy is dissipated. This volume is calculated as a product of the thickness and surface area of a cylinder within the powder sample that is assumed to be heated by ESD directly. The thickness was initially assumed to be equal to the thickness of the entire sample, and specific measurements were performed to assess its surface area or radius.

For samples prepared as a monolayer, ESDs at 5 kV and 8 kV were applied. Portions of the powder were removed by the discharge and the resulting spark imprints were examined under the SEM. The corresponding imprint areas were determined using UTHSCSA Image Tool v 3.0. Examples of the obtained spark imprints for Mg and Al powders are shown in Figure 6.1. The spark imprints ranged from roughly spherical to irregular in shape, and in many occasion there were multiple spark spots. This indicated that ESD may generate one or several individual streamers. Based on the images, the effective imprint radii were obtained for different voltages and different powders, as shown in Figure 6.2. The radii were calculated as the radii of circles having the same area as the measured area of the imprints. The radii are very close to each other for Al and Mg, while they are greater for Ti. The radii are not noticeably affected by the applied ESD voltage.

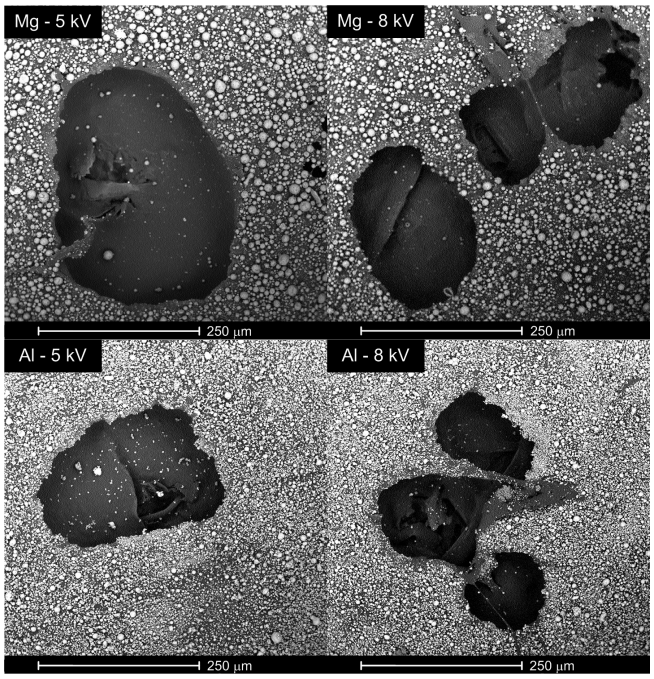

Figure 6.1 Spark imprints produced at different voltages for the Al and Mg powder samples prepared as monolayers.

The ESD imprints were also visualized and measured for the 0.5 mm-thick samples by preparing dilute solutions of powder with liquid adhesive to prevent particle ejection. Samples were loaded slightly wet and dried prior to experiments. SEM images of the imprints obtained for Al and Mg powder samples are shown in Figure 6.3. The area of discoloration in the images was taken as the spark area. For Ti powder, discoloration was not clearly detectable in the SEM images. However, as described in more detail elsewhere [61], Ti particles were observed to be fused by ESD and the size of the fused agglomerates was measured. The radii of these agglomerates were assumed to represent the spark imprint radii. These radii were substantially greater than the radii of the discolored spots on the Al and Mg powder samples. A summary of the measured ESD imprint radii for different sample thicknesses is shown in Figure 6.4. It is apparent that the ESD imprints increase in size with sample thickness; however, this result should be

considered with caution recalling that different data points are obtained using different "spark signatures" and thus may represent different ESD-induced processes.

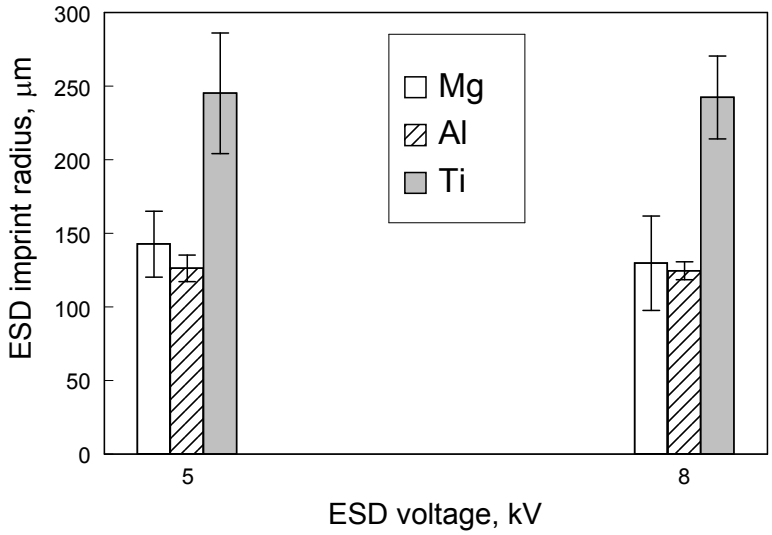

Figure 6.2 Spark imprint radius as a function of the ESD voltage for different powders prepared as monolayers.

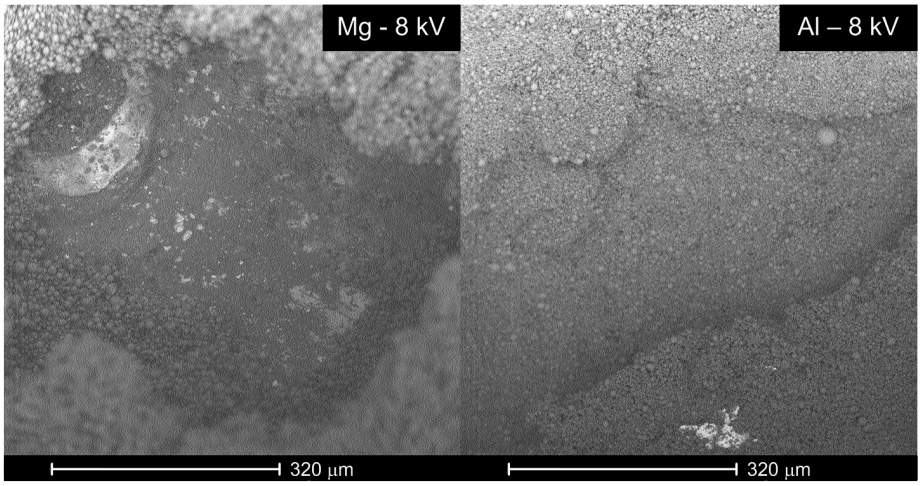

Figure 6.3 Spark imprints produced for the 0.5-mm thick samples of Al and Mg powders prepared with adding a small amount of adhesive to prevent powder ejection. The discolored areas are taken to be spark imprints.

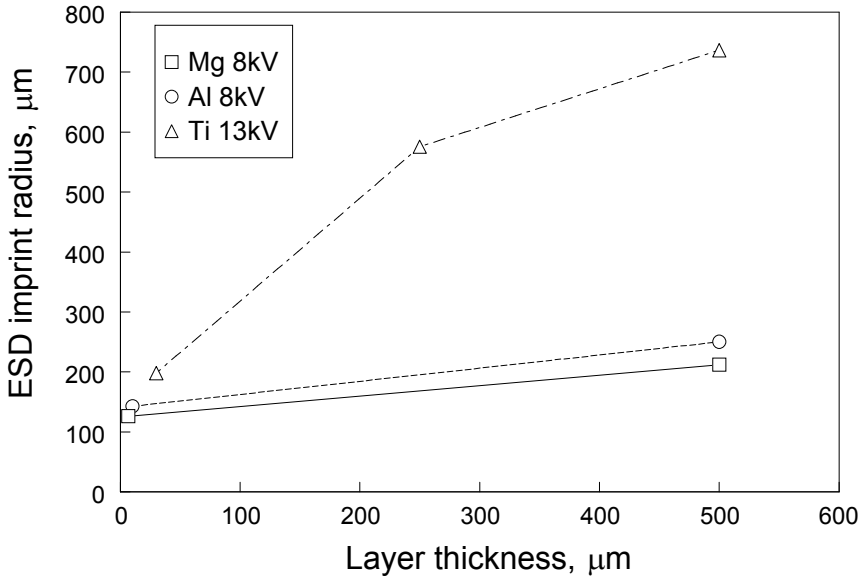

Figure 6.4 Apparent ESD imprint radius as a function of the layer thickness for different powders. Note that different sample preparation techniques and different imprint area measurements methods were used for samples of different thickness and for different materials (see text). ESD voltage is shown in legend.

6.1.2 Powder Resistance and ESD Joule Energy

As in the previous work [51, 53, 61], the powder resistance R_p was determined based on the current traces recorded for the same ESD settings for the sample holders with and without powder. For each experiment, the current trace, showing a decaying oscillatory pattern, was matched with that calculated for an *R-L-C* circuit connected in series. The matching of the experimental and calculated traces was achieved by adjusting the circuit impedance, so that the equivalent resistance for each experiment was obtained. The difference between resistances for the powder-loaded and empty sample holders was assumed to represent the powder resistance. For all three metal powders, the powder resistance increased as a function of the layer thickness, as shown in Figure 6.5. Note that the results are shown in two panels, using the same vertical scale for Al and Mg, but a different scale for Ti. For Ti powder, the resistance is significantly smaller than for Al

and Mg powders. It is also observed that the resistance of a monolayer is a bit greater than that of a thinnest multi-layer sample. These peculiarities in Ti resistance are likely associated with fusing Ti particles, already mentioned above. Measurements also indicate that the powder resistance is decreasing at higher ESD voltage. The last trend is even more clearly shown in Figure 6.6. The results are presented for a fixed powder layer thickness for each metal. In each case, the resistance is decreasing with increased ESD voltage.

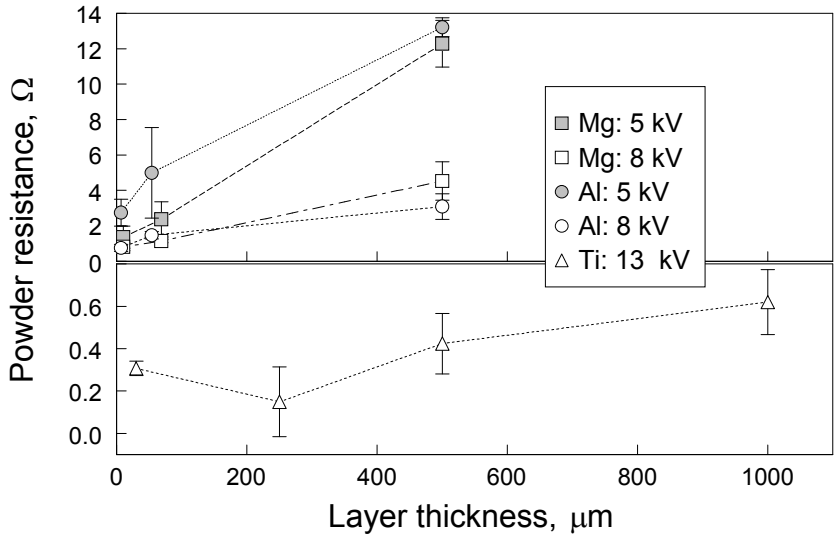

Figure 6.5 Powder resistance as a function of the powder sample thickness for different powders. ESD voltage is shown in legend.

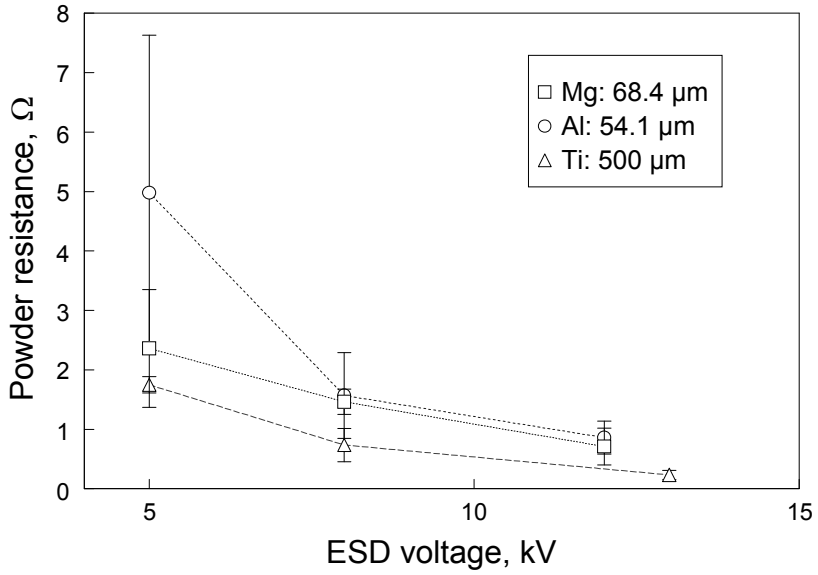

Figure 6.6 Powder resistance as a function of ESD voltage. Powder sample thickness is shown in legend.

Joule heating energy was calculated by Equation (3.3). The results are shown in Figure 6.7. As the layer thickness increased, so did the Joule heating energy. As for the case of powder resistance, the only exception was Ti monolayer, for which the Joule energy was higher than for the 0.25-mm thick layer. For both Al and Mg powders, higher ESD voltage settings resulted in the higher Joule energies for a given thickness. It is interesting that the effect of a smaller resistance for Ti powder (Figure 6.5) is nearly compensated by an increasing current (at a higher capacitor voltage), so that the Joule energy released in Ti powder is comparable to those for Al and Mg powders.

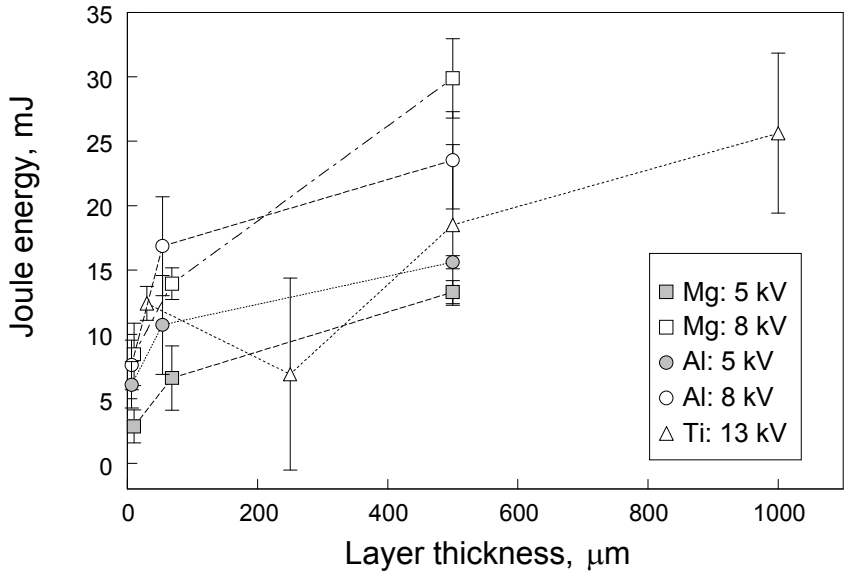

Figure 6.7 Joule energy as a function of layer thickness. Capacitor voltage is shown in legend.

6.1.3 Minimum Ignition Energy (MIE)

The MIE identified based on visual detection of ignition is shown in Table 6.1. These data are shown for reference only, so that the ESD ignition sensitivity of the powders investigated here can be readily compared to the values determined by the current standardized testing corresponding to the shown MIE for 500-μm thick layers. Note that either individual particle streaks or dust cloud flames could represent the visually detected ignition. In the case of Mg, a dust cloud flame was observed at the MIE irrespective of the powder layer thickness. For Al, dust cloud was visible only at a layer thickness of 6.7 μm. For thicker Al powder layers, MIE corresponds to the observed streaks of individual burning particles. For titanium, all MIE values correspond to the observed individual particle streaks.

Table 6.1 MIE of the Metallic Powders Based on Visual Detection of Ignition

Magnesium		Aluminum		Titanium	
Layer thickness, μm	MIE, mJ	Layer thickness, μm	MIE, mJ	Layer thickness, μm	MIE, mJ
10.3	16	6.7	16	30	25
68.5	25	54.1	25	250	25
500	25	500	25	500	25

6.1.4 Burning Modes

Powders ignited by ESD burned in two regimes, which can be classified as a dust cloud flame or combustion of individual particles, producing well-separated single particle streaks. ESD ignited Mg powder always produced a dust cloud flame. Ti powder produced individual particle streaks in all experiments, except ignition of Ti powder prepared as a monolayer with the ESD voltage exceeding 18 kV, when dust cloud flames were observed. Both burning modes were observed for Al powder, with dust cloud flames generally produced for greater ESD energies. Examples of images produced by each burning mode are shown in Figure 6.8.

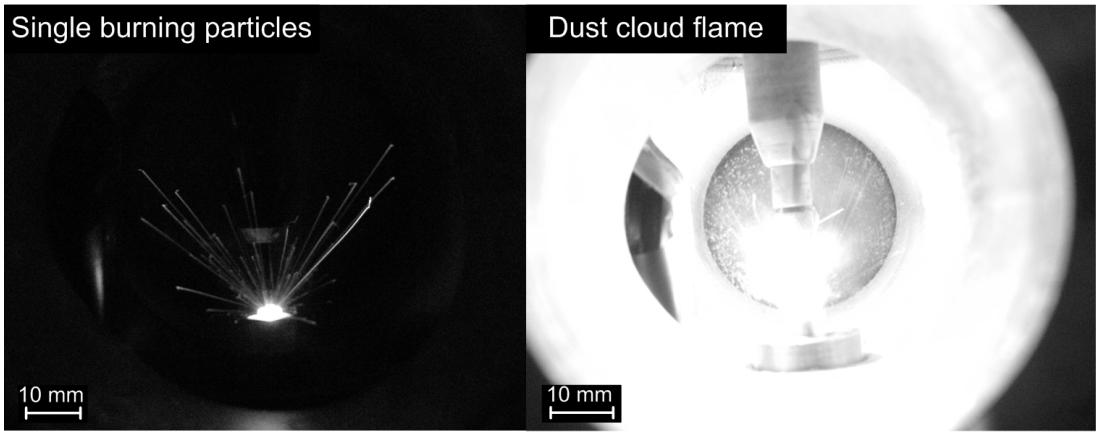

Figure 6.8 Al powder ignited by ESD and producing individual particle streaks (left, voltage 12 kV, thickness 54.1 μm) and dust cloud flame (right, voltage 18 kV, thickness 54.1 μm).

In addition to differences in the visual appearance between the two burning modes, a clear difference was observed in the recorded photodiode traces monitoring combustion. For the events resulting in the individual particle combustion, the initial sharp spike produced by the spark itself was extended in time whereas for the dust cloud combustion, a second broad pulse was produced in addition to the first sharp spike, as shown in Figure 6.9. The onset of the second broad pulse always occurred with a 0.1-0.45 ms delay after the ESD initiation, without apparent effect of the material, voltage, or powder layer thickness.

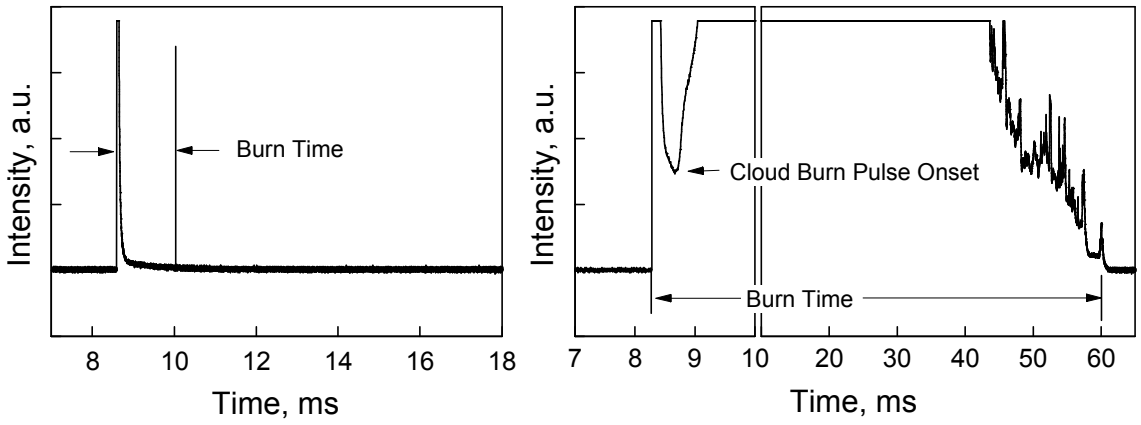

Figure 6.9 Photodiode traces recorded for Al powder ignited with different ESD energies and resulting in individual particle streaks (left, voltage 12 kV, thickness 54.1 μm) and dust cloud flame (right, voltage 18 kV, thickness 54.1 μm).

6.1.5 Flame Dimensions and Particle Ejection Velocity

It was observed that the thickness of the powder layer affected the velocities of the ejected ignited particles as well as the shapes of the produced dust cloud flames. Images of the individual Al particle streaks for powder ignited by 12-kV ESD are shown in Figure 6.10. The image on the left is produced for a 500 μm-thick powder layer; it shows short and bright streaks which are directed at a broad range of angles. Based on the measured streak length and the recorded emission time, the velocity of particles is

estimated to be close to 1.5 m/s. The image on the right is for the 54.1 μm-thick layer; the streaks are noticeably longer and dimmer, indicating particles that move faster. A similar estimate using the streak length and the emission time suggests the velocity of about 5 m/s. The streaks are also more focused vertically, with fewer particles ejected at shallow angles. Interestingly, in both cases, the overall durations of the recorded photodiode signals are close to each other, showing that the burn times of the ejected particles were not affected by the variation in their initial velocities.

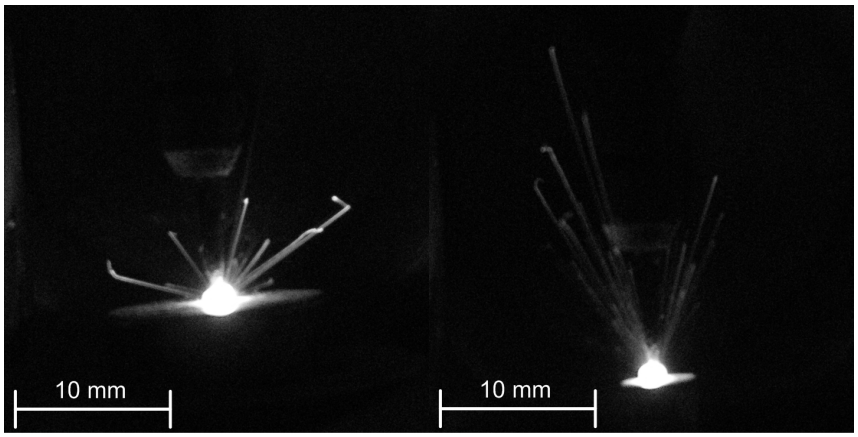

Figure 6.10 Images of the individual particle streaks produced by Al powder ignited by 12-kV ESD when the powder was prepared as a 500 μm-thick layer (left) and 54.1 μm-thick layer (right).

For higher ESD energies, burning dust clouds were produced for the same Al powder samples. The shapes of these flames can be observed from individual frames of a high-speed video record produced at 500 fps and shown in Figure 6.11. There is an apparent difference in the flame propagation patterns for different powder sample thicknesses. For a 500-μm thick samples, the flame spreads horizontally and is not significantly lifted up, even at relatively long times. For a 54.1-μm thick sample, the ESD generates a burning jet rising nearly vertically. A flame is ignited well above the powder sample and is propagated downward at longer burn times. As further discussed

below, for the dust cloud burn regime, the burn times are somewhat longer for the thicker samples.

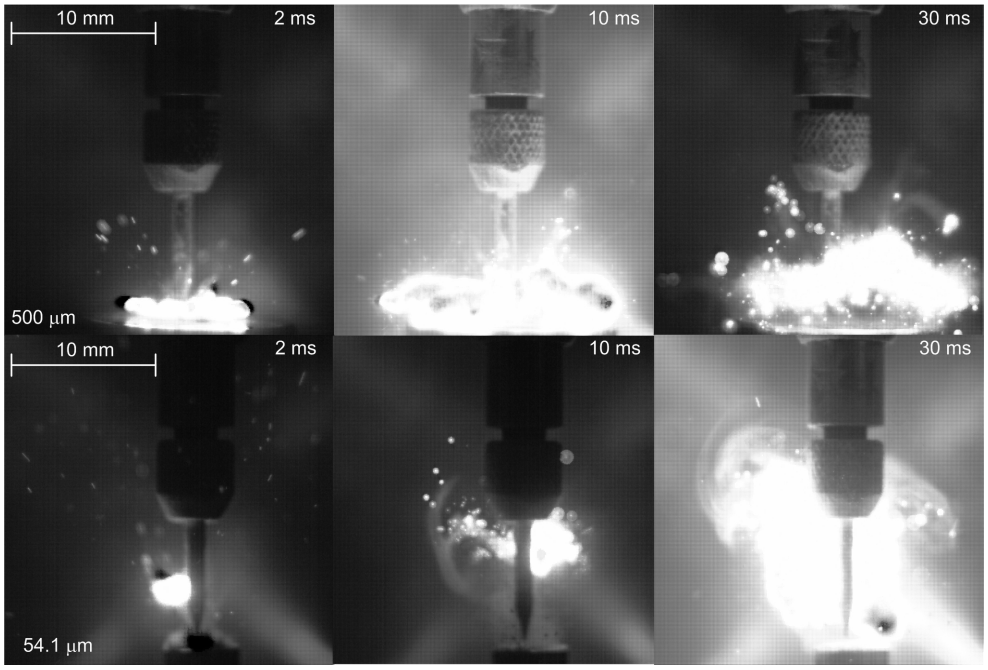

Figure 6.11 Dust cloud flame images captured using a high speed camera at 18 kV at 500 μm-thick (top) and 54.1 μm-thick (bottom) Al powder samples.

6.1.6 Burn Times

Burn times were measured from the beginning of the photodiode spike caused by the spark until the signal was finally reduced to less than 5% of its original baseline level. For the ignition events resulting in the production of individual particle streaks, the burn times were generally substantially shorter than for the events resulting in the combustion of dust clouds. A summary of the measured burn times for different materials, ESD Joule energies, and powder sample thicknesses is shown in Figure 6.12. For Mg which always produced dust cloud flames, greater burn times are consistently observed for thicker powder layers. For Al, burn times less than 10 ms are observed for lower Joule energies, which result in ignition of individual particles. Significantly longer burn times,

approaching 100 ms are observed for greater Joule energies, when Al dust cloud flames were produced. No clear correlation between the burn time and Joule energy is observed for Ti powder.

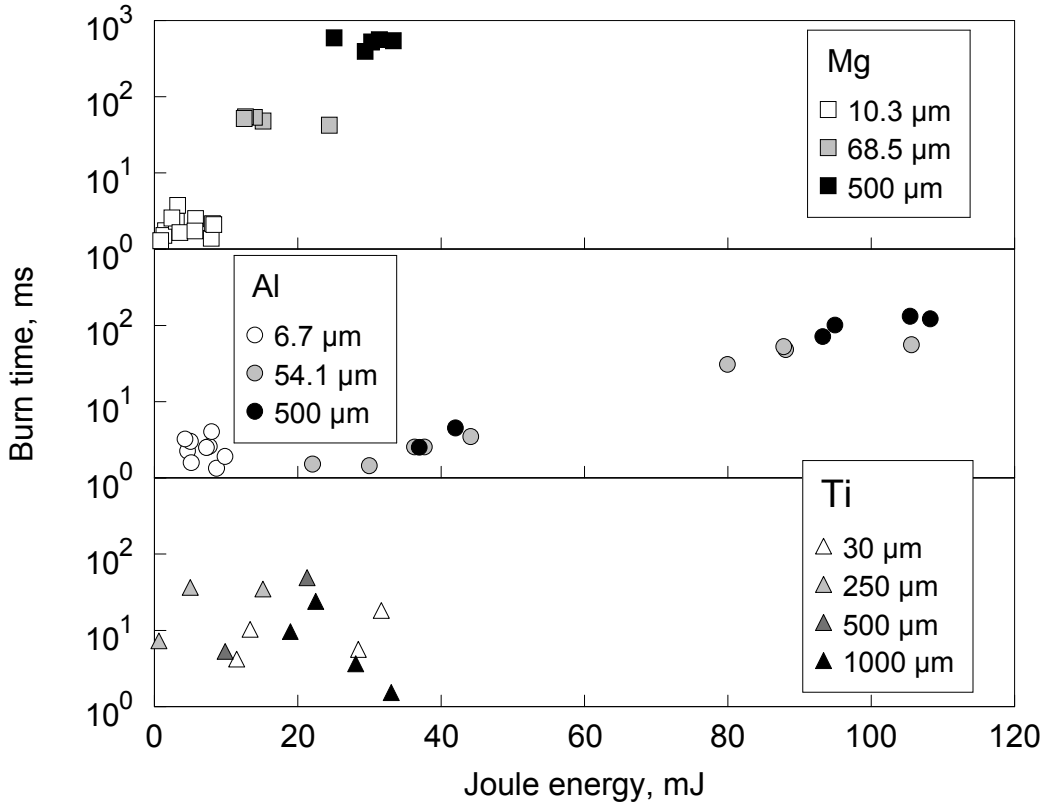

Figure 6.12 Burn time as a function of Joule energy for Mg, Al and Ti.

6.1.7 Particle Fragmentation

The burn times measured for some of the experiments with powders prepared as monolayers were much shorter than anticipated based on the particle sizes used. Therefore, it was attempted to capture particles ejected by the spark under such settings. A silicon wafer was placed approximately 1-3 mm above the sample holder. Burning particles could not be captured, so that the experiments were repeated under argon. In argon, the ejected particles adhered to the silicon wafer and were examined using electron microscopy. Images of such captured particles are shown in Figure 6.13. Very fine, thin,

splat-quenched droplets are observed to form for all metals. The dimensions of these droplets are markedly smaller than characteristic dimensions of the respective starting metal particles. This explains the shorter burn times observed.

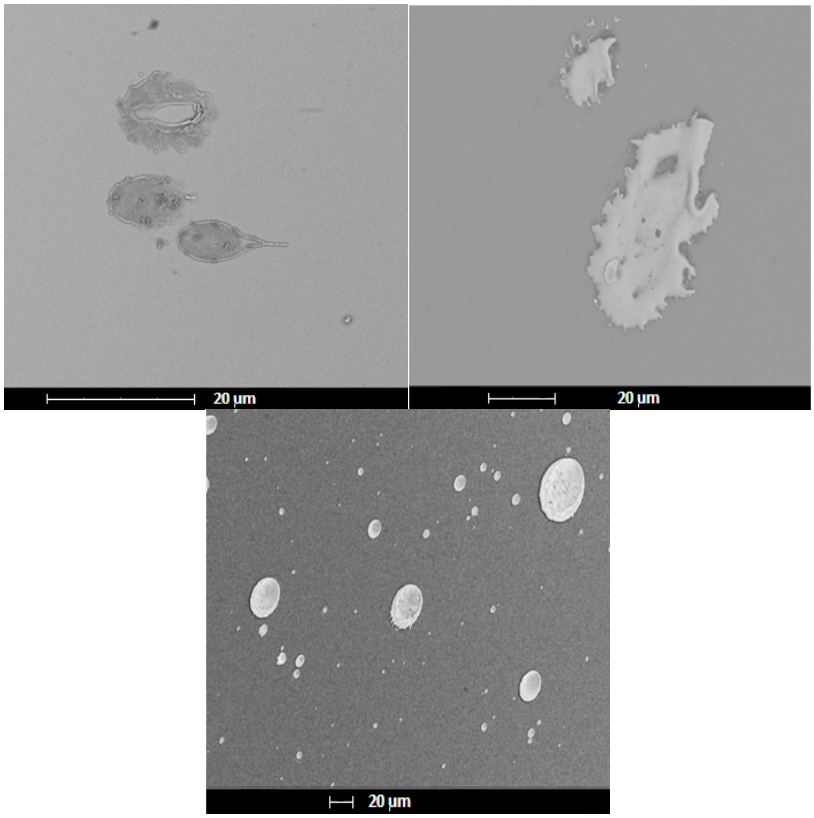

Figure 6.13 SEM image of captured particles ejected from the powder monolayer struck by spark in Ar: Mg (top left), Al (top right), and Ti (bottom center).

6.2 Interpretation of Results of Ignition of Powder at Different Thicknesses

6.2.1 Estimated Temperature of the Igniting Powder

The temperatures to which the metal particles are heated prior to their ignition can be estimated, considering adiabatic heating of the powder by the ESD Joule energy. In the simplest estimate, the Joule energy should be uniformly distributed in the powder volume directly heated by the ESD. This volume can be initially estimated as a product of the powder layer thickness and the effective spark area. The results of these estimates are shown in Figure 6.14. As described above (see Figures 6.1-6.4), the effective spark area was assessed using various spark signatures. It is unknown whether some of any of such assessments truly represent the area directly heated by the spark, so different spark area values (or spot radii, as shown in legend in Figure 6.14) were used to obtain different initial estimates of the respective powder temperatures. To streamline comparison of the estimates for different metals, the shown temperatures are dimensionless and are obtain as ratios of the estimated temperatures to the respective melting temperatures of each metal. It is expected that in experiments, the igniting particles are heated above or at least very close to the metal melting point [56, 62-63], so the estimated dimensionless temperatures that fall far below the value of one are not realistic.

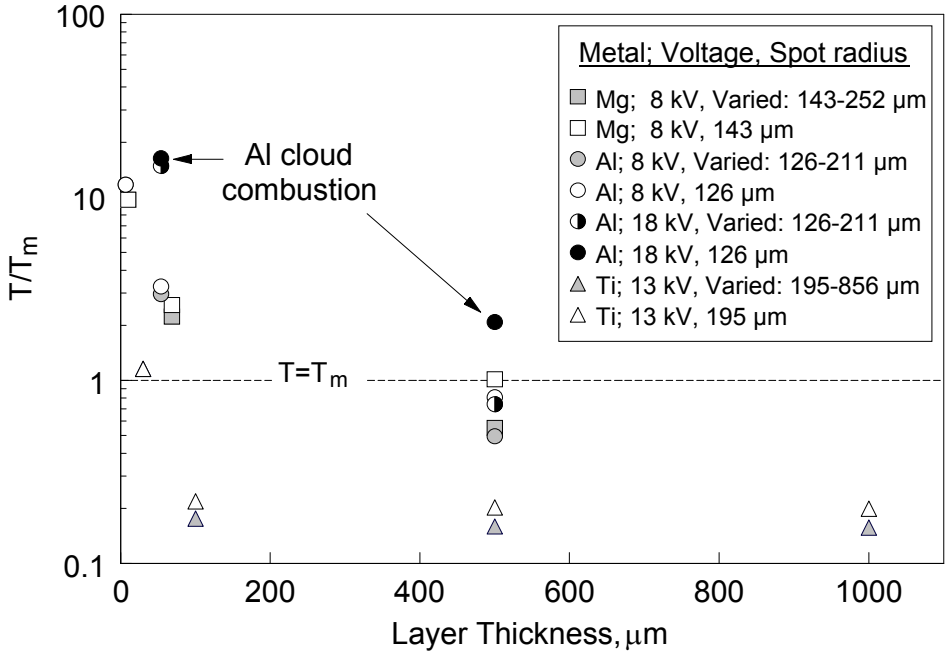

Figure 6.14 Estimated powder temperature as a result of its heating by ESD as a function of powder sample thickness for different metals.

For all monolayer samples, the estimated temperatures shown in Figure 6.14 well exceed the melting points of the respective metals. For Al and Mg monolayers, the estimated temperatures are close to 9000 K, which is much higher than could be attained in experiments. The discrepancy is likely explained by the energy used to fragment and evaporate igniting particles and by radiation heat losses, increasing dramatically as the temperatures exceed approximately 2000 K.

For Ti, the estimated monolayer temperature exceeds slightly its melting point of 1941 K, which is also reported to be the temperature at which Ti ignites [56]. For all increased layer thicknesses for Ti, the estimated temperatures are substantially lower than the Ti melting point. The estimated temperatures are unreasonably low for all available assessments of the spark area. This discrepancy can be interpreted suggesting that only a fraction of the entire Ti powder thickness is heated by the released ESD Joule energy. The rest of the powder is fused and thus poses effectively no resistance to the passing

electric current. Assuming that the igniting powder was heated to 1941 K, the thickness of the heated powder layer was roughly estimated not to exceed two individual Ti powder layers.

For thin layers of Al and Mg (54 and 69 μm, respectively), the estimated particles temperatures are between 2400 and 3000 K. For these metals, the spark area is not a strong function of the layer thickness (Figure 6.4), therefore, the estimated temperatures are nearly the same for differently assessed spark areas. However, for igniting 0.5-mm thick samples of Mg and Al, estimated temperatures become unrealistically low when the spark radii are assumed to vary as a function of the layer thickness as illustrated in Figure 6.4. More reasonable, although still somewhat low temperatures are calculated, assuming that the spark radius remains constant and is assessed using data shown in Figures 6.1, 6.2. Note that powders contained particles of different sizes, which could be heated to somewhat different temperatures [53]. Thus, the bulk powder temperatures estimated to be achieved for 0.5-mm thick Al and Mg powder layers using a fixed spark area (cf. Figures 6.1, 6.2) fall within a reasonably expected temperature range.

6.2.2 Interpretation of Burning Modes

As previously described, two burn modes were observed upon ignition of the metallic powders by ESD. For a dust cloud flame particles interact with one another. The competition for oxygen consumption and heat transfer between burning particles represent the most important interactions. As clearly visible from the flame images for 54.1 μm-thick powder layer in Figure 6.11, for the cloud combustion mode, additional powder can be ignited as the cloud flame develops. Emission pulses produced by the burning particle clouds are much longer and the emission intensity is much higher than

for the cases when ignition is restricted to individual and non-interacting particles, respectively

In the case of Mg, a dust cloud flame was always observed. This is readily understood considering a combined effect of a relatively low Mg particle ignition temperature and a high temperature achieved in the typical Mg vapor phase flame. Thus, even if only a fraction of the Mg particles lifted by the spark is heated to the ignition temperature, the particles that are lifted by the spark and not ignited are likely to be quickly heated to the Mg ignition temperature and contribute to the formation of a burning dust cloud.

For Al powder a dust cloud flame or single burning particles can occur depending on layer thickness and Joule energy. For the monolayer samples, a dust cloud flame was always observed. This observation is consistent with the very high estimated initial temperature of the particles heated in the monolayer; the cloud combustion becomes even more likely because the number of the hot lifted particles is increased due to the observed powder fragmentation. For thicker Al powder layers, single burning particles were observed at low Joule energies while a dust cloud flame occurred at higher Joule energies. It is interesting that the Joule energies required to achieve the cloud combustion regime for 54 and 500-μm thick layers are nearly the same (see points corresponding to long burn times in Figure 6.11); which means that the energy densities and respectively, estimated particle temperatures for these two cases are very different (cf. Figure 6.13). Furthermore, Figure 6.13 indicates that for thinner, 54-μm layers, the temperatures estimated to be achieved for the case of single particle ignition are greater than the temperatures estimated for the case of a cloud ignition for 500-μm thick layers. This

apparent contradiction can be interpreted considering that a much larger number of particles can be lifted by the spark (but not necessarily ignited) for the 500-µm than for 54-µm thick layers. The larger number density of the lifted particles translates into closer proximity between ignited and un-ignited particles, suggesting a higher probability of interaction between such particles.

For Ti, a dust cloud flame was not observed for thicker layer even with an increase in energy density. This may be due to the fusion of Ti particles reducing the number of the particles lifted by the spark and thus the possibility of a dust cloud flame formation. However, it was possible to produce a dust cloud flame with a monolayer of Ti powder at very high energies. As for Al, it is suggested that particle fragmentation producing multiple small igniting particles close to one another contributed to the formation of the burning cloud.

6.2.3 Practical Implications

MIE is dependent on layer thickness for all the powders tested, as shown in Table 6.1. For Al and Mg, MIE decreases with decreasing layer thickness. Conversely, for Ti, the effect of powder layer thickness on MIE is not pronounced; however, different spark energies result in substantially different ignition behavior for all powders. The fire hazard from the ESD-induced ignition is most significantly affected by the observed burning mode (single particle vs. cloud flame), which is not reflected in the current testing methods. For all powders, the spark energies required to produce cloud flames were measured. For Al and Ti, for which both ignition modes are observed for some layer thicknesses, the energies required to achieve the cloud flame and individual particles flames are obtained and shown in Table 6.2. These data can be used to assess

the respective fire hazards. Note that no individual particle flames were observed for Al monolayers and no dust flames were observed for multilayered samples of Ti.

Table 6.2 ESD Energies Required to Achieve Different Burning Modes for Al and Ti Powders

Aluminum			**Titanium**		
Layer thickness, μm	ESD energies for single burning particles, mJ	ESD energies for a dust cloud flame, mJ	Layer thickness, μm	ESD energies for single burning particles, mJ	ESD energies for a dust cloud flame, mJ
6.7	N/A	10	30	11	28
54.1	12	80	250	5	N/A
500	24	71	500	6	N/A

The present results also suggest that the potential fire hazard is affected the velocities at which ignited particles are ejected and respective flame dimensions as shown in Figures 6.10-6.11. The particles ejected from thinner powder layers travel faster and reach further (see Figure 6.10). These particles can potentially ignite other flammable substances at much greater distances compared to particles ejected from thicker powder layers.

CHAPTER 7

NUMERICAL SIMULATION OF LAYER RESISTANCE AND IGNITION

7.1 Motivation

There has been continuing interest in trying to understanding the mechanisms that govern an ESD stimulated ignition event. Many novel materials cannot be scaled up into production because they either fail an ESD sensitivity test or are not available in large enough quantity to perform such a test according to the existing standards [26]. Recent work in ESD-stimulated ignition of metal powders established several important processes and parameters that affect their heating and ignition [51, 53, 61, 64]. It was observed that the spark delivers energy to the powder via its Joule heating. The Joule energy transferred to the powder can be quantified from measurements of the discharge current and powder impedance. The powder is heated by ESD very rapidly (characteristic spark durations are of the order of μs) and nearly adiabatically. It is clear that the powder heating occurs preferentially at the particle-particle contacts, where the electrical resistance is high. However, no quantitative models describing such heating could be found in the literature.

A powder layer can be regarded as a porous material and several methods were used in the past to describe the conductivity in porous materials. Numerous approaches exist that correlate the conductivity of a porous media with the bulk conductivity of the material and the particle size and/or voidage. However, empirical and semi-empirical approaches are limited in describing conductivity. Suitable estimates can be made for mono-sized powders whereas most powders have relatively broad particle size distribution [65-66]. Statistical methods involving percolation theory are commonly used

in describing transport in porous structures [67]. In such methods, a domain is made of randomly connected unit cells where the number of connections made accounts for the voidage inside the porous material. A reasonable agreement in predicting electrical conductivity of sintered compacts, polyethylene composites, and metal-insulator composites was shown for different porosities of various materials [68-70]. However the effects of specific particle size distributions and morphology of individual particle/particle interfaces on the overall conductivity cannot be straightforwardly described.

Alternatively, thermal and electrical conductivities have been modeled analytically, directly taking into account the geometry and arrangement of particles [71-75]. However, mono-dispersed particles were considered by most researchers to enable closing the problem, which severely restricts the practical utility of such models.

Recently, Finite Element Modeling (FEM) was applied to determine conductivity of porous materials [76-77]. Typically, an image of the porous material is taken and the individual phases (solid fraction and pores) are discriminated. A mesh is placed over the selected cross-section of the porous material, and the conduction is numerically calculated taking into account the phases present in the individual elements. Extrapolating the 2D results to account for the 3D structure is often a limiting factor of this method, if the porous material exhibits a complex structure. It is also not always possible to prepare a useful cross-section of the material of interest; in particular, this is difficult for loosely bound powders used in the ESD ignition tests.

Recent advances in Discreet Element Modeling (DEM) over the past few years offer a promising new method for describing conductivity in powders. In DEM, the

number, sizes, and morphologies of the powder particles can be directly simulated. In addition the effect of such material properties as friction coefficients can be factored in while describing its packing in the powder bed. The particle contacts can readily be described taking into account the dimensions of each individual particle. Thus, the effect of the particle/particle interface morphology can be elucidated, which is important for the case of particles heated by ESD.

DEM is used to describe the powder bed so that the electrical resistance network produced by the powder is described directly. The powder heating is then described and the particle temperature distributions as a function of particle sizes, their location in the powder bed, and as a function of the applied ESD energy are considered. The general objective is to enable prediction of the ESD sensitivity for different materials and identify which material parameters must be taken into account to generate such predictions. A specific objective of this modeling effort is to describe and interpret experimental observations on ESD ignition of poly-dispersed, spherical aluminum powders.

7.2 Model

7.2.1 General Approach

Joule heating of the powder bed was simulated. The resistance was assumed to be produced by particle-particle contacts only, while the resistance of bulk metal was neglected. The polydisperse powder sample was simulated using Discrete Element Modeling (DEM). The resistance network inside the simulated powder bed was analyzed and the overall electrical resistance was calculated. The adjustable parameters in the developed model were selected to match the experimental powder resistances obtained at

different powder layer thicknesses and different applied voltages. Finally, Joule heating produced by the current passing through individual particle-particle contacts was evaluated and the heat released was distributed among respective particles in contact.

7.2.2 Powder Bed Simulated by DEM

Commercially available EDEM software [77] was used to simulate a powder layer struck by the electric discharge. Particles were assumed to be spherical in this simulation focused on describing ESD ignition experiments with spherical Al powders [53, 64]. The simulations were available for the particle size distributions (PSD), approximating those observed experimentally [53, 64]. Specifically, the particle size distributions were described by Gaussian functions. Two powders were considered, with nominal particle sizes 3-4.5 and 10-14 μm. The coarser powder was additionally represented as a superposition of coarse and fine fractions (99.5 and 0.5 mass %, respectively), to consider fine particles observed to adhere to coarser particles in the SEM images. The size distribution parameters used in modeling are shown in Table 7.1 with the PSDs of both experimental and DEM numerical generated in Figure 7.1. The particles randomly generated in the gravitational field were allowed to freely settle into a cylindrical sample holder, so that the dimensions of the cylinder determined the total number of particles considered. Settling is affected by static and rolling friction, and coefficient of restitution which are shown in Table 7.2. The powder bed height was chosen to match the experimentally tested configurations [53, 64].

The DEM simulation was typically run until particles stopped shifting and remained in their final positions. The final particle positions were used to simulate the powder resistor network.

Table 7.1 Summary of the Gaussian Distribution Parameters

Powder	Diameter, μm	Standard deviation, μm
Al 3-4.5 μm	6.0	2.1
Al 10-14 μm, coarse fraction	18	5.1
Al 10-14 μm, fine fraction	2.5	0.7

Table 7.2 Summary of the Parameters that Affect Settling

Static friction	0.5
Rolling friction	0.01
Coefficient of restitution	0.5

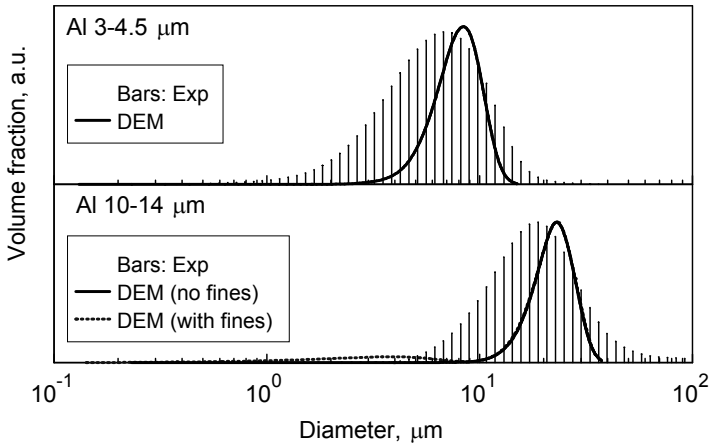

Figure 7.1 Particle size distributions obtained by low-angle light scattering (experimental) and those entered into DEM models for describing packing of Al 3-4.5 μm and Al 10-14 μm powders.

7.2.3 Electrical Resistor Network Outline

The model assumes that the powder is heated by the passing ESD current. The heat release occurs at the contacts between adjacent particles located within the conductive channel created in the powder. Thus, formation of this channel and its resistance are described in the model. The channel is assumed to form after the following sequence of events:

1. An initial discharge streamer(s) originated from the pin electrode passes through the gas gap.

2. Once the conductive channel is created between the pin electrode and one of the particles at the top of the powder layer, secondary streamers pass through the powder layer, breaking down particle-particle contacts from the top to the bottom of the sample.

3. Each individual contact breakdown occurs if the distance between the adjacent particle surfaces is less than 7 μm, a minimum breakdown gap obtained from the Paschen curve in air [78].

4. Once a continuous circuit through the powder to the grounded sample cup is established, the voltage applied to the powder layer drops so no new current pathways are formed. The current channel within the powder has formed.

5. Current flows through the produced micro-discharges while voltage drop between any two adjacent metal surfaces must exceed V_0, the sum of the minimum cathode and anode potentials, depending on the electrode material and spark plasma temperature [79-83]. This condition restricts the diameter of the formed conductive channel.

6. The heat release occurs in the particle-particle contacts, where the main electrical resistance is. This heat is distributed between the contacting particles resulting in their heating.

The produced configuration of the conductive channel in the powder layer is illustrated in Figure 7.2. The electric spark was assumed to comprise of one or more individual streamers. The number of streamers originated from the pin electrode increases at greater spark voltages to match the experimentally observed effect of the applied voltage on the imprint produced by the spark striking a powder layer. Each streamer was assumed to directly strike one of the particles at the top of the simulated powder bed. This assumption was in agreement with the dimensions of the spark cathode and anode spots reported earlier to be in the range of several microns [84-85]; i.e., comparable to the dimensions of individual simulated particles. The number of arc contacts that the spark makes in contact with the powder surface was estimated as a function of capacitor voltage is shown in Figure 7.3.

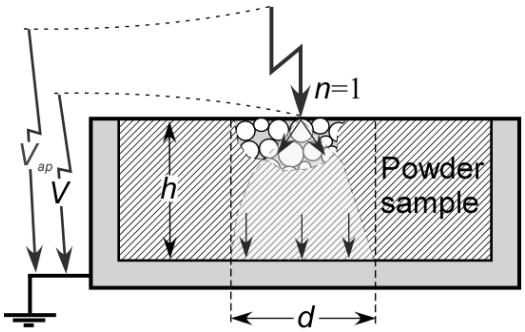

Figure 7.2 Schematic diagram of the powder layer affected by the spark and the conductive channel formed in the layer.

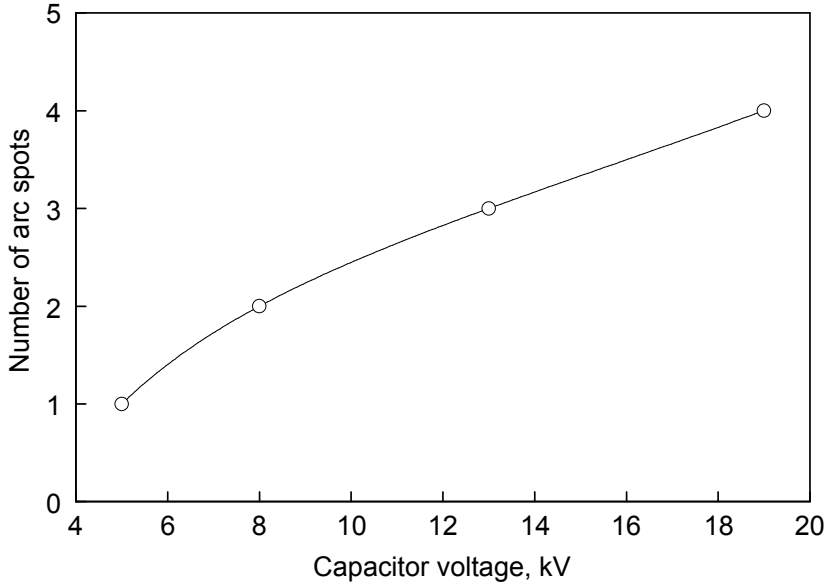

Figure 7.3 Number of arc spots vs. capacitor voltage estimated from the imprints on carbon paper.

7.2.4 Contact Types

Electric discharge can travel through the particles in direct physical contact or separated by small air gaps, as long as the distance between the particle surfaces is less than the break-down distance, l_b = 7 μm, determined based on the respective Paschen curve for the discharge in air [78]. It is assumed that before particle-particle contacts are broken through by micro-discharges, their resistances are very high because particles are not

pressed into one another, so that the surface areas in the direct physical contact are negligible or non-existent. Once the breakdown occurs, the surface area available for the current passing between the particles increases, as described below; this surface area and distance between the particles are used to calculate individual contact resistances.

There are several types of contact that can be made inside the resistor network though which the current travels, examples of which are shown in Figure 7.4. Particles *i* and *j* (see Figure 7.4, top), make an electrical contact with each other if:

$$PP - RR \leq l_b \tag{7.1}$$

where *PP* is the distance between the centers of the particles and *RR* is the sum of the particle radii. *PP* is given by:

$$PP = \left(\left(x_i - x_j \right)^2 + \left(y_i - y_j \right)^2 + \left(z_i - z_j \right)^2 \right)^{0.5} \tag{7.2}$$

where *x*, *y*, and *z* are the coordinates of the centers for particles *i* and *j*. *RR* is given by:

$$RR = r_i + r_j \tag{7.3}$$

where *r* are the radii of the particles *i* and *j*. Particles make contact with the grounded cup (see Figure 7.4, bottom) if:

$$z_i = r_i \tag{7.4}$$

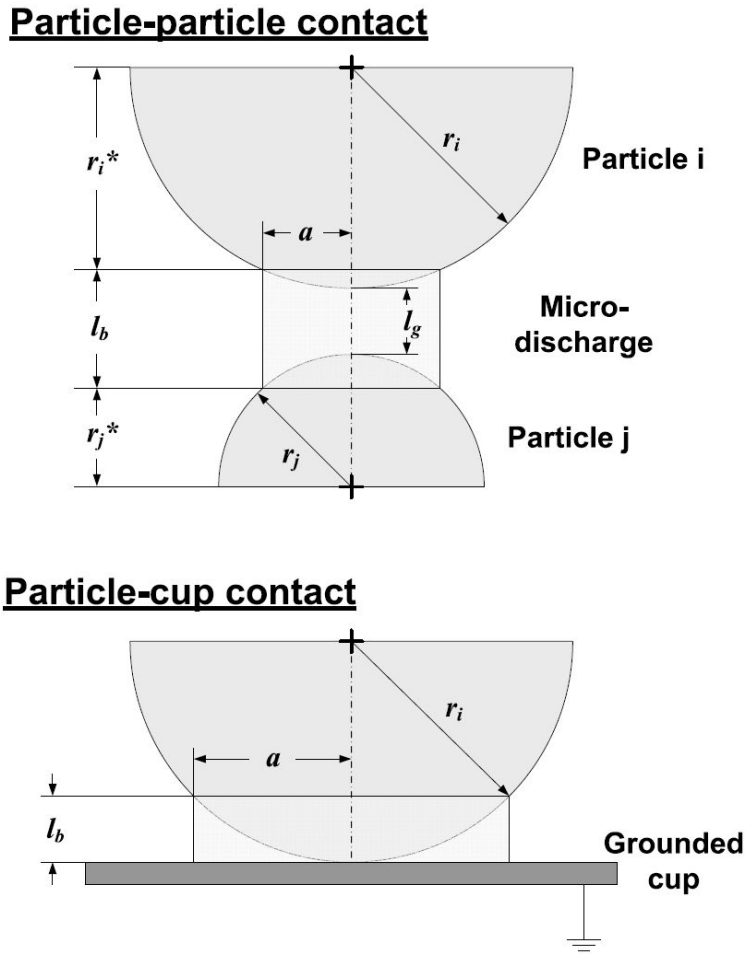

Figure 7.4 Contact types that can be made in the resistor network.

7.2.5 Contact Area

In order to determine the resistance of each contact, the contact area must be known. The contact area is assumed to be equal to the cross-sectional area of the micro-discharge channel. The contact radius (see Figure 7.4) is:

$$a = \left(r_j^2 - \left(\frac{C^2 + r_j^2 - r_i^2}{2C} \right)^2 \right)^{0.5} \qquad (7.5)$$
$$C = r_i + r_j + l_g - l_b$$

where l_g is the gap between particles i and j, so that $l_b \geq l_g \geq 0$. For derivation of Equation (7.5) see Appendix A. Equation (7.5) cannot be used when r_j becomes so small that:

$$r_j^2 < \left(\frac{C^2 + r_j^2 - r_i^2}{2C} \right)^2 \tag{7.6}$$

When Equation (7.6) is satisfied, the contact radius is given by:

$$a = r_j \tag{7.7}$$

In the case of the particle-cup contact, the contact radius is given by:

$$a = \left(2 r_i l_b - l_b^2 \right)^{0.5} \tag{7.8}$$

Once the contact radius, a, is found, the contact area, A is:

$$A = \pi a^2 \tag{7.9}$$

There are also situations that for the particles, for which the condition given by Equation (7.1) is satisfied, there is a third, smaller particle (index k) between particles i and j, as shown in Figure 7.5. If the diameter of particle k is less than that of the micro-discharge channel formed between particles i and j, it is assumed that the channel encloses particle k completely. Particles are enclosed into the discharge when:

$$2 r_k < l_b \tag{7.10}$$

Particles for which Equation (7.10) is satisfied are assumed to be by-passed electrically and do not contribute to the powder impedance; however, these particles are still heated by the spark's plasma (see below).

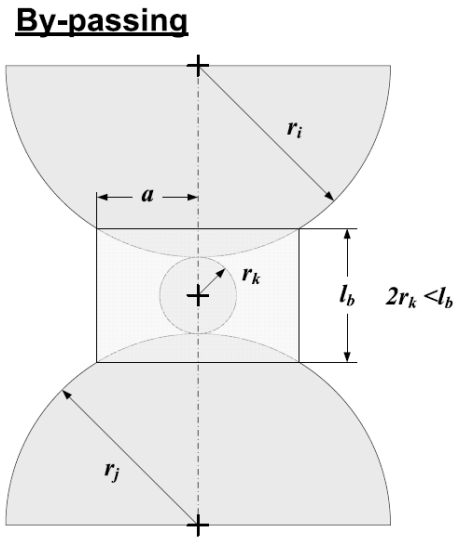

Figure 7.5 Example of a particle being bypassed if the channel size is larger than the particle.

7.2.6 Contact Resistance and Equivalent Layer Resistance

The contact resistance is given by:

$$R = \frac{\rho l_b}{A} \tag{7.11}$$

where ρ is the resistivity of the air plasma existing in the micro-discharge. It is assumed that the resistance is fully defined by the plasma, because the resistivity of metal is much lower than that of plasma [86-87]. The plasma resistivity, ρ, is reported to vary in the range of 10^{-3}-10^{-4} Ω-m [86, 89]. It is treated in the present model as an adjustable parameter selected to match the calculated and measured resistance of the powder layer.

In order to determine the equivalent layer resistance, the current distribution in the powder layer is determined (initially, considering ρ as an unknown constant). Each particle is treated like a node through which the current travels. Assuming that there is no accumulation of charge on the metal surfaces, the current distribution can be found using Kirchoff's circuit laws. The sum of currents entering and exiting a particle is:

$$\sum_i I = \sum_i \frac{V_j - V_i}{R_{ij}} = 0 \tag{7.12}$$

where V_i is the voltage of the particle of interest, and V_j is voltage of the particle/cup that is making contact with particle *i*. Note that $\left|V_j - V_i\right| > V_0$. For a particle at the top of the sample, which has current entering it from the streamer(s) from the discharge pin, the voltage is fixed:

$$V_i = V \tag{7.13}$$

where V is the voltage drop across the entire powder layer. For particles in contact with the cup, the cup voltage is fixed at 0:

$$V_j = 0 \tag{7.14}$$

because the cup is grounded. For each particle (node), the voltage is determined by simultaneously solving Equation 7.12-7.14 for each particle. Once the voltage of each particle is known, the total current through the powder layer is found as the current exiting the particle in the top layer through which the initial discharge streamer enters the powder layer:

$$I_{Tot} = \sum \frac{V_j - V}{R_{vj}} \tag{7.15}$$

where R_{vj} is the contact resistances of all particles in electrical contact with the particle through which the current enters the powder. The equivalent layer resistance is given by:

$$R_{Eq} = \frac{V}{I_{Tot}} \tag{7.16}$$

Parameters used in the mathematical formulation of the model are shown in Table 7.3.

Table 7.3 Parameters Used in the Electrical Resistor Network Model

Type	Parameter	Designation	Function of	Comment
Experimental	Powder layer thickness	h		5 – 500 μm
	Applied voltage	V_{ap}		5 – 20 kV
	Current trace (in time)	$I(t)$		Measured directly
	Number of arc spots (streamers)	N	V_{ap}	Varied from 1 to 4, when 5 kV<V_{ap}<20 kV
	Powder layer resistance	R_{Eq}	h, d, ρ	R_{exp} obtained from $I(t)$
	Joule energy released	E	V, ρ, h, d	E_{exp} obtained from $I(t)$, R_{exp}
Adjustable	The sum of minimum cathode and anode potentials	V_0		Literature data: 1 – 40 V
	Spark plasma resistivity	ρ		Literature data: ~ 10^{-4} Ω·m
	Voltage drop over the powder layer	V	V_{ap}, V_0, h, N, d	Experiment: 100 – 500 V
	Diameter of the arc channel	d	h, V, V_0	Experiment: 40 – 200 μm

7.2.7 Selection of Adjustable Parameters and Model Validation

Table 7.3 contains parameters, many of which are from experiment, and are therefore not adjustable but must be used in matching the model with the experimental data. However, several parameters may not be well defined a priori, including V_0 and ρ. Values reported in the literature vary. These parameters are treated as adjustable and determined from a model calibration. Unlike other adjustable parameters, the values of V_0 and ρ are invariant for all Al spherical powders, for all powder layer thicknesses, and for all ESD voltage settings. The calibration uses a set of experiments measuring the spark current,

voltage, and respective layer resistance and transferred Joule energy for systematically varied applied voltages, powder layer thicknesses, and PSD. These measured data sets are matched with computations by selecting appropriate values of the adjustable parameters.

The following is the calibration algorithm aimed to identify the adjustable parameters included into the model:

1. Set layer thickness, h. Use particle size distribution and a DEM model to create powder fill. Ensure that the sample diameter is greater than the anticipated value of d as shown in Figure 7.6.

2. Create a resistance network considering surface areas of adjacent particles and assuming the breakdown length $l_b = 7$ μm (from Paschen curve in air).

3. Solving Equations (7.1)-(7.16), calculate resistance R_{Eq} as a function of d for a set of values of ρ, varied in the range including various reported literature data as shown in Figure 7.7.

4. For each value of ρ, find d so that $R_{Eq}=R_{exp}$. Obtain $\rho\ (d)$ curve enabling the match of R_{exp} as schematically shown in Figure 7.8.

5. Select a range of V; for each V calculate E as a function of d. Use $\rho(d)$ from step 4.

6. Match E with E_{exp}; find $V(d)$ matching both R_{exp} and E_{exp}, as schematically shown in Figure 7.9.

7. Using the obtained $V(d)$ curve, determine respective $V_0(d)$ curve identifying respective values of the initially unknown V_0. The values V_0 correspond to the (minimum possible) potential differences between the particles sitting on the grounded cup removed by $d/2$ from the discharge channel symmetry axis and the cup itself.

8. Repeat steps 1-7 for different h, for which experimental values of R_{exp} and E_{exp} are available (or interpolated between the measured values). For all values of h, the value of V_0 should be the same, so that the diameter d as a function of h can be found along with the adjustable parameters V_0 and corresponding value of ρ (also invariant for different h).

9. Repeat steps 1-8 for different particle size distributions; matching R_{exp} and E_{exp} for different size distributions with the same values of V_0 and ρ will validate the model.

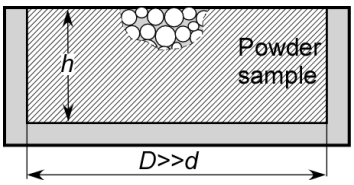

Figure 7.6 Illustration of a powder bed with a diameter much greater than what is needed in order to determine the spot diameter, d.

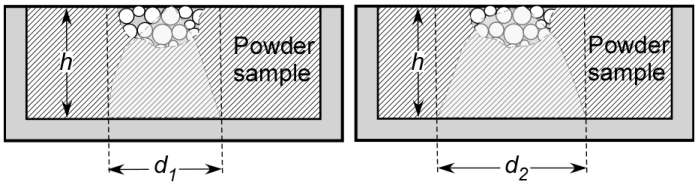

Figure 7.7 Illustration of a powder bed with different spot diameters, d, for corresponding different values of ρ.

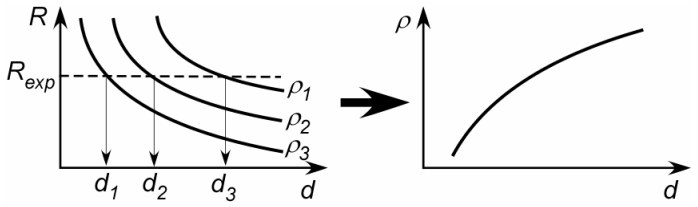

Figure 7.8 Obtaining ρ vs. d curve for a range of resistivities which match the experimental resistance.

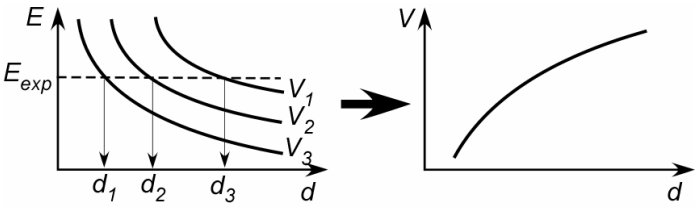

Figure 7.9 Obtaining V vs. d curve, which matches the experimental Joule energy for the same set of resistivties as used in step 4.

7.2.8 Energy Distribution

Once the adjustable parameters are established, the model is used to determine the temperatures of particles heated by the spark. The computed particle temperatures are used to determine which particles ignite. First, the amount of energy that is generated at each contact must be determined and then distributed among the particles making the contact. The amount of energy generated between particles *i* and *j* in electrical contact is:

$$E_{ij} = \frac{\left(V_i - V_j\right)^2}{R_{ij}} \Delta t \tag{7.17}$$

where Δt is the spark duration as measured from the current, $I(t)$. For larger capacitor voltages, the spark time increases. As discussed earlier, the micro-discharge will bypass small particles if Equation (7.10) is met. In addition, particles may be partially enveloped in the micro-discharge. An illustration of the different ways a particle can be heated is shown in Figure 7.10. The contact areas for all particle types are given by:

$$\begin{aligned} &\text{Particle A:} \quad A_c = 2\pi r_i \left(r_i - \left(r_i^2 - a^2 \right)^{0.5} \right) \\ &\text{Particle B:} \quad A_c = 4\pi r_i^2 \\ &\text{Particle C:} \quad A_c = 2\pi r_i h_c \end{aligned} \tag{7.18}$$

where h_c is the spherical cap height that intersects the plasma channel for particles of type C. The contact areas for particles of type A and C are the respective spherical cap areas.

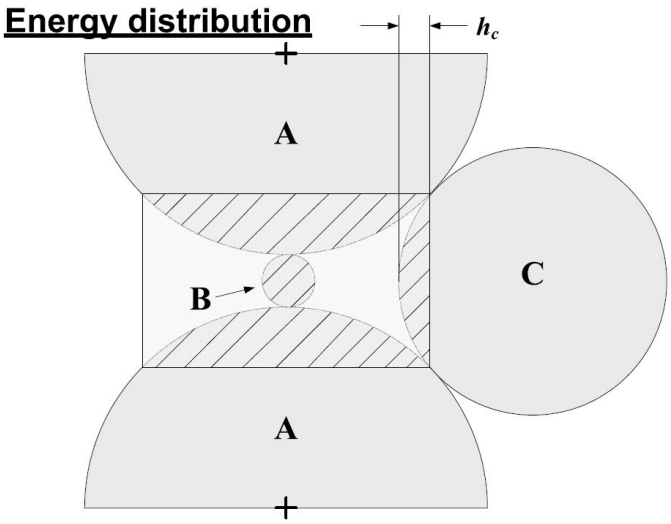

Figure 7.10 Illustration of how the energy is distributed based on how particles make contact with the micro-discharge with the hatch lines showing the area of the particle that is heated. Particles A and A are involved in the breakdown with one another. Particle B is by-passed and is fully enclosed into the plasma, uniformly heating it. Particle C is not involved in the breakdown process of Particles A, but is partially enveloped by the plasma, non-uniformly heating it. Note, additional micro-discharges between A and C and possibly, C and B also form and are considered separately.

The fraction of energy that is delivered to each particle in Figure 7.10 is given by:

$$E_{ij,f} = E_{ij} \frac{A_C}{\sum A_C} \tag{7.19}$$

where A_C is the contact area made with the spark plasma. Once the fraction of energy that can enter a particle from a contact is determined (Equation (7.19)), the total energy that enters a particle is the sum of all fractional energies from all contacts as given by:

$$E_P = \sum E_{ij,f} \tag{7.20}$$

7.2.9 Particle Temperature Outline

1. Each particle is heated adiabatically; any heat losses or heat release due to chemical reactions are neglected.

2. Although the heat release areas are localized around contact points, it is assumed that the heat is uniformly distributed along the particle surfaces.

3. Thermal penetration depth is estimated based on the spark duration and metal thermal diffusivity, all heat is assumed to be uniformly heating the exterior of particles from the surface down to the thermal penetration depth, l_p:

$$l_p = \sqrt{\alpha \Delta t} \tag{7.21}$$

where α is the thermal diffusivity of the bulk metal. Thermal diffusivity is taken at the melting point as it is reliably known and it's relatively constant above the melting point. A particle fully equilibrates if the length of thermal penetration is greater than particle radius as given by:

$$l_p \geq r_p \tag{7.22}$$

4. The metal oxide layer on a particle which is a few nm thick and its influence on heat capacity and other thermal properties of the powder is neglected.

7.2.10 Temperature of a Particle Uniformly Heated

For particles that have that have satisfied Equation (7.22), the temperature of the particle is determined by the following procedure. The energy is normalized by the particle mass in order to determine which phase it is in, as given by:

$$E_{P,m} = \frac{E_P}{m_p} = \frac{3E_P}{4\rho_p \pi r_p^3} \tag{7.23}$$

where m_p is the mass of the particle and ρ_p is the density of the particle. If a particle is still solid, its temperature is determined from:

$$E_{P,m} = \int_{Ti}^{Tp} C_{p,s}(T)\, dT \tag{7.24}$$

where $C_{p,s}(T)$ is the specific heat capacity of the solid particle as a function of temperature, T_i is the initial particle temperature taken to be at room temperature, and T_p is the particle temperature which is solved for. If a particle is melting, its specific energy must satisfy the follow condition:

$$
\begin{aligned}
E_{solid} &= \int_{Ti}^{Tm} C_{p,s}(T)\,dT \\
E_{melt} &= \int_{Ti}^{Tm} C_{p,s}(T)\,dT + \Delta H_{s\to l} \\
E_{solid} &\le E_{P,m} \le E_{melt}
\end{aligned}
\tag{7.25}
$$

where T_m is the melting point of the particle, E_{solid} is the specific energy needed to heat the particle up to the melting point, E_{melt} is the specific energy needed to fully melt the particle and $\Delta H_{s\to l}$ is the specific enthalpy of fusion. If Equation (7.25) is met, the particle temperature is:

$$T_p = T_m \tag{7.26}$$

If a particle has exceeded the upper limit of Equation (7.25) but has not reached the boiling point, the particle temperature is determined from solving the following:

$$E_{P,m} = E_{melt} + \int_{Tm}^{Tp} C_{p,l}(T)\,dT \tag{7.27}$$

where $C_{p,l}(T)$ is the specific heat capacity of the liquid particle as a function of temperature. If a particle is boiling its specific energy must satisfy the following condition:

$$
\begin{aligned}
E_{molten} &= \int_{Ti}^{Tm} C_{p,s}(T)\,dT + \Delta H_{s\to l} + \int_{Tm}^{Tb} C_{p,l}(T)\,dT \\
E_{boiled} &= \int_{Ti}^{Tm} C_{p,s}(T)\,dT + \Delta H_{s\to l} + \int_{Tm}^{Tb} C_{p,l}(T)\,dT + \Delta H_{l\to v} \\
E_{molten} &\le E_{P,m} \le E_{boiled}
\end{aligned}
\tag{7.28}
$$

where T_b is the boiling point of the particle, E_{molten} is the specific energy needed to bring the particle to the boiling point, E_{boiled} is the specific energy needed to fully boil off the

particle, and $\Delta H_{l \to v}$ is the specific enthalpy of vaporization. If Equation (7.28) is met, the particle temperature is:

$$T_p = T_b \tag{7.29}$$

If a particle reaches or exceeds the upper limit of Equation (7.28), the particle is boiled off. Although the boiling off of a particle can sever the continuity in the electrical resistance network, it is assumed that continuity is maintained even for particles that have boiled off. The effect and validity of this assumption will be discussed when obtained particle temperatures are presented.

If a particle has more energy than is sufficient to boil it off, the excess energy is distributed among particles in contact with it. The excess energy is given by:

$$E_{excess} = m_p \left(E_{p,m} - E_{boiled} \right) \tag{7.30}$$

The fraction of the excess energy distributed to each contacting particle is based on the respective contact area:

$$E_{excess,f} = E_{excess} \frac{A_C}{\sum A_C} \tag{7.31}$$

This fraction of the excess energy is added to the total energy entering a particle, E_p.

7.2.11 Temperature of a Particle Not Uniformly Heated

For particles that do not satisfy Equation (7.22), a l_p–deep layer of the particle is uniformly heated. The interior of the particle, for which the radius is less than l_p remains cold. Should the outer layer of the particle not exceed the boiling pt. of the metal, than it is assumed that the entire particle will equilibrate in a few μs after the spark heating. Therefore, Equations (7.23)-(7.29) can be applied to particles whose thermally penetrated volume does not begin to boil. Those particles with the thermally penetrated volume

beginning to boil as well as particles which are uniformly heated and begin to boil are discussed in the next section.

7.2.12 Partial Boil Off of a Particle

During spark heating, particles that begin to boil reduce in size. This is of particular importance when estimating the expected burn times for the ignited particles, which can be compared to those observed in experiment. The thermal penetration length will limit how much of the particle volume reaches thermal equilibrium. It will also affect the prediction on how much material will partially boil as illustrated in Figure 7.11. In order to determine if a fraction of the particle can boil off for a particle that does not fully equilibrate (Equation (7.22) is not satisfied), the energy of the particle is first normalized by the mass through which the thermal penetration occurs.

$$E_{pv} = \frac{3E_p}{4\pi\rho_p\left(r_p^3 - \left(r_p - l_p\right)^3\right)} \tag{7.32}$$

If E_{pv} falls in the specific energy range as given in Equation (7.28), then a fraction of the particle will boil off. The amount of energy that is available to boil off a fraction of the particle is given by:

$$E_{fb} = 4\pi\rho_p\left(r_p^3 - \left(r_p - l_p\right)^3\right)\left(E_{pv} - E_{molten}\right) \tag{7.33}$$

Therefore the new particle radius after a fraction of the particle boils off is given by:

$$r_n = \left(r_p^3 - \frac{3E_{fb}}{4\pi E_{boiled}}\right)^{1/3} \tag{7.34}$$

For a particle which fully equilibrates during the spark heating, partial boiling can be determined directly by Equation (7.28). If Equation (7.28) is satisfied, the amount of energy that is available to boil off a fraction of the particle is given by:

$$E_{fb} = 4\pi\rho_p r_p^3 \left(E_{pv} - E_{molten}\right) \tag{7.35}$$

The new particle radius for a particle that fully equilibrates and partially boils off is given in Equation (7.34). In order to determine the particle temperature, the remaining energy is re-normalized with the mass of particle accounting for the new reduced radius of the particle. For a particle which had not fully equilibrated, the remaining energy is distributed as:

$$E_{p,m} = \frac{\left(r_n^3 - \left(r_p - l_p\right)^3\right)}{r_n^3} E_{molten} \tag{7.36}$$

For a particle that had fully equilibrated, the specific energy of the particle is given by:

$$E_{p,m} = E_{molten} \tag{7.37}$$

The temperature of the particles partially boiled off can be determined as previously described in Equations (7.23)-(7.29).

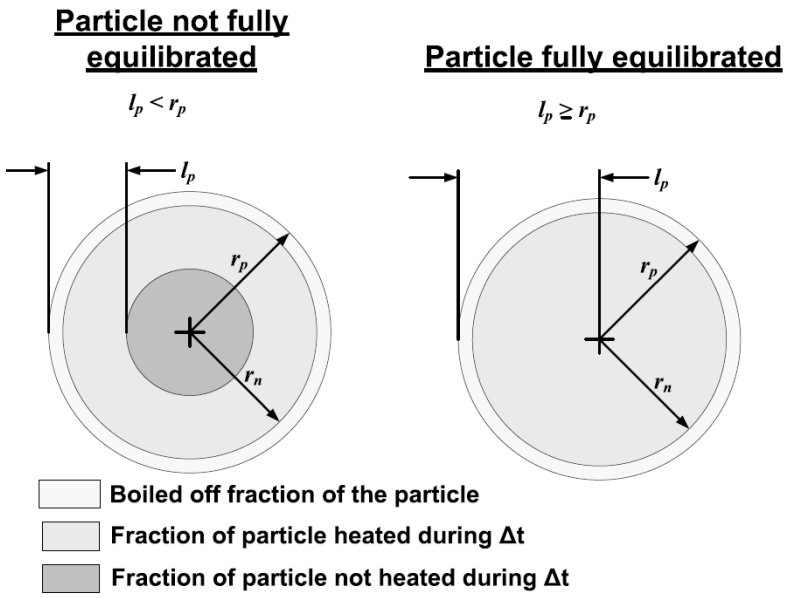

Figure 7.11 Particle on left not fully equilibrated during the spark duration and particle on right fully equilibrated during the spark duration.

7.3 Calibration Results

7.3.1 Resistance vs. Spot Diameter

Table 7.4 shows a summary of the powder layer thicknesses, resistances, spark durations, and ranges of Joule energies measured at 5 kV and 8 kV for Al 10-14 μm and Al 3-4.5 μm. The energy levels of min, avg, and max are introduced to illustrate the spread between respective measurements for nominally identical experimental settings. Parameters shown in Table 7.4 were reproduced in numerical simulations to characterize the electrical resistance and heating of Al powders by the ESD. The thickness of the powder layer for 10-14 μm powder was 450 μm, slightly less than 500 μm. The powder layer thickness is obtained after the EDEM simulation, and additional simulations were not performed because the discrepancy is within the experimental error bar. To reproduce conditions at 5 kV, the current entered the powder through one streamer. At 8

kV, two streamers were considered, in agreement with Figure 7.3. The voltage applied to the powder layer was adjusted to reproduce the values of the Joule energies shown in Table 7.4. The model was calibrated for aluminum powder for a capacitor voltage of 5 kV, at the average energy level.

Table 7.4 Experimental Resistance, Joule Energy, and Spark Duration for Al 10-14 μm and Al 3-4.5 μm, at 5 kV and 8 kV

Nominal particle sizes	Applied voltage, kV	Spark duration, μs	Powder layer resistance, Ω	Layer thickness, μm	Energy level	Joule energy, mJ
Al 10-14 μm	5	1.5	4.34	500	Min	3.56
					Avg	9.15
					Max	14.5
	8	2.5	1.49		Min	10.1
					Avg	16.1
					Max	20.7
Al 3-4.5 μm	5	1.5	4.99	50	Min	3.00
					Avg	10.7
					Max	15.0
			5.84*	100*	Avg	11.2

*Interpolated from experimental data for a smaller and greater layer thickness

Figures 7.12-7.15 show calculated equivalent layer resistance, R_{Eq}, plotted vs. spot diameter, d, for a range of plasma resistivities, ρ; the calculations are compared to the experimental resistance values R_{exp}, shown in Table 7.4. For Al 10-14 μm, the calculations are performed for two particle size distributions, with and without an additional fine particle fraction, noticeable in the SEM images but not reflected in the PSD measured by light scattering, as discussed above. Calculated resistance decreases with increasing spot diameter for all the simulations; at greater spot diameters the change in the resistance diminishes. Reducing the plasma resistivity decreases the equivalent layer resistance.

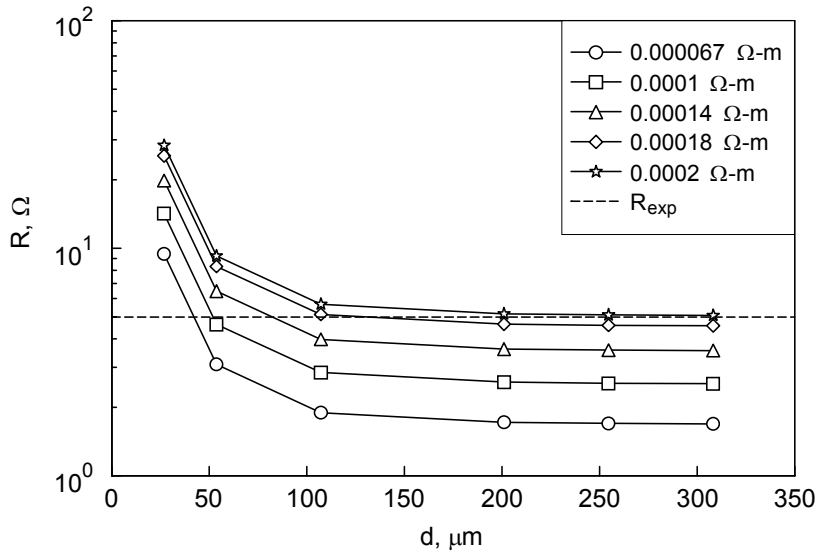

Figure 7.12 Powder layer equivalent resistance vs. spot diameter for a 50-μm thick layer of Al 3-4.5 μm powder; plasma resistivities used in calculations are shown in legend.

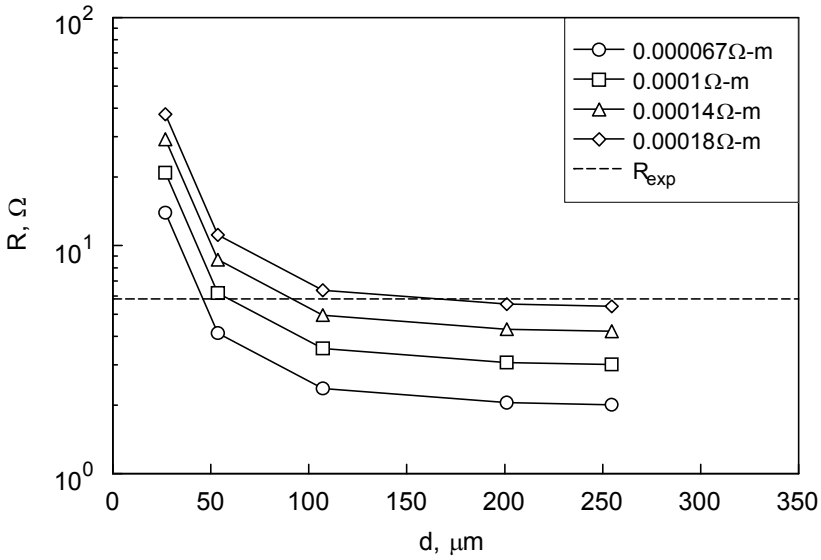

Figure 7.13 Powder layer equivalent resistance vs. spot diameter for a 100-μm thick layer of Al 3-4.5 μm powder; plasma resistivities used in calculations are shown in legend.

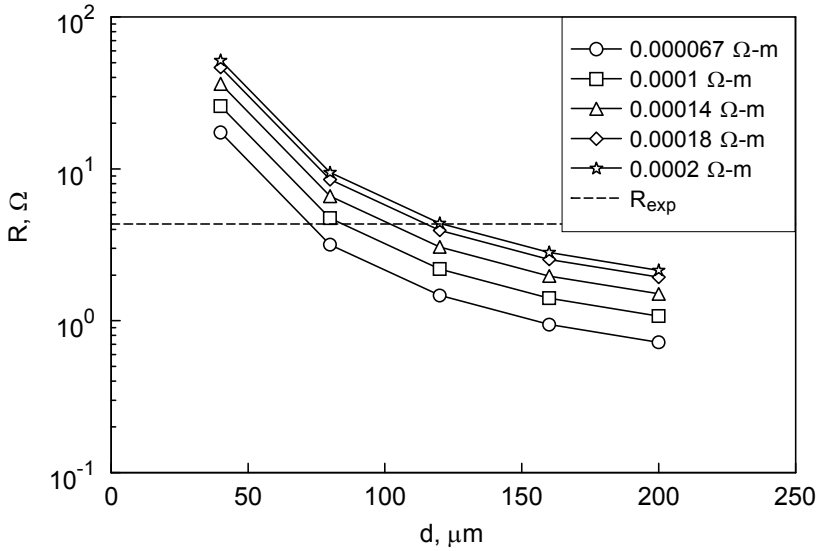

Figure 7.14 Powder layer equivalent resistance vs. spot diameter for a 500-μm thick layer of Al 10-14 μm powder (without fines); plasma resistivities used in calculations are shown in legend.

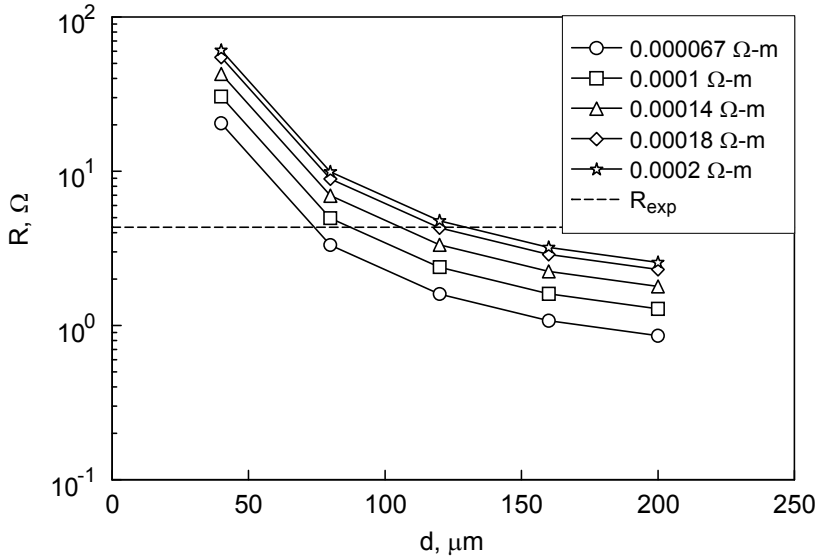

Figure 7.15 Powder layer equivalent resistance vs. spot diameter for a 500-μm thick layer of Al 10-14 μm powder (with fines); plasma resistivities used in calculations are shown in legend.

7.3.2 Spot Diameter vs. Resistivity

Spot diameter vs. plasma resistivity is shown in Figure 7.16 for all the simulated cases, for which the experimental and calculated equivalent powder layer resistances match. Generally, the spot diameter increases with increasing resistivity. For both Al 3-4.5 μm simulated cases, the spot diameter vs. resistivity are comparable. Comparable spot diameters are also observed for both Al 10-14 μm simulated cases. The predicted effect of plasma resistivity on the spot size is generally stronger for the finer Al powder.

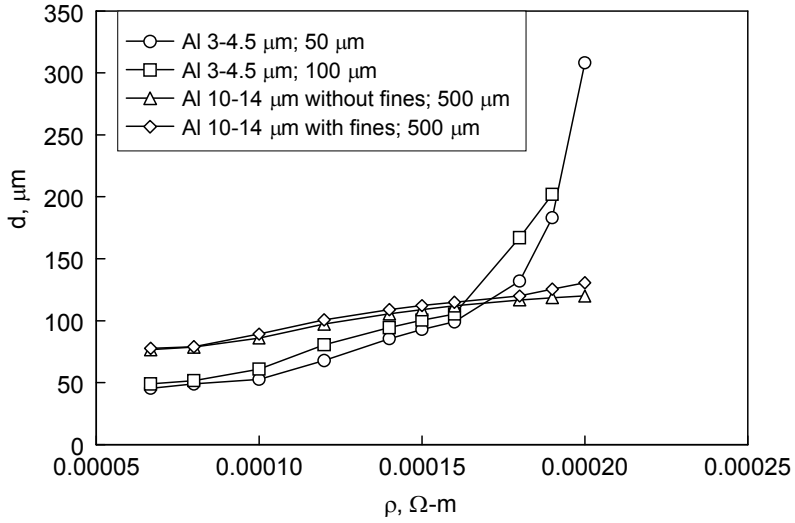

Figure 7.16 Spot diameters vs. plasma resistivity for which the experimental resistance matches the calculated value. Each curve corresponds to a specific particle size distribution and layer thickness, as shown in legend.

7.3.3 Joule Energy vs. Spot Diameter

Calculated Joule energy vs. spot diameter for 50-μm and 100-μm thick layers of Al 3-4.5 μm powder is shown in Figure 7.17 for a range of voltages, V, applied to the powder layer. The dashed line corresponds to the experimental Joule energy listed in Table 7.4. The energy is a strong function of the spot diameter for very small diameters, with a less pronounced effect for greater spot sizes. The value of voltage, V, considered in the model

to be applied to the powder layer that matches the experimental Joule energy varies in a relatively narrow range of 180-200 V.

Calculated Joule energies vs. spot diameter for a 500-μm thick layer of Al 10-14 μm powder modeled with and without the fine fraction are shown in Figure 7.18 for a range of voltages, *V*. In this case, the value of *V* needed to match the experimental Joule energy is slightly above 150 V. A lower voltage is needed for Al 10-14 μm than for Al 3-4.5 μm because a lower experimental Joule energy was measured.

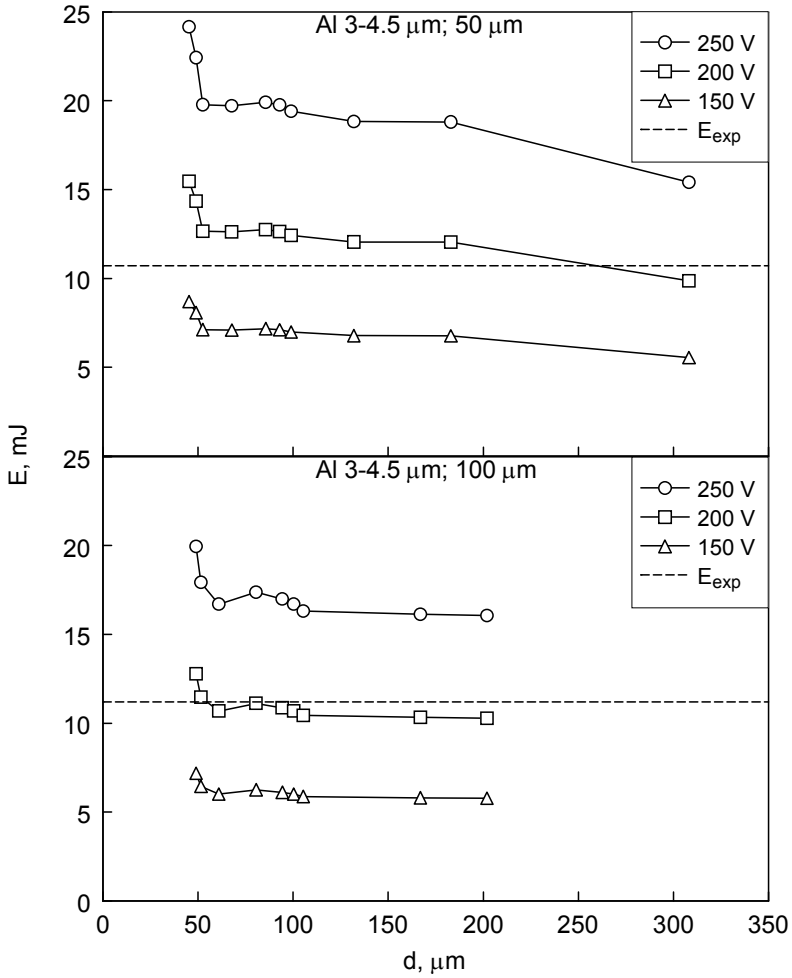

Figure 7.17 Joule energy vs. spot diameter for selected voltages for Al 3-4.5 μm powder at 50 μm and 100 μm layer thicknesses.

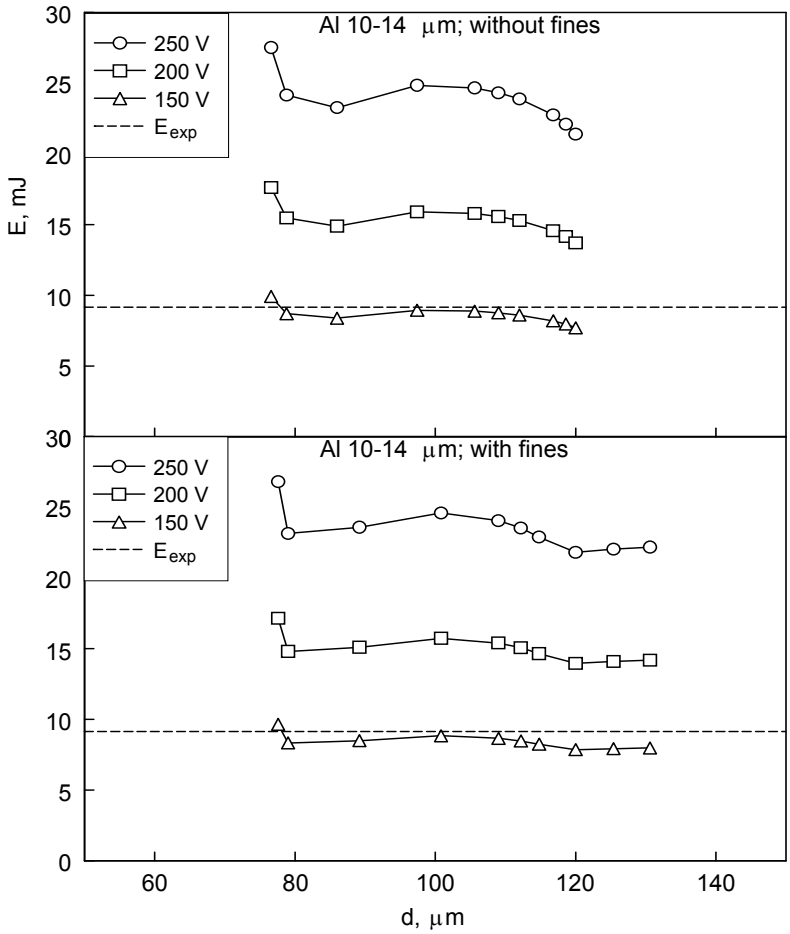

Figure 7.18 Joule energy vs. spot diameter for selected voltages for Al 10-14 μm powder (modeled without and with fine particle size fraction) at 500 μm layer thickness.

7.3.4 Voltage Distribution and Electrode Fall Potential

Figure 7.19 shows an example of the voltage distribution over a horizontal line drawn within the powder bed. The data are for Al 10-14 μm powder with fines. Three voltage distributions shown were obtained for the horizontal lines at the top, middle, and bottom of the powder bed. The voltage is applied to a particle at the center of the top particle layer. The strongest voltage gradient is seen for particles where the spark current enters the powder, in the top-most layer. Weaker voltage gradients are observed for particles in the middle and bottom layers. The bottom-most layer is generally only a few volts above

ground. The voltage drop for particles contacting the grounded cup and removed by one half of the spot diameter from the vertical axis through which the initial discharge streamer enters the powder, is the minimum voltage drop which should be equal to the electrode fall potential, V_0.

Figure 7.20 shows the electrode fall potential V_0 inferred by the calculation and plotted vs. plasma resistivity, ρ. Each curve in Figure 7.20 shows the values of V_0 and ρ corresponding to the experimental Joule energy and equivalent resistance for the respective powder layers. For Al 3-4.5 μm powder, the calculated value of V_0 decreases with increasing ρ. There is almost no change in the calculated V_0 for Al 10-14 μm powder. Because for the same material (Al) ignited in the same environment (air), both V_0 and ρ are independent of the powder layer thickness and particle size distribution, the curves in Figure 7.20 are expected to intersect in a single point, identifying the actual values of V_0 and ρ . The intersection of the curves occurs for the plasma resistivity of about 0.0002 Ω-m and the electrode fall potential of about 9-10 V.

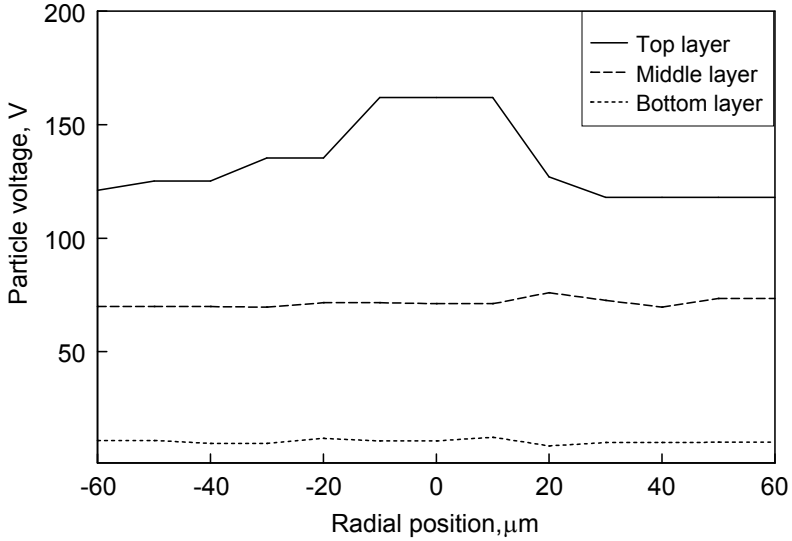

Figure 7.19 Example of voltage distribution in the powder layer for Al 10-14 μm showing the particle voltage as a function of radial position in the top layer, middle layer, and bottom layer.

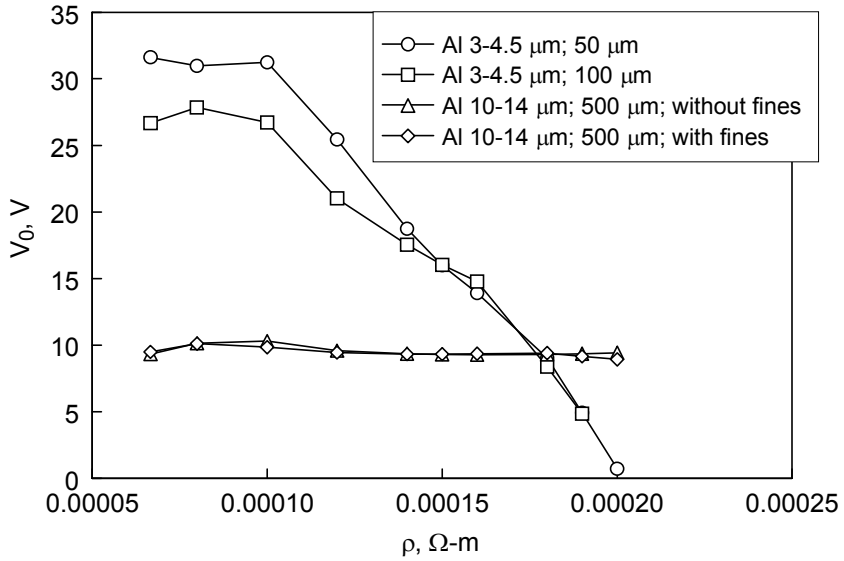

Figure 7.20 Electrode fall potential, V_0, vs. plasma resistivity, ρ, inferred from the simulations, for which both electrical resistance and measured Joule energy are matching the respective computed values.

7.3.5 Sensitivity to the Spark Spot Location

The calibration results above were conducted with a particle at the top of the sample arbitrarily chosen for the spark streamer to attach to. Therefore, the location of this specific particle and a number of contacts it has with its neighbors may have a strong effect on the overall current distribution in the sample. In order to determine the effect of the source particle on the circuit, calculations were repeated with different particles selected for the streamer to attach to. Results showing the spot diameter obtained in order to match the experimental Joule energy and resistance from Table 7.4 (for Al 10-14 μm with fines) is shown in Table 7.5. Calculation with one of the particles (coordinates 0, 0) yields a spot diameter significantly larger than the others. This difference is due to different number of particle contacts. For Al 3-4.5 μm, a similar study was not done given that V_0 vs. ρ were consistent at for both considered powder layer thicknesses, 50 and 100 μm.

Table 7.5 Effect of the Spark Spot Location on the Diameter of the Powder Volume Directly Heated by the Spark (Al 10-14 μm with Fines)

Coordinate of the "source" particle, μm	Spot diameter, μm
0,0	280
50,0	120
-50,0	116
0,50	122
0,-50	118

7.3.6 Sensitivity to the Distance Between Spark Streamers at Higher Voltages

The sensitivity of results to the selected distance between particles directly struck by the spark streamers was judged by the predicted change in the powder layer resistance. The calculations were performed for Al 10-14 μm with fines at the average energy level and 8

kV. The diameter of the computational domain containing the powder was chosen to be 220 μm, so that the particles struck by the spark could be separated by up to 150 μm. A desired or nominal separation was pre-selected and then the code selected two particles in the top powder layer separated by a distance close to that pre-selected. Therefore, the actual distance between the particles varies somewhat randomly. Results are shown in Table 7.6. For reference, a calculation with a single streamer is also shown, for which the powder layer resistance is 1.98 Ω. Splitting the spark into two streamers reduces the equivalent resistance by less than 25 %. The powder layer resistance is a weak function of both sizes of the "source" particles and their separation. It is likely more affected by the number of contacts each "source particle has. For determining particle temperature, a nominal distance of 60 μm between the two streamers was chosen, which matched closely both experimental powder layer resistance and Joule energy shown in Table 7.4.

Table 7.6 Effect of Distance Between Spark Streamers Entering the Powder on Powder Layer Resistance for Al 10-14 μm with Fines.

Nominal distance apart, μm	**Actual distance apart, μm**	**Particle 1 size, μm**	**Particle 2 size, μm**	**Powder layer resistance, Ω**
0	0	22.4		1.98
20	35.7	20.2	18.7	1.54
40	40.1	18.9	23.4	1.50
60	76.2	14.9	21.9	1.50
80	96.8	16.4	19.4	1.43
100	115	11.5	24.3	1.68
120	135	27.6	15.7	1.78
140	151	27.3	16.9	1.58

7.4 Temperature Results

7.4.1 Particle Temperature

Figures 7.21 and 7.22 show temperatures of particles intersecting the x-z planes for the average energy levels for Al 10-14 μm and Al 3-4.5 μm powders, respectively. Particles that are white are boiling or have boiled off. Particles located in immediate vicinity of the initial streamer have reached the boiling point for both powders. For Al 10-14 μm powder, the coarse particles in middle of the sample are not significantly heated. Smaller particles can be very hot everywhere, as seen by white speckles spread throughout the sample. Finally, particles at the bottom of the sample appear to be heated more than in its interior. For Al 3-4.5 μm, there are many more particles that are heated to the boiling point. Interestingly, most boiled particles are found at the bottom of the sample.

Figures 7.23-7.25 show particle temperatures vs. their diameters for the energy levels listed in Table 7.4. The points are color-coded based on the vertical coordinate of the particles in the sample; specific ranges of particle heights used to color-code the points are shown in legend. Particles that have fully boiled off are shown to be at 0 K. As Joule energy increases, the sizes of particles that can reach higher temperatures also increase, especially for Al 10-14 μm at 5 kV. For Al 10-14 μm at 5 kV, the majority of particles heated above melting are from the fine fraction. In addition, substantial heating is observed for some coarse particles in the top or bottom-most layers. For Al 10-14 μm at 8 kV, the coarse particles that reach elevated temperatures can only be found in the top layer. This is likely due to combined effects of two discharge streamers and a wider spot diameter used in simulations to match the experimental resistance, resulting in the reduced energy density in the discharge channel. For Al 3-4.5 μm, the particle

temperatures do not appear to be strongly dependent on their size. Significant variation in the observed particle temperatures is likely responsible for the observed experimental spread in the number of ignited particles and their burn times from experiment [53].

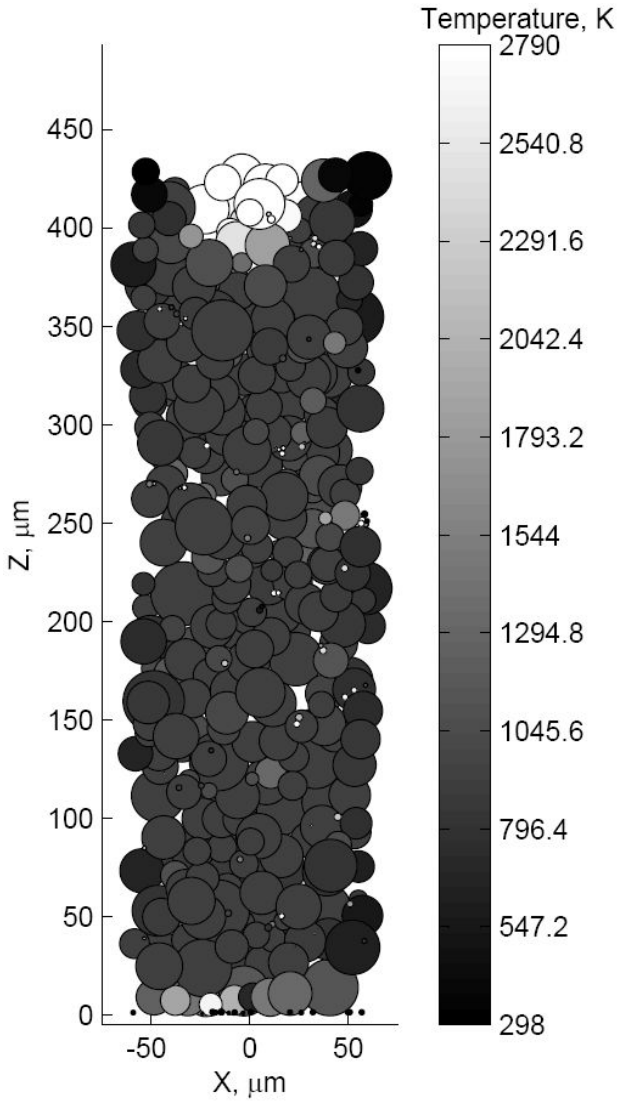

Figure 7.21 Particle temperatures in the X-Z cross-section plane for Al 10-14 μm at the avg energy level (See Table 7.5).

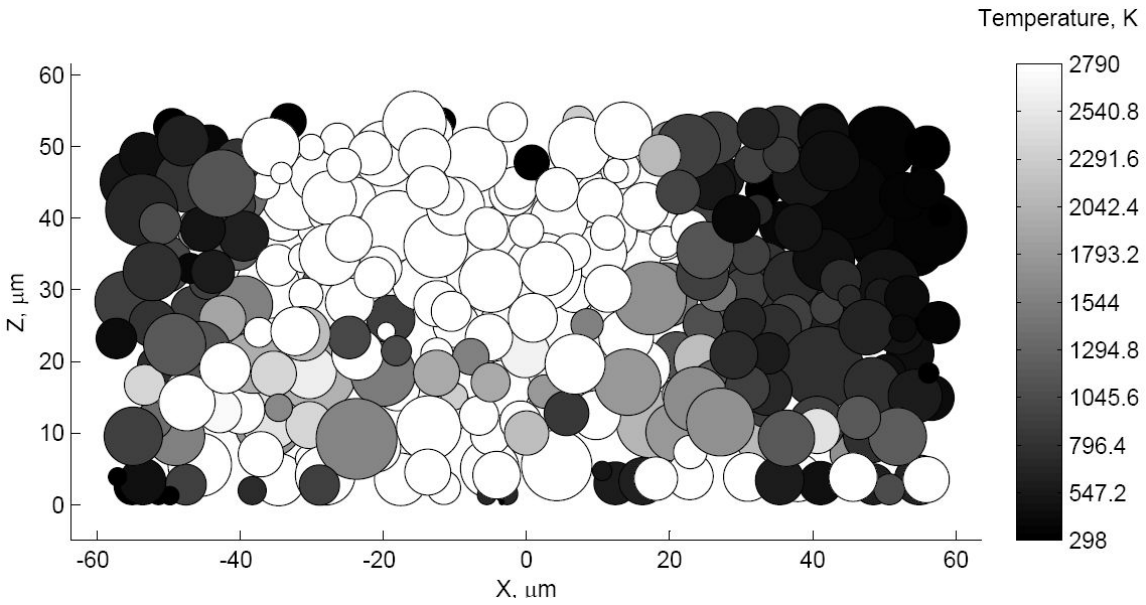

Figure 7.22 Particle temperatures in the X-Z cross-section plane for Al 3-4.5 μm at the avg energy level (see Table 7.5).

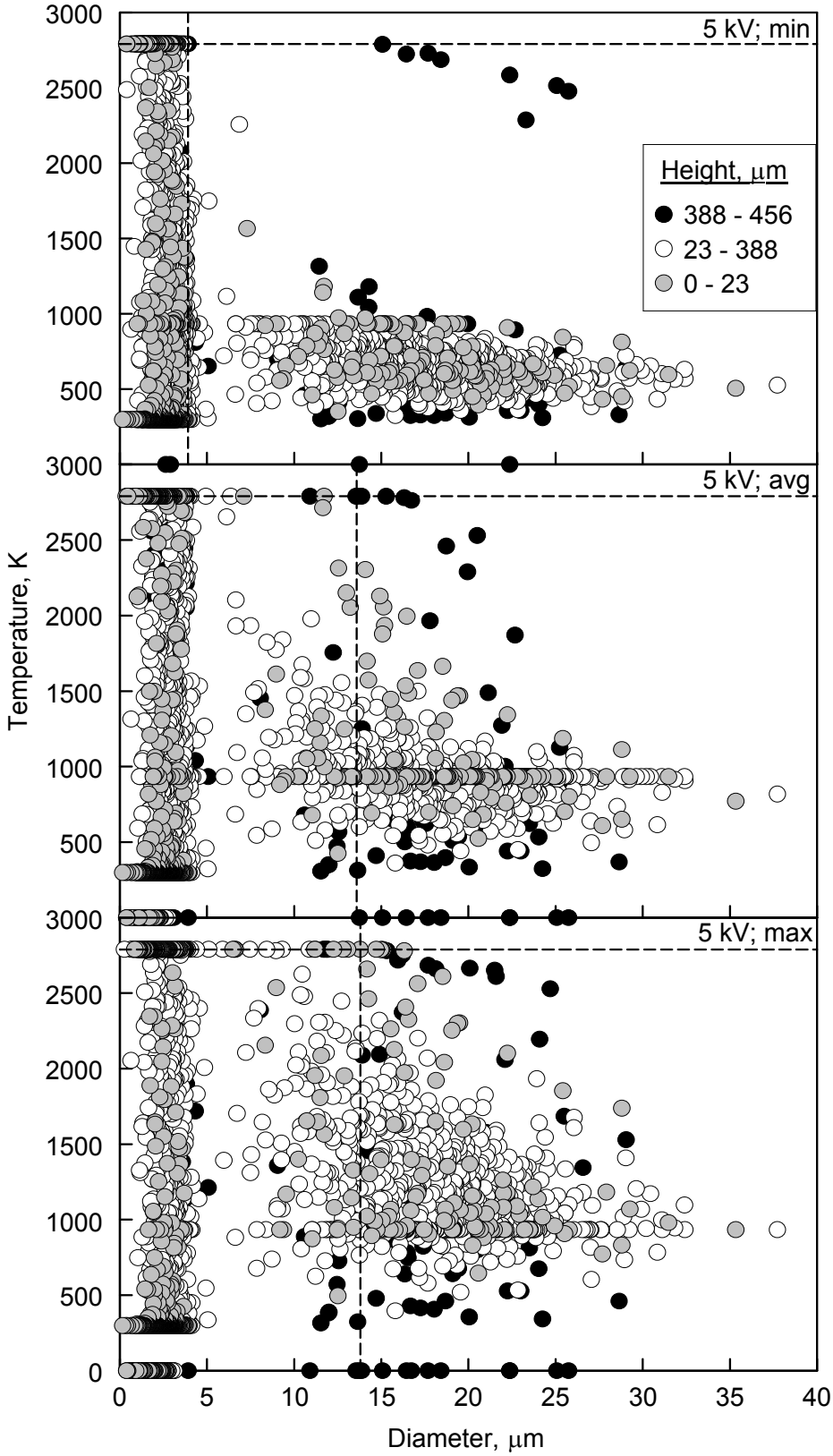

Figure 7.23 Particle temperature vs. diameter for Al 10-14 μm at 5 kV.

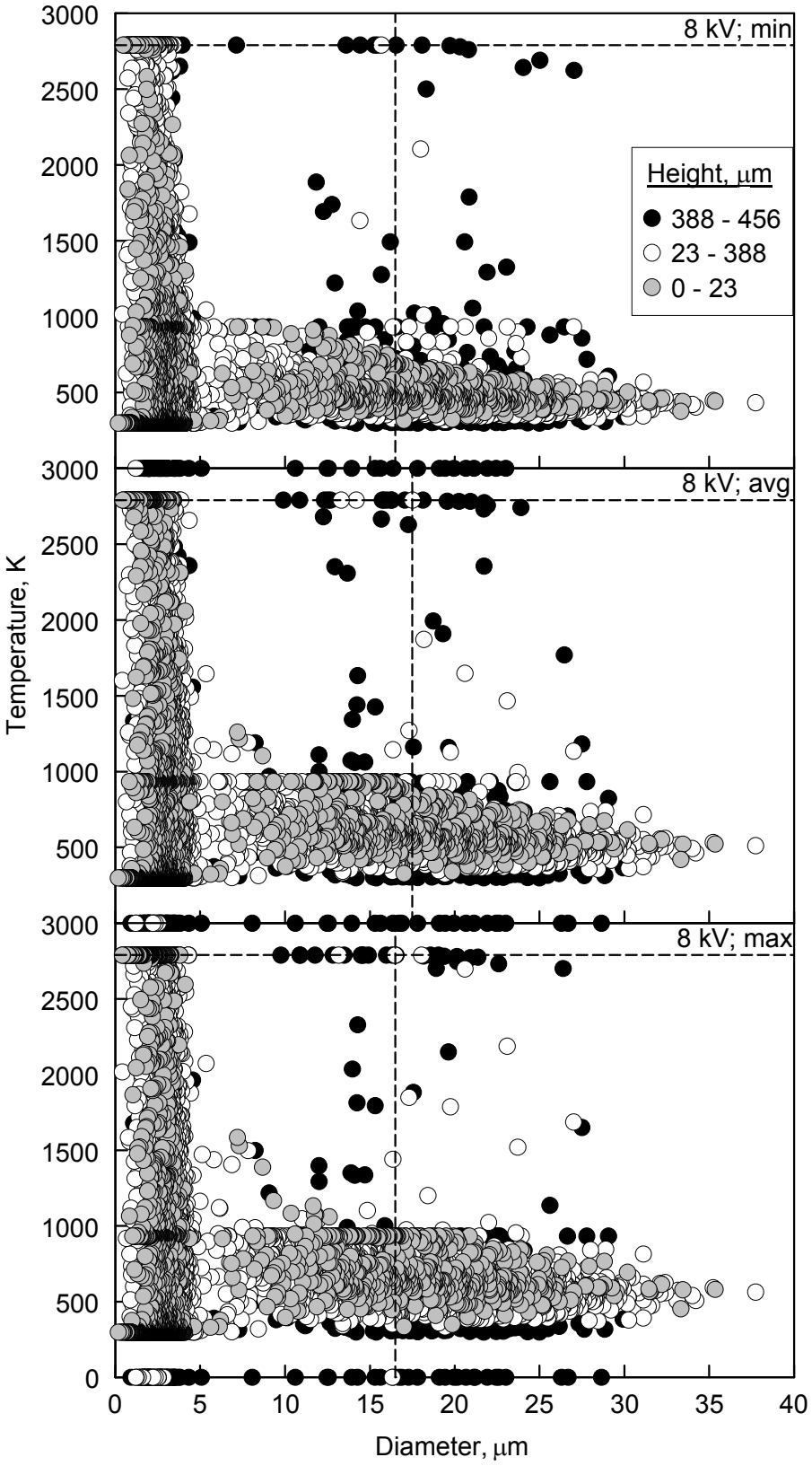

Figure 7.24 Particle temperature vs. diameter for Al 10-14 μm at 8 kV.

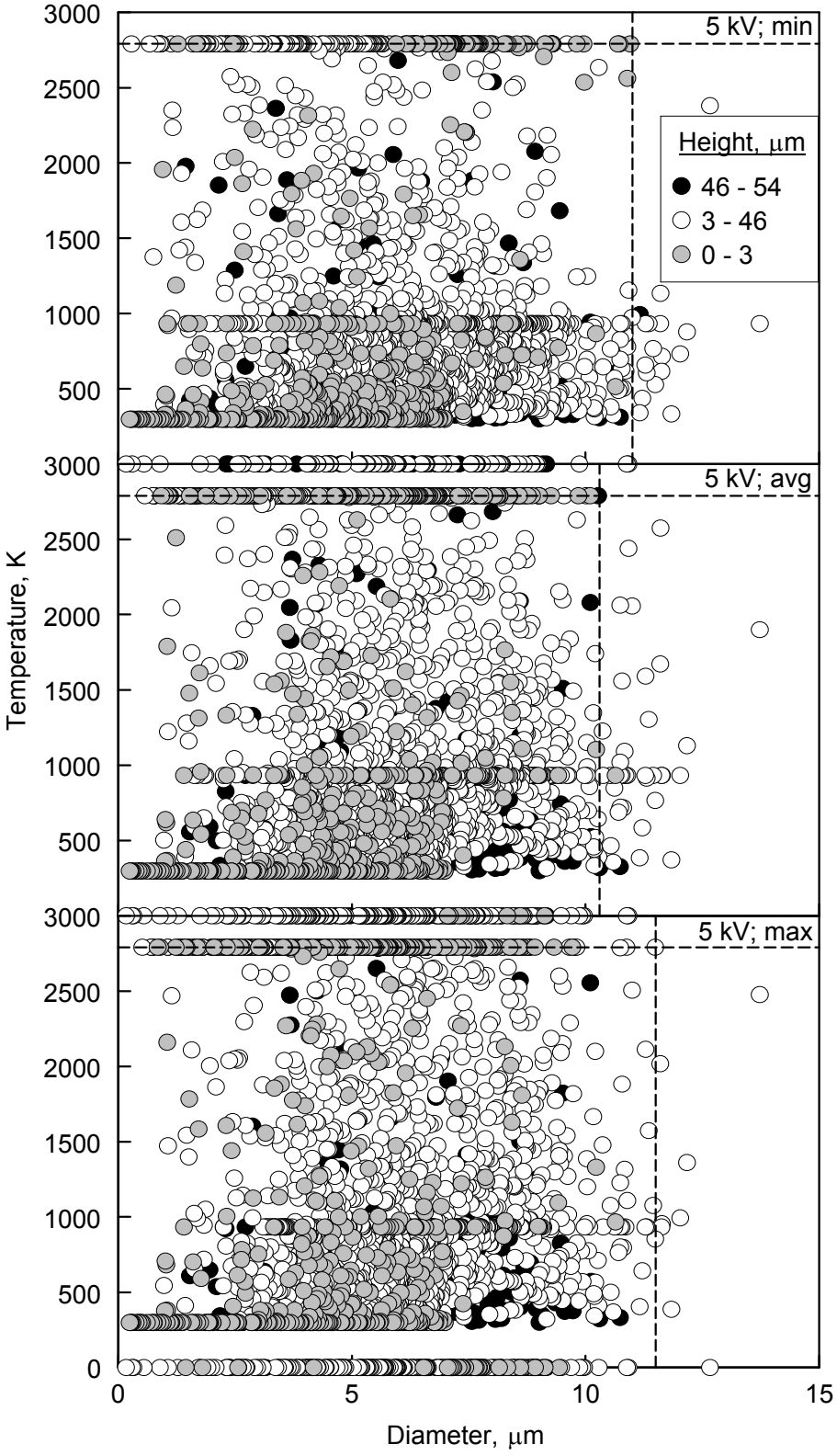

Figure 7.25 Particle temperature vs. diameter for Al 3-4.5 μm at 5 kV.

7.4.2 Ignition of Al Particles

In the literature, Al particle ignition temperature has been shown to vary widely. In the earlier ESD ignition work for Al, ignition taken at the alumina melting point was shown to agree with the experimental result. In these calculations, heat losses were neglected, so that the predicted particle temperatures are likely somewhat higher than in reality. Therefore several predicted temperature levels were considered as leading to ignition: the alumina melting point (2320 K), aluminum boiling point (2790 K), and a temperature taken in between of these two values (2555 K). The largest particles predicted to reach these temperatures are shown in Table 7.7. Table 7.7 also shows the number of particles that reach or exceed the respective temperature level.

For Al 10-14 μm, the bulk of the ignited particles come from the fine fraction of the powder. Interestingly, the number of particles to reach the ignition is comparable for both particle size distributions (with and without fines). At the alumina melting point the largest particle to ignite is between 20-27 μm for Al 10-14 μm and 11-14 μm for Al 3-4.5 μm, respectively. Clearly, the sizes of heated particles are not directly determined by the Joule energy. The most pronounced correlation between the temperature level and Joule energy is observed for Al 10-14 μm particles heated up to their boiling point with the ESD voltage set up at 5 kV. Particle sizes predicted to be heated to the Al boiling, shaded in Table 7.7, correlate best with the experimental data from [53] as shown in Figure 7.26. Note the largest particle diameters predicted to be heated to the boiling point of Al are shown by vertical dashed lines in Figures 7.23-7.25.

Table 7.7 Largest Size and Overall Number of Particles Predicted to be Heated to Different Temperature Levels

Powder	ESD voltage, kV	Energy level	Temp. level, K	Largest particle heated, μm	Number of fine particles heated	Number of coarse particles heated	Total number of particles heated
Al 10-14 μm	5	Min	2790	3.92	227	0	227
			2555	22.4	256	5	261
			2320	25.8	294	7	301
		Avg	2790	13.6	493	7	500
			2555	16.7	524	12	536
			2320	20.5	556	14	570
		Max	2790	13.8	531	19	550
			2555	21.6	548	37	585
			2320	24.7	580	50	630
	8	Min	2790	16.5	181	7	188
			2555	27.0	221	14	235
			2320	27.0	269	15	284
		Avg	2790	17.5	458	14	472
			2555	23.9	558	25	583
			2320	23.9	674	27	701
		Max	2790	16.5	723	15	738
			2555	26.4	831	28	859
			2320	26.4	942	28	970
Al 3-4.5 μm	5	Min	2790	11.0	-	-	181
			2555	11.0	-	-	199
			2320	12.7	-	-	225
		Avg	2790	10.3	-	-	338
			2555	11.6	-	-	364
			2320	11.6	-	-	398
		Max	2790	11.5	-	-	368
			2555	11.5	-	-	404
			2320	13.7	-	-	447

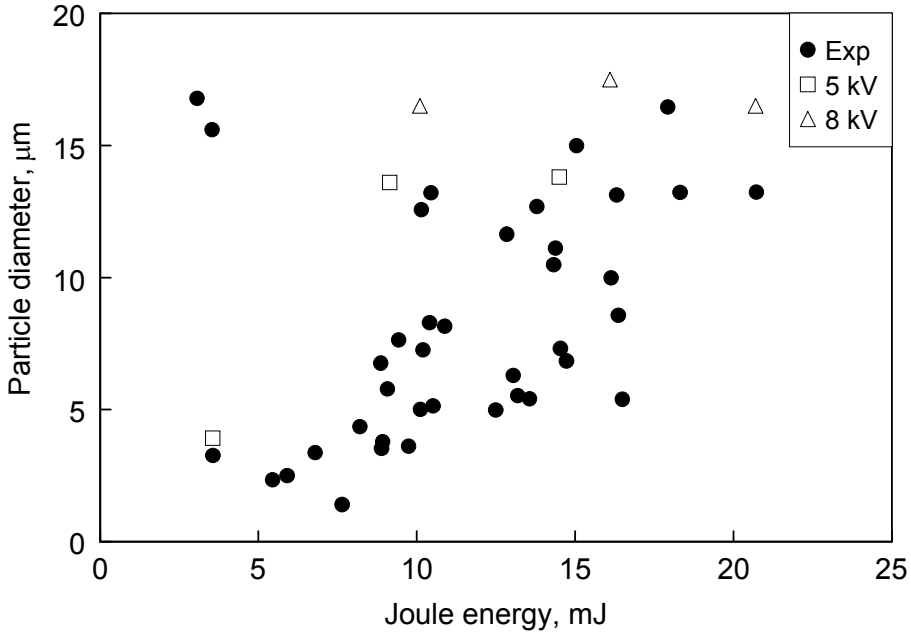

Figure 7.26 Particle diameter estimated to ignite as a function of Joule energy. The filled symbols correspond to particle diameters estimated from the measured burn times. The open symbols correspond to the largest particle size predicted to reach the Al boiling point.

7.4.3 Number of Ignited Particles

Figure 7.27 shows the number of individual burning particle streaks observed in experiments as a function of Joule energy. The number of particles burning is a weak function of Joule energy and varies between 10-30 particles. Based on the streak dimensions, they were produced by relatively large particles burning for several ms or longer. To compare these experimental data to the present calculations, the open symbols in Figure 7.27 show number of particles greater than 5 μm that were heated up to the boiling point of Al. Results are for Al 10-14 μm (cf. Table 7.7) for all energy levels at 5 kV and 8 kV. There is a good correlation between the numbers of particles observed to ignite and burn in experiments, and the number of particles predicted to be heated to the boiling point of Al.

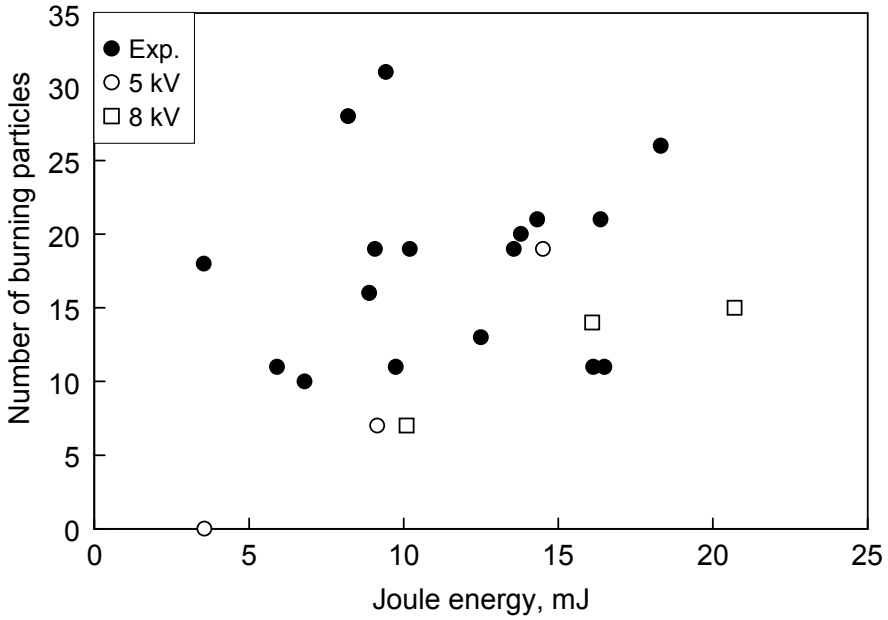

Figure 7.27 Number of ignited particles vs. Joule energy. The filled symbols show the number of burning particle streaks observed in experiments and the open symbols show the number of particles greater than 5 μm heated to the boiling point of Al.

7.4.4 Discussion of Ignition Results

The ignition estimates for Al 10-14 μm as given in Chapter 4, Figure 4.12 do not directly correlate with the results in Figure 7.26. This difference is mainly due to how energy was distributed throughout the powder. In the heat transfer model given in Chapter 4, it was assumed that the energy was distributed uniformly to particles of the same size. In reality, as reflected in DEM, particles are heated according to how particles make contact and how the voltage drops through the powder. Lastly, DEM can both predict the number of particles and sizes of particles that can ignite at a given ignition energy, making it a better and a more comprehensive model for Al heating and ignition.

It should be noted that the PSD used in simulation, does not match the experimental size distribution well. A broader size distribution could alter how the

current passes through the powder and affect the heating and ignition of the powder. The effect of size distribution should be further investigated.

CHAPTER 8

CONCLUSIONS

Ignition of metal powders by ESD was investigated. It was found that for the characteristic ESD ignition testing configurations, the spark duration is of the order of a few μs. The current in the discharge has substantial AC component so that the polarity of the electrodes was observed to be insignificant for the spark energy transfer to the powder. It was also found that only about one-third of the energy stored in the capacitor is supplied to the igniting powder as a result of its Joule heating.

For Mg powder used in the experiments, the powder ignition was observed to be delayed by 0.5–3.5 ms after the spark discharge is over. Shorter ignition delays were observed for greater spark energies. In addition shorter ignition delays were observed for experiments conducted with binder or with smaller sample holder, for which a greater portion of energy was transferred to the powder as a result of direct Joule heating. A portion of the powder was observed to be ejected by the spark independently whether ignition was or was not observed. It was hypothesized that the ejection is due to a shock wave produced by the spark and reflected from the bottom of the sample holder. Limiting the powder ejection by adding a small amount of binder to the powder affects the dependency of the ignition delay on the spark energy. For the powder with the binder, the decrease in the ignition delays is almost linear as a function of the spark energy. With no binder, the ignition delays level out for the spark energy of about 60 mJ and do not decrease at greater spark energies. A simplified estimate shows that the ignition can be described considering that the spark current first adiabatically heats a powder cylinder

located directly under the spark plasma channel. Considering the experimentally determined minimum ignition energy for magnesium powder, the radius of this cylinder directly heated by the Joule heat generated by the spark current is estimated to be between 42 and 46 μm. Individual particles ejected from this initially heated cylinder enter the oxidizing gas environment at a temperature exceeding that required for the self-sustaining particle combustion. Thus, visible streaks are produced by these individual burning particles. When the majority of powder is not ejected by the spark, the powder cylinder directly heated by the spark current starts oxidizing and the released enthalpy of oxidation heats the rest of the powder causing its subsequent ignition.

For Al powders, it was shown that visible particle streaks are not adequate indicators of the powder ignition. It was also observed that spark ignition can result in the formation of individual burning aluminum particles as well as of an aerosol flame. In case of ignition of individual ejected particles, many more particles are ejected from the powder surface than are ignited. Therefore, the mechanisms of particle ejection and ignition by ESD are not directly related to each other. The dimensions and number of streaks produced by igniting particles are decreased with the decrease in the spark energy. However, the MIE defined as the minimum energy stored in the capacitor and required to achieve a detectable ignition is not a useful powder characteristic because it is strongly affected by the sensitivity of the used optical diagnostics. Duration of the emission signal produced by igniting particles was measured and correlated with the applied spark energy and Joule heating energy. A clear correlation was observed for a coarser, unagglomerated powder with nominal diameters in the range of 10–14 μm. However, the trend was barely distinguished for a finer powder, for which the particles were heavily agglomerated. For

the un-agglomerated powder, it is observed that ignition can be reasonably described theoretically assuming that the particles are heated by the spark's current proportionally to their surface area. For practical purposes, it is proposed that the durations of the measured photodiode pulses determine the time the exothermic reactions induced by the spark continue and can serve as useful indicators of the powder ignition sensitivity. Such durations can be measured for a specific spark energy or energy range. Shorter reaction times correspond to the powders that are less sensitive and thus safer to handle. Similarly, the lengths of the particle streaks, preferably measured with a pre-determined camera sensitivity, can be used to assess the distance to which the ignited particles can travel. The maximum streak length can also be considered as a quantitative indicator of the powder ignition sensitivity to the ESD stimulation, with shorter distances corresponding to powders that are less sensitive and safer to handle.

For Ti powders, several ignition modes were observed and were strongly affected by both powder morphology and layer thickness. For both spherical and sponge Ti powders prepared as monolayers, ESD initiation results in fragmentation of the initial particles. Produced particle fragments are ejected from the sample holder and burn as fine individual particles. The burn times for such particles are substantially shorter than expected for the particles present in the starting Ti powder. Sponge powder placed in thicker layers also ignited generating individual burning particles with combustion times close to those expected based on the particle size distribution. Spherical Ti powder placed in thicker layers was difficult to ignite and only a few short individual particle streaks were observed, which could be attributed to the finest particles present in the sample. When a titanium powder (either spherical and sponge) was placed in a layer with

thickness greater than 0.1 mm, significant fusing of the particles was observed which reduced the electrical resistance of the powder layer and minimized its heating by the discharge's Joule energy. Although the energy needed for ignition of monolayer is less than thick layers, a greater amount of material is observed burning. Therefore, powders prepared as a monolayer are potentially a greater fire hazard than that of powder prepared as a thick layer.

The ignition mode and characteristics affecting the powder ignition by ESD are significantly influenced by the thickness of the powder layer tested. For all three metals, Mg, Al, and Ti, the ESD resulted in fragmentation of the particles prepared as a monolayer. Such fragmented particles typically produced a dust cloud flame. Dust cloud flame was also observed for all Mg powder samples. Either a dust cloud flame or individual particle combustion was observed for thicker layers of Al powders. Only single particle combustion mode was detected for thicker Ti powder layers. The powder layer thickness significantly affected initial velocities of the particles ejected by the spark as well as the flame shape, when the dust cloud flames were formed. These effects are important for assessing the fire hazard in practical situations. Both the powder layer thickness and applied ESD voltage affected the electrical resistance of the powder layers. It is possible to roughly estimate the temperatures of the ignited metal particles adiabatically heated by the ESD Joule energy for Al and Mg assuming that the entire powder layer thickness is heated. However, a similar estimate for Ti yields an unreasonably low temperature, suggesting that only a fraction of the Ti powder layer thickness is effectively heated by the ESD current.

DEM simulations were used to describe the powder packing in polydisperse powder layers subjected to ESD initiation. The equivalent layer resistance is described by analyzing electrical resistance network produced by individual particle contacts. Each contact was assumed to be broken through by a micro-discharge in which the minimum voltage drop was restricted to the electrode fall potential. The model was calibrated by matching the experimental and predicted powder layer resistances and Joule energies for Al powders with different powder layer thicknesses and particle size distributions. The volume heated by the spark directly was predicted by analyzing current distribution in the sample. The diameter of the zone predicted to be directly heated by the spark agrees with earlier measurements of the spark imprint diameters. The model predicts temperatures of all particles in the affected zone, assuming their adiabatic heating by the ESD current. Particles are observed to be heated most readily if they are located in the top and bottom-most layers in the powder. It was shown that the dimension of the largest Al particles predicted to be heated up to the boiling point matched the dimensions of the largest particle observed to ignite in respective experiments. The number of particles of predicted to be heated to the boiling point compare well with the number of individual particle streaks detected in the respective experiments.

APPENDIX A

DERIVATION

From Figure 7.4, the following geometric relations can be made in order to determine the micro-discharge radius, a.

$$r_i + r_j + l_g = r_i^* + r_j^* + l_b \tag{A.1}$$

$$\left(r_i^*\right)^2 + a^2 = \left(r_i\right)^2 \tag{A.2}$$

$$\left(r_j^*\right)^2 + a^2 = \left(r_j\right)^2 \tag{A.3}$$

Solving for r_i^* in Equation (A.1) yields:

$$r_i^* = r_i + r_j + l_g - r_j^* - l_b \tag{A.4}$$

In Equation (A.4), the several lengths are known and for a contact are constant:

$$C = r_i + r_j + l_g - l_b \tag{A.5}$$

Solving for r_j^* in Equation (A.3) yields:

$$r_j^* = \left(\left(r_j\right)^2 - a^2\right)^{0.5} \tag{A.6}$$

Combining Equations (A.2), (A.5), and (A.6) yields:

$$C^2 - 2Cr_j^* + \left(r_j^*\right)^2 = r_i^2 - a^2 \tag{A.7}$$

Substituting Equation (A.6) into Equation (A.7), yields:

$$C^2 - 2C\left(r_j^2 - a^2\right)^{0.5} + r_j^2 - a^2 = r_i^2 - a^2 \tag{A.8}$$

Solving for a, in terms of the known radii, gap, and minimum breakdown distance yields Equation (A.9) which is Equation (7.5).

$$a = \left(r_j^2 - \left(\frac{C^2 + r_j^2 - r_i^2}{2C} \right)^2 \right)^{0.5} \qquad \text{(A.9)}$$

$$C = r_i + r_j + l_g - l_b$$

APPENDIX B

IGNITION OF NANOCOMPOSITE THERMITE POWDERS

B.1 Motivation

ESD sensitive nanocomposite thermites are often stored in an inert environment in order to reduce the effects of powder aging and reduce fire hazards. However, this effect is unclear as typical ESD sensitivity testing of powder is carried out in an air environment. Therefore, ESD ignition sensitivity tests are carried out in an inert gas environment to assess if there is any impact on the ignition of nanocomposite powders

B.2 Experiment

Figure B.1 below shows the modified ESD ignition apparatus described in Chapter 2. The discharge electrodes are placed in a sealable stainless steel chamber. The electrical diagnostics are the same as described in Chapter 2. Polycarbonate windows which are bolted on the chamber to seal it are see through which allow for optical measurements of the burning powder. The chamber can be evacuated and a desired gas environment can be filled in to a desired pressure.

In these experiments, Ar was used as the inert gas environment and the pressure in experiment was at 1 atm. To minimize the presence of O_2, the chamber was evacuated three times and filled with Ar after each evacuation. The percentage of O_2 by pressure left in the chamber was estimated to be 0.006 %. In addition to experiments in Ar, experiments were conducted in vacuum. To reduce the amount of O_2 in the chamber the

same evacuation and Ar filling was done as described above. Then a 4th evacuation was carried out reducing the absolute pressure in the chamber to 0.067 atm.

Two nanocomposite thermites were used in these experiments: $4Al + MoO_3$ and $4Al + Fe_2O_3$. The stoichiometries were chosen as these powders are fuel rich which can react with ambient air. Therefore these powders are likely affected by gas environment in which the powder burns. Powders were prepared as a 500 μm layer thickness.

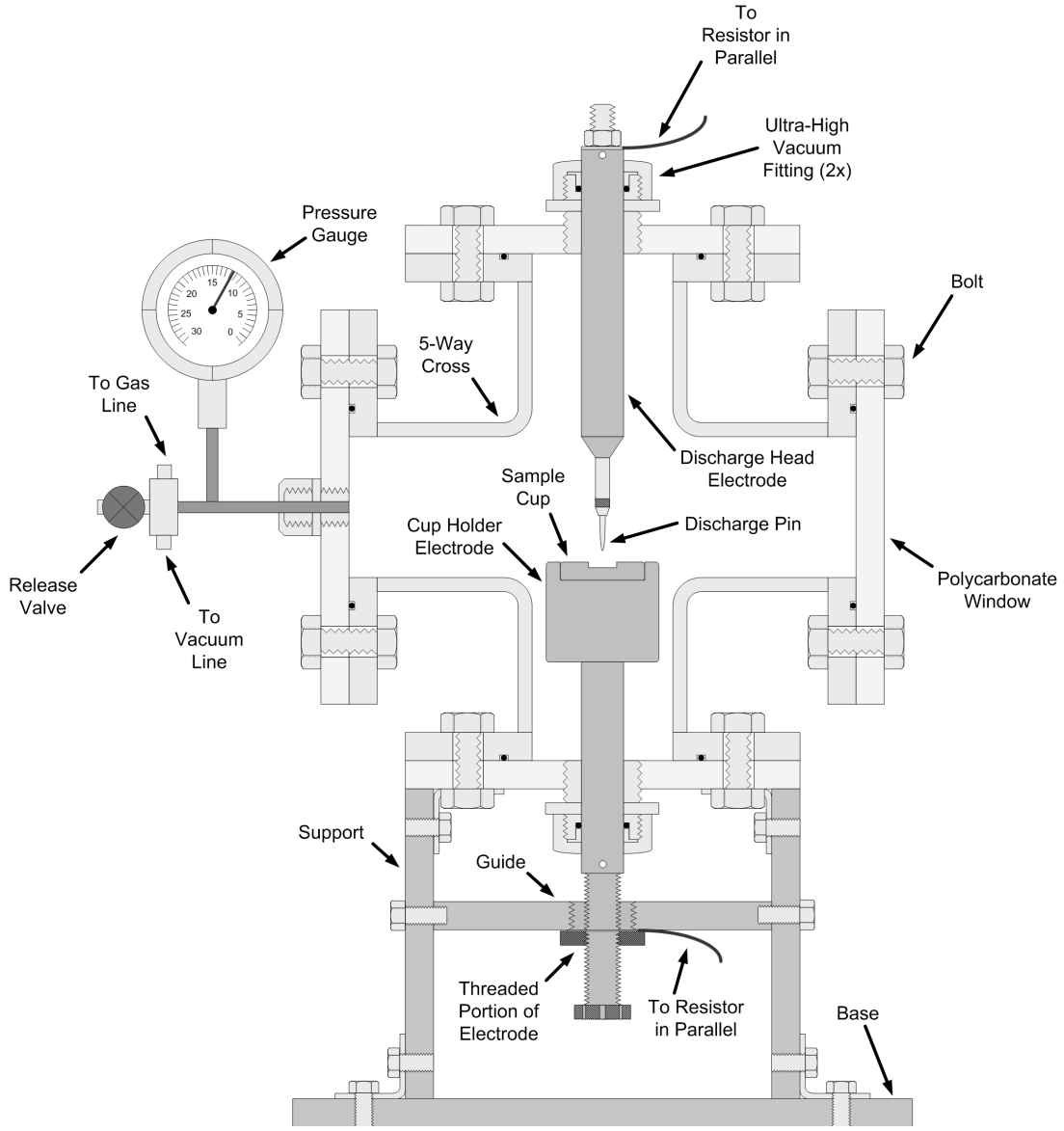

Figure B.1 Modified experimental apparatus used in ESD ignition experiments of nanocomposite thermite powder in a controlled gas environment.

B.3 Ignition of $4Al + MoO_3$

$4Al + MoO_3$ ignited by ESD in an Ar environment produces an brilliant dust cloud flame. In addition powder not directly heated by the spark was ignited leaving little to no un-reacted powder left in the sample cup. This burn behavior is very similar to $4Al + MoO_3$ burning in an air environment. In a few ignition experiments, individual streaks were observed burning as shown in Figure B.2. In addition several micro-explosions can be observed. During these ignition experiments the acquired images were processed to determine the pixel intensity a summary of which is shown by the filled symbols in Figure B.3. The pixel intensity correlates with the amount and sizes of particles that burn. The dashed line corresponds to the maximum pixel intensity. With the exception of low Joule energies, a dust cloud flame was observed.

Under a vacuum environment the burn behavior is drastically different, and example of which is shown in Figure B.4. Many faint streaks are observed burning with several micro-explosions observed. In addition the individual burning particles appear to burn for a longer time, as many particles are seen bouncing off the chamber walls. Particles are observed to fan out in greater angles when burned under vacuum as compared to under Ar. Interestingly, the powder not directly heated by the spark is remains un-reacted. The open symbols in Figure B.3 show the pixel intensity vs. Joule energy of ignition experiments in vacuum. The pixel intensities are below the Ar ignition experiments, indicating that fewer particles ignited. This difference in burn behavior is likely due to a reduction of heat transfer that occurs in a gas environment at reduced pressure.

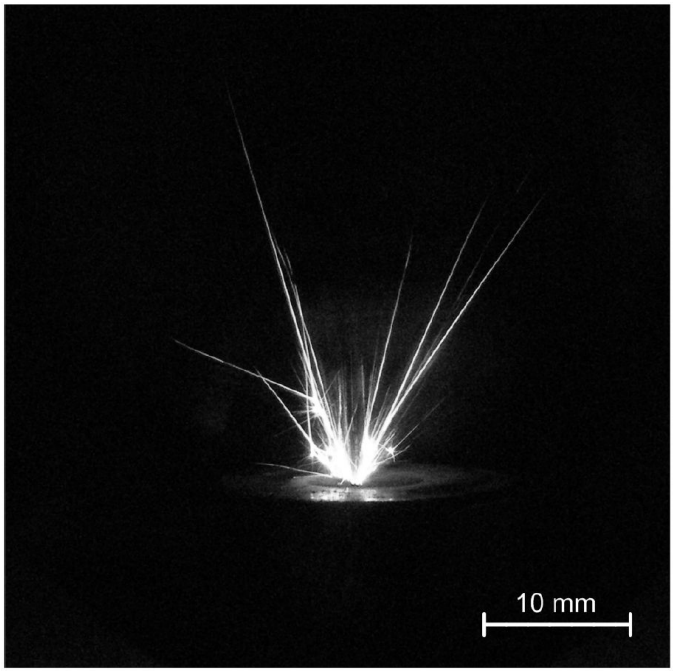

Figure B.2 Still image of $4Al + MoO_3$ ignited in Ar, at low Joule energies.

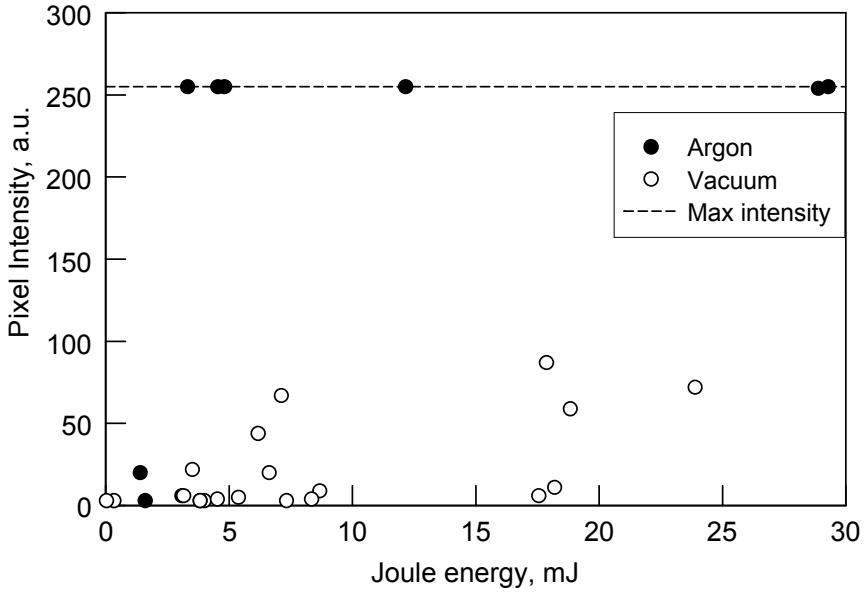

Figure B.3 Pixel intensity vs. Joule energy of $4Al + MoO_3$ ignited in Ar and vacuum.

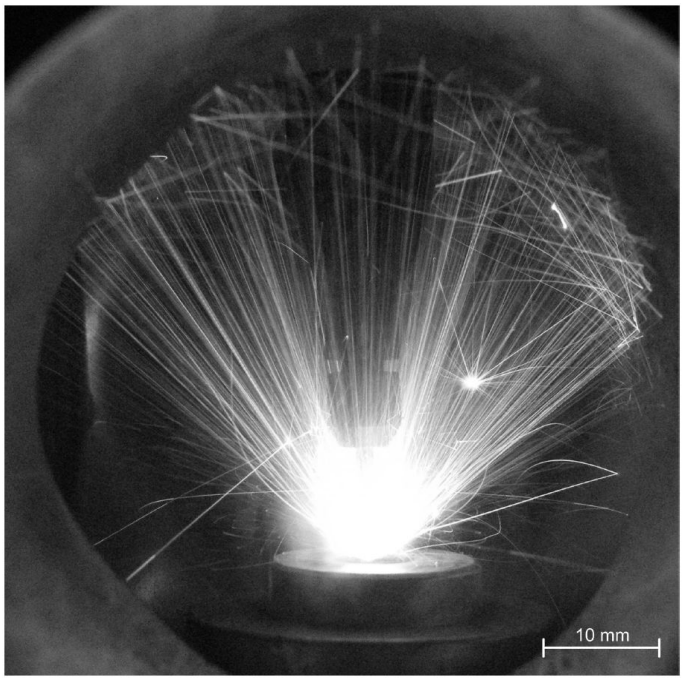

Figure B.4 Still image of 4Al + MoO_3 ignited in vacuum.

B.4 Ignition of 4Al + Fe_2O_3

4Al + Fe_2O_3 ignited in vacuum burns similarly as 4Al + MoO_3 ignited in vacuum, an example of which is shown in Figure B.5. The streaks are thicker than the streaks of burning 4Al + MoO_3. In addition there does not appear to be any micro-explosions. Figure B.6 shows pixel intensity vs. Joule energy of 4Al + Fe_2O_3. 4Al + Fe_2O_3 was observed to be fairly agglomerated, and two sets of ignition experiments were carried out, with and without agglomerated powder. The un-agglomerated and agglomerated powder are represented by filled and open symbols, respectively. Pixel intensity increases with increasing Joule energy for un-agglomerated powder but no trend is observed for the agglomerated powder. In either case the pixel intensity is comparable to that of 4Al + MoO_3 ignited in vacuum. Lastly, the burn duration was measured for the agglomerated

4Al + Fe_2O_3, but no clear trend was observed as shown in Figure B.7. Agglomerated powder likely unpredictably than un-agglomerated powder, due to the sizes and contacts involved in the contact made.

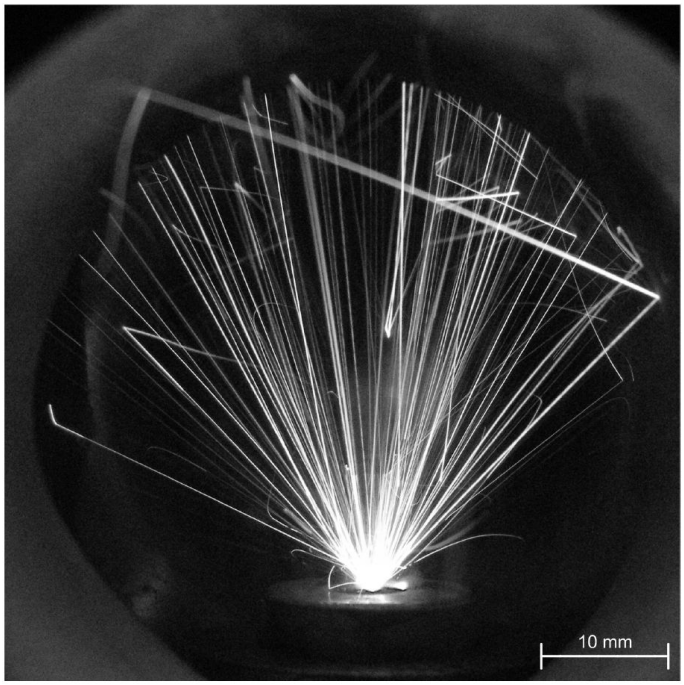

Figure B.5 Still image of 4Al + Fe_2O_3 ignited in vacuum.

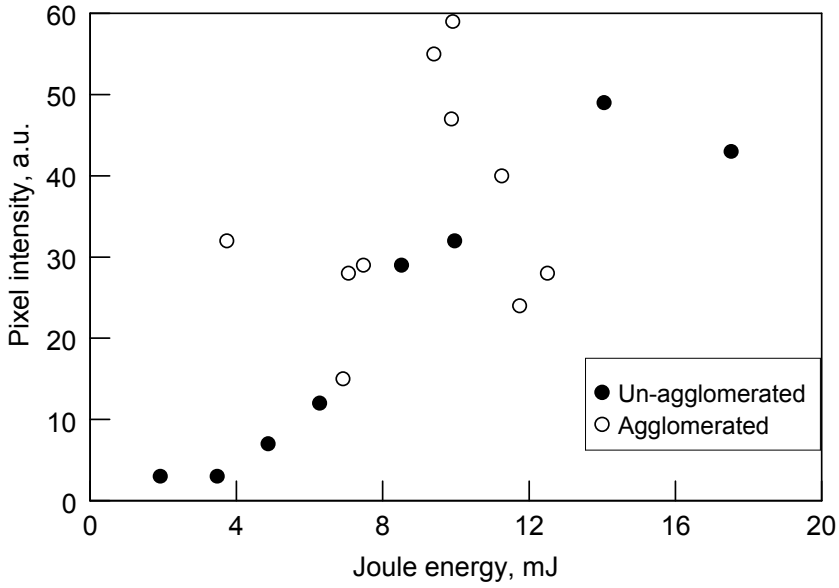

Figure B.6 Pixel intensity vs. Joule energy of agglomerated and un-agglomerated 4Al + Fe_2O_3 ignited in vacuum.

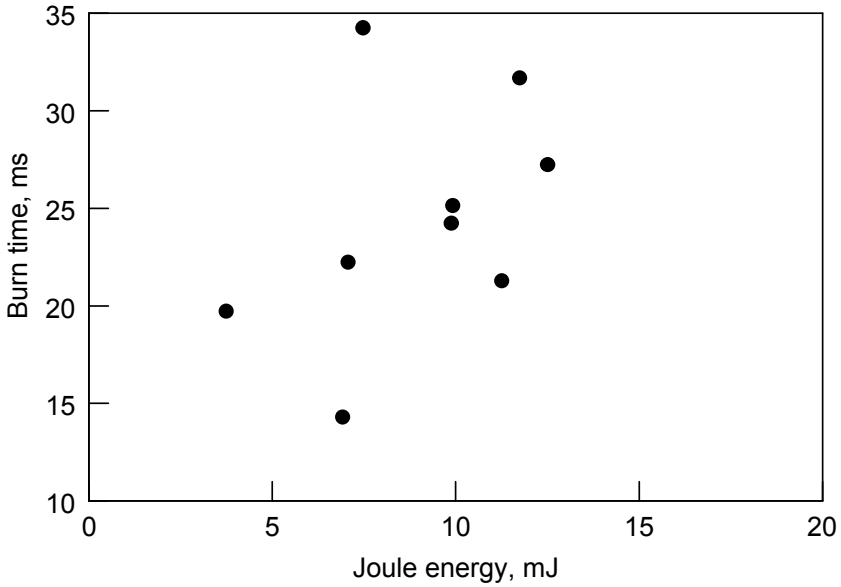

Figure B.7 Burn time vs. Joule energy of agglomerated 4Al + Fe_2O_3 ignited in vacuum.

REFERENCES

1. Glor, M. Hazards due to electrostatic charging of powders, Journal of Electrostatics 16 (2–3), (1985) 175-191.

2. Glor, M. Ignition hazard due to static electricity in particulate processes, Powder Technology 135-136, (2003) 223-233.

3. Glor, M. Electrostatic ignition hazards in the process industry, Journal of Electrostatics 63 (6-10), (2005) 447-453.

4. Walther, C.D., Schacke, H. Danger of electrostatic ignition in the handling of solvent containing bulk materials +IBM- Explosion in a facility that manufactures coating materials, VDI Berichte 2024, (2008) 79-96.

5. Smallwood, J. Standardisation of electrostatic test methods and electrostatic discharge prevention measures for the world market, Journal of Electrostatics 63 (6-10), (2005) 501-508.

6. von Pidoll, U. An overview of standards concerning unwanted electrostatic discharges, Journal of Electrostatics 67 (2–3), (2009) 445-452.

7. Dahn, C.J., Dastidar, A.G. Requirements for a minimum ignition energy standard, Process Safety Progress 22 (1), (2003) 43-47.

8. Perrin, L., Laurent, A., Falk, V., Dufaud, O., Traore, M. Dust and electrostatic hazards, could we improve the current standards?, Journal of Loss Prevention in the Process Industries 20 (3), (2007) 207-217.

9. Mellor, A.M., Stoops, D.R., Rudy, T.O., Hermsen, R.W. Optimization of spark and ESD propellant sensitivity tests, Propellants, Explosives, and Pyrotechnics 15, (1990) 1-7.

10. Mellor, A.M., Baker, P.J. Propellant properties conducive to electrostatics discharge ignition, Journal of Energetic Materials 12, (1994) 1-62.

11. Ryzhik, A.B. Critical conditions of the spark ignition of metal powder suspensions in gas, Fizika Goreniya i Vzryva (in Russian) 14, (1978) 53-57.

12. Ryzhik, A.B., Makhin, V.S., Kititsa, V.N. Detonation of aerosols of disperse magnesium, Fizika Goreniya i Vzryva (in Russian) 16 (2), (1980) 78-84.

13. Kim, S.W., Colver, G.M. Spark ignition of aluminum powder in mixtures of oxygen, nitrogen, and carbon dioxide. A new testing method, American Society of Mechanical Engineers, Heat Transfer Division 148, (1990) 97-104.

14. Kao, C.S., Duh, Y.S. Accident investigation of an ABS plant, Journal of Loss Prevention in the Process Industries 15 (3), (2002) 223-232.

15. Wu, A., Chen, Y., Hu, X., Liu, S. Research on ESD ignition hazards of textiles, Journal Electrostatics 57 (3-4), (2003) 203-207.

16. Tunnicliffe, G., Thomson, M. Explosion Protection, Cleanroom Technology 9 (9), (2003) 29-32.

17. Marmo, L., Cavallero, D. Minimum ignition energy of nylon fibres, Journal of Loss Prevention in the Process Industries 21 (5), (2008) 512-517.

18. Gao, L., Zhou, H., Zhou, B.M. Investigation of hazard classification and protection measures for ESD ignition in powder handling processes, Donbei Daxue Zuebao/Journal of Northeastern University 27 (Suppl.), (2006) 125-128.

19. Senecal, J.A. Manganese mill dust explosion, Journal of Loss Prevention in the Process Industries 4, (1991) 332.

20. Matsuda, T., Yamaguma, M. Tantalum dust deflagration in a bad filter dust-collecting device, Journal of Hazardous Materials 77 (1-3), (2000) 33-42.

21. Ebadat, V., Pilkington, G. Assessing dust explosion hazards in powder handling operations, Chemical Processing 58 (9), (1995) 5.

22. Zeman, S., Koci, J. Electric spark sensitivity of polynitro compounds: Part IV. A relation to thermal decomposition parameters, Energetic Materials 8 (1), (2000) 23-26.

23. Skinnner, D., Olson, D., Block-Bolton, A. Electrostatic discharge ignition of energetic materials, Propellants, Explosives, and Pyrotechnics 23, (1998) 34-42.

24. Matsugi, K., Hatayama, T., Yanagisawa, O. Effect of direct current pulse discharge on specific resistivity of copper and iron powder compacts, Journal of the Japan Institute of Metals 59 (7), (1995) 740-745.

25. Belyaev, A.A., Gutso, D.E., Kiseev, V.M. Formation of inter-particle contact resistance in powder materials, Poroshkovaya Metallurgiya (in Russian) 10, (1992) 83-86.

26. Allied Ordnance Publications, Manual of Data Requirements and Tests for the Qualification of Explosive Materials for Military Use, AOP-7 ED.2, US Department of Defense, Washington, DC, (2003).

27. International Electrotechnical Commission, Commission Publication, Electromagnetic compatibility (EMC) – Part 4-2: Testing and measurement techniques – Electrostatic discharge immunity tests IEC 61000-4-2 Edition Geneva: 1.2, (2001).

28. Roberts, T.A., Burton, R.L., Krier, H., Ignition and combustion of aluminum/magnesium alloy particles in O_2 at high pressures, Combustion and Flame 92 (1-2), (1993) 125-143.

29. Ward, T.S., Trunov, M.A., Schoenitz, M., Dreizin, E.L. Experimental methodology and heat transfer model for identification of ignition kinetics of powered fuels, International Journal of Heat and Mass Transfer 49 (25-26), (2006) 4943–4954.

30. Mohan, S. Experiment and Modeling: Ignition of Al particles with a CO_2 laser, New Jersey Institute of Technology, PhD dissertation, (2008) 77-79.

31. Star Brite, Star Brite liquid electrical tape MSDS. http://www.starbrite.com/, accessed June 2008.

32. Pearse, R.W.B., Gaydon, A.G. The Identification of Molecular Spectra, 4th ed., Chapman and Hall, Chapman and Hall, London, UK, (1976).

33. Herzberg, G. Molecular Spectra and Molecular Structure: Spectra of Diatomic Molecules, 2nd ed., D. van Nostrand, New York, USA, (1950).

34. Borghese, A., D'Alessio, A., Diana, M., Veintozzi, C. Development of hot nitrogen kernel, produced by a very fast spark discharge, Proceedings of the Combustion Institute 22, (1988) 1651-1659.

35. Kerchner, R.M., Corcoran, G.F., eds. Alternating Current Circuits, 4th ed., John Wiley & Sons, New York, USA, (1960).

36. Sher, E., Ben-Yalish, J., Kravichik, T. On the birth of spark channels, Combustion and Flame 89, (1992) 186-194.

37. Howatson, A.M. An introduction to gas discharges, Pergamon Press, Oxford, UK, (1965).

38. McCahill, M.J., Lee, R.J., Remmers, D.L., Electrostatic Discharge Sensitivity, Revisited JANNAF PSHS, (2002).

39. Ono, R., Nifuku, M., Fujiwara, S., Horiguchi, S., Oda, T. Gas temperature of the capacitance spark discharge in air, Journal of Applied Physics 97 (12), (2005) 1-7.

40. Incropera, F.P., Dewitt, D.P., Bergman, T.L., Lavine, A.S., eds. Introduction of Heat Transfer, 5th ed., John Wiley & Sons, New York, USA, (2007).

41. UTHSCSA Image Tool v 3.0, University of Texas Health Science Center at San Antonio, (2002).

42. Dreizin, E.L. Experimental study of stages in aluminum particle combustion in air, Combustion and Flame 105 (4), (1996) 541-556.

43. Ebadat, V., Prugh, R.W. Case study: aluminum-dust explosion, Process Safety Progress 26 (4), (2007) 324-329.

44. Colver, G.M., Kim, S.W., Yu, T.U. An electrostatic suspension method for testing spark breakdown, ignition, and quenching of powders, Journal of Electrostatics 37 (3), (1996) 151-172.

45. Myers, T.J. Reducing aluminum dust explosion hazards: case study of dust inerting in an aluminum buffing operation, Journal of Hazardous Materials 159 (1), (2008) 72-80.

46. Mel'nikov, M.A., Nikitin, V.V. Effect of aluminum on the sensitivity and electric-spark ignition of explosives, Fizika Goreniya i Vzryva (in Russian) 8 (4), (1974) 396-400.

47. Wu, H.C., Ou, H.J., Hsiao, H.C., Shih, T.S. Explosion characteristics of aluminum nanopowders, Aerosol and Air Quality Research 10 (1), (2010) 38-42.

48. Stamatis, D., Jiang, X., Beloni, E., Dreizin, E.L. Aluminum burn rate modifiers based on reactive nanocomposite powders, Propellants, Explosives, and Pyrotechnics 35 (3), (2010) 260-267.

49. Shoshin, Y.L., Dreizin, E.L. Particle combustion rates for mechanically alloyed Al-Ti and aluminum powders burning in air, Combustion and Flame 145 (4), (2006) 714-722.

50. Lynch, P., Krier, H., Glumac, N. A correlation for burn time of aluminum particles in the transition regime, Proceedings of the Combustion Institute 32, (2009) 1887-1893.

51. Beloni, E., Dreizin, E.L. Experimental study of ignition of magnesium powder by electrostatic discharge, Combustion and Flame 156, (2009) 1386-1395.

52. Mohan, S., Furet, L., Dreizin, E.L. Aluminum particle ignition in different oxidizing environments, Combustion and Flame 157 (7), (2010) 1356-1363.

53. Beloni, E., Dreizin E.L. Ignition of aluminum powder by electro-static discharge, Combustion and Flame 157 (7), (2010) 1346-1355.

54. Collins, E.W. Materials properties handbook: titanium alloys, ASM International, Materials Park, USA, (1994).

55. Dolganov, A.P., Kovalev, V.N. High-temperature interaction between titanium foil and oxygen, Latvijas PSR Zinatnu Akademijas Vestis, Fizikas un Technisko Zinatnu Serija (in Russian) 4, (1988) 82-88.

56. Andrzejak, T.A., Shafirovich, E., Varma, A. On the mechanisms of Ti particle reaction in O_2/N_2 and O_2/Ar atmospheres, Propellants, Explosives, Pyrotechnics 34, (2009) 35-58.

57. Derevyaga, M.E., Stesik, L.N., Fedorin, E.A. Ignition in titanium in oxygen, Combustion, Explosives, Shock Waves 12 (4), 493-496.

58. Chernenko, E.V. Griva, V.A., Rozenband, V.I. Investigation of the laws of ignition of titanium powders, Combustion, Explosives, Shock Waves 18 (5), (1982) 513-518.

59. Song, X., Liu, X., Zhang, J. Neck formation and self-adjusting mechanism of neck growth of conducting powders in spark plasma sintering, Journal of American Ceramic Society 89 (2), (2006) 494-500.

60. Shafirovich, E., Teoh, S.K., Varma, A. Combustion of levitated titanium particles in air, Combustion and Flame 152 (1-2), (2008) 262-271.

61. Beloni, E., Dreizin, E.L. Ignition of titanium powder by electro-static discharge, Combustion, Science, and Technology, (2011) accepted for publication.

62. Ravi Kumar, N.V. Effect of alloying elements on the ignition resistance of magnesium alloys, Scripta Materialia 49, (2003) 225-230.

63. Boiko, V.M., Poplavski, S.V. Self-ignition and ignition of aluminum powders in shock waves, Shock Waves 11, (2001) 289-295.

64. Williams, R.A., Beloni, E., Dreizin, E.L. Ignition of metal powder samples with different thicknesses by electrostatic discharge, Journal of Propulsion and Power, (2011) submitted for publication.

65. Bala, K., Pradhan, P.R., Saxena, N.S., Saksena, M.P. Effective thermal conductivity of copper powders, Journal of Physics D: Applied Physics 22, (1989) 1068-1072.

66. Gusarov, A.V., Kovalev, E.P. Model of thermal conductivity in powder beds, Physical Review B 80, (2009) 1-15.

67. Kirkpatrick, S. Percolation and conduction, Reviews of Modern Physics 45 (4), (1973), 574-588.

68. Zekri, L., Kaiss, A., Clerc, J.P., Porterie, B., Zekri, N. 2D-to-3D percolation crossover of metal insulator composites, Physical Letters Section A: General, Atomic, and Solid State Physics 375 (3), (2011) 346-351.

69. Bhattacharya, S., Tandon, R.P., and Sachdev, V.K. Electrical conduction of graphite Filled high density polyethylene composites; experiment and theory, Journal of Material Science 44, (2009) 2430-2433.

70. Montes, J.M., Cuevas, F.G., Cintas, J. Porosity effects on the electrical conductivity of sintered powder compacts, Applied Physics A 92, (2008) 375-380.

71. Patel, K.K., Paulsen, J.M., Desilvestro, J. Numerical simulation of porous materials in relation to battery electrodes and separators, Journal of Power Sources 122, (2003) 144-152.

72. Mari, C.M., Dotelli, G. A random resistor model to forecast the electrical properties of crystalline ionic conductor composites, Solid States Ionics 136-137, (2000) 1315-1319.

73. Argento, C., Bouvard, D. Modeling the effective thermal conductivity of random sphere packing of spheres through densification, International Journal of Heat and Mass Transfer 29 (7), (1996) 1343-1350.

74. Bahrami, M., Yovanovich, M.M., Culham, J.R. Effective thermal conductivity of rough spherical packed beds, International Journal of Heat and Mass Transfer 49, (2006) 3691-3701.

75. Slavin, A.J., Arcas, V., Greenhalgh, C.A., Irvine, E.R., Marshall, D.B. Theoretical model for the thermal conductivity of a packed bed of solid spheroids in the presence of static gas, with no adjustable parameters except at low pressure and temperature, International Journal of Heat and Mass Transfer 45, (2002) 4151-4161.

76. Bakker, K. Using the finite element method to compute the influence of complex Porosity and inclusion structures on the thermal and

77. EDEM software, DEM Solutions Ltd., http://www.dem-solutions.com/, accessed November 2010.

78. Schramm, J., Witter, K. Gas discharges in very small gaps in relation to electrography, Applied Physics 1, (1973) 331-337.

79. Shi, J.J., Kong, M.G., Cathode fall characteristics in a dc atmosphere pressure glow discharge, Journal of Applied Physics 94 (9), (3003) 5504-5513.

80. Hemmi, R., Yokomizu, Y., Matsumura, T. Anode-fall and cathode-fall voltages of air arc in atmosphere between silver electrodes, Journal of Physics D: Applied Physics 36, (2003) 1097-1106.

81. Pursch, H., Schoepp, H., Kettlitz, M., Hess, H. Arc attachment and fall voltage on the cathode of an ac high-pressure mercury discharge, Journal of Physics D: Applied Physics 35, (2002) 1757-1760.

82. Hajossy, R., Morva, I. Cathode and anode falls of arcs with fusible electrodes, Journal of Physics D: Applied Physics 27, (1994) 2095-2101.

83. Harris, W.J., O'Hair, E.A., Hatfield, L.L., Kristiansen, M. Cathode erosion research on medium to high power arcjet thrusters, IEEE Transactions on Electron Devices 28, (1993) 280-292.

84. Spears, J.W., Krompholz, H., Hatfield, L.L. Sub-nanosecond point-plane gas breakdown in conical-shaped spark gap, Digest of Technical Papers-IEEE International Pulsed Powder Conference, (2003) 1347-1350.

85. Yamashita, H., Yamazawa, K., Wang, Y.S. The effect of tip curvature on the prebreakdown streamer structure in cyclohexane, IEEE Transactions on Dielectrics and Electrical Insulation 5(3), (1998) 396-401.

86. Finkelnburg, W., Segal, S.M. High temperature plasma properties from high current arc stream measurements, Physical Review 80 (2), (1950) 258-260.

87. Simmons, R.O., Balluffi, R.W. Measurements of the high-temperature electrical resistance of aluminum: resistivity of lattice vacancies, Physical Review 117 (1), (1960) 62-68.

88. Bazelyan, E.M., Raizer, Y.P. Spark discharge. CRC Press, New York, (1998).